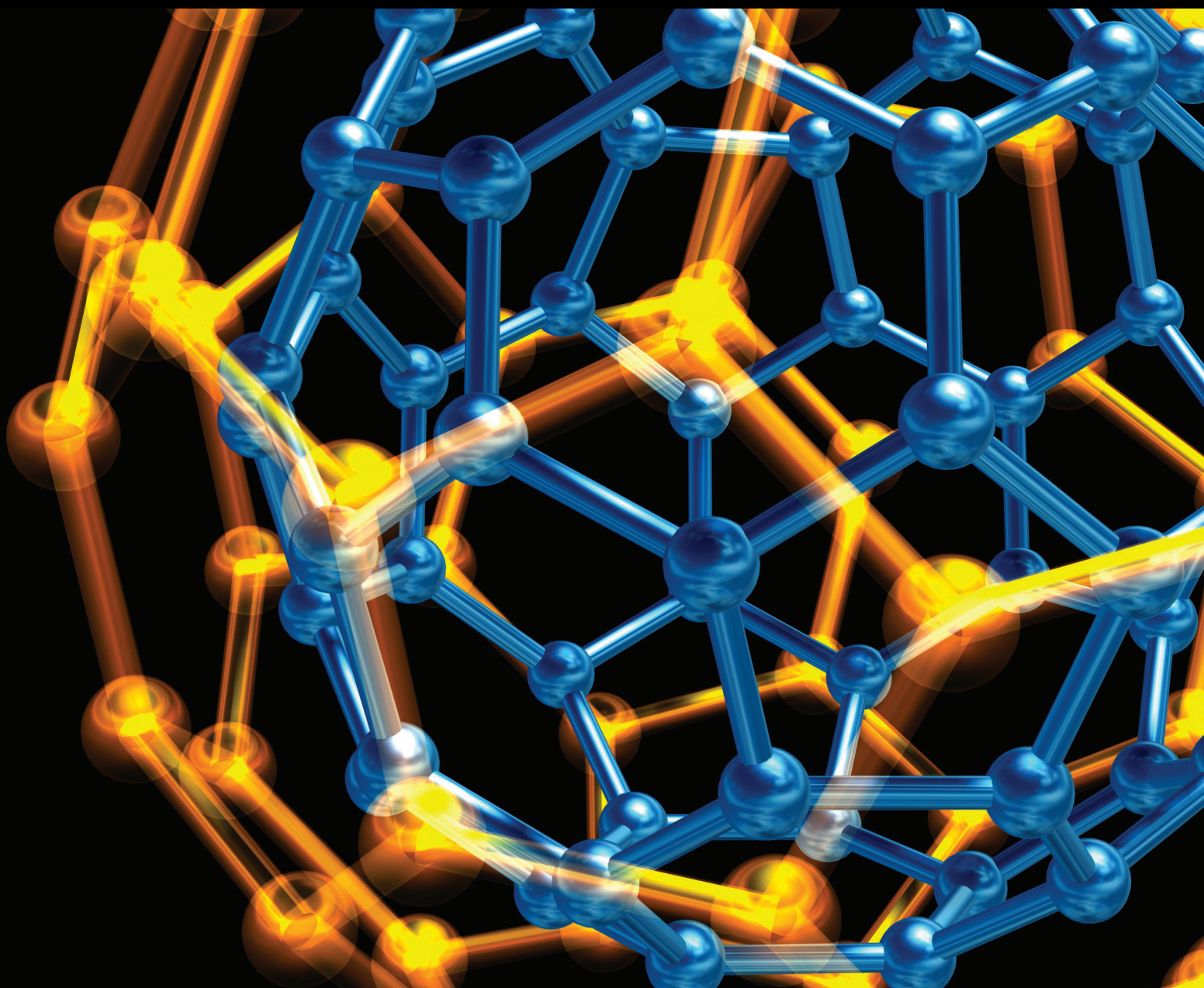


# Metal Oxide Nanostructures: Synthesis, Properties, and Applications

Guest Editors: Lin-Hua Xu, Dnyaneshwar S. Patil, Jiazhi Yang,  
and Jingzhong Xiao





---

# **Metal Oxide Nanostructures: Synthesis, Properties, and Applications**

## **Metal Oxide Nanostructures: Synthesis, Properties, and Applications**

Guest Editors: Lin-Hua Xu, Dnyaneshwar S. Patil, Jiazhi Yang,  
and Jingzhong Xiao



---

Copyright © 2015 Hindawi Publishing Corporation. All rights reserved.

This is a special issue published in “Journal of Nanotechnology.” All articles are open access articles distributed under the Creative Commons Attribution License, which permits unrestricted use, distribution, and reproduction in any medium, provided the original work is properly cited.



## Editorial Board

Simon Joseph Antony, UK  
Felix A. Buot, USA  
Carlos R. Cabrera, Puerto Rico  
Franco Cerrina, USA  
Gan Moog Chow, Singapore  
Jeffery L. Coffey, USA  
Enkeleida Dervishi, USA  
Dmitriy A. Dikin, USA  
Dimitris Drikakis, UK  
John S. Foord, UK  
Joseph Irudayaraj, USA  
Niraj K. Jha, USA

Miguel Jose-Yacamán, USA  
Valery Khabashesku, USA  
Sakhrat Khizroev, USA  
Abdel Salam H. Makhlouf, Germany  
Constantinos Mavroidis, USA  
Paolo Milani, Italy  
Oded Millo, Israel  
Oussama Moutanabbir, Canada  
M. Grant Norton, USA  
Paresh Chandra Ray, USA  
Benjaram M. Reddy, India  
Mehmet Sarikaya, USA

Jorge M. Seminario, USA  
V. Shalaev, USA  
Mahi R. Singh, Canada  
Xiaowei Sun, Singapore  
O. K. Tan, Singapore  
Thomas Thundat, USA  
Boris I. Yakobson, USA  
Nan Yao, USA  
Yoke K. Yap, USA  
Chuan Jian Zhong, USA

## Contents

**Metal Oxide Nanostructures: Synthesis, Properties, and Applications**, Lin-Hua Xu,  
Dnyaneshwar S. Patil, Jiazhi Yang, and Jingzhong Xiao  
Volume 2015, Article ID 135715, 2 pages

**Growth Mechanisms of Nanostructured Titania in Turbulent Reacting Flows**, Sean C. Garrick  
Volume 2015, Article ID 642014, 10 pages

**Preparation of ZnO/CdS/BC Photocatalyst Hybrid Fiber and Research of Its Photocatalytic Properties**,  
Beibei Dai, Cheng Chao, Xiaoyu Lu, Qingcheng Xia, Jing Han, Fei Mao, Jiazhi Yang, and Dongping Sun  
Volume 2015, Article ID 614170, 8 pages

**Comparing and Optimizing Nitrate Adsorption from Aqueous Solution Using Fe/Pt Bimetallic Nanoparticles and Anion Exchange Resins**, Muhammad Daud, Zahiruddin Khan, Aisha Ashgar, M. Ihsan Danish, and Ishtiaq A. Qazi  
Volume 2015, Article ID 985984, 7 pages

**Silica Sol-Gel Entrapment of the Enzyme Chloroperoxidase**, Tuan Le, Selina Chan, Bassem Ebaid, and Monika Sommerhalter  
Volume 2015, Article ID 632076, 10 pages

**Synthesis and Application of Magnetic Photocatalyst of Ni-Zn Ferrite/TiO<sub>2</sub> from IC Lead Frame Scraps**, Robert Liu and H. T. Ou  
Volume 2015, Article ID 727210, 7 pages

**TiO<sub>2</sub> Nanocatalysts Supported on a Hybrid Carbon-Covered Alumina Support: Comparison between Visible Light and UV Light Degradation of Rhodamine B**, Mphilisi M. Mahlambi, Ajay K. Mishra, Shivani B. Mishra, Rui W. Krause, Bhekie B. Mamba, and Ashok M. Raichur  
Volume 2015, Article ID 198723, 8 pages

## Editorial

# Metal Oxide Nanostructures: Synthesis, Properties, and Applications

**Lin-Hua Xu,<sup>1</sup> Dnyaneshwar S. Patil,<sup>2</sup> Jiazhi Yang,<sup>3</sup> and Jingzhong Xiao<sup>4</sup>**

<sup>1</sup>*School of Physics and Optoelectronic Engineering, Nanjing University of Information Science & Technology, Nanjing 210044, China*

<sup>2</sup>*Department of Electronics, North Maharashtra University, Jalgaon, Maharashtra 425001, India*

<sup>3</sup>*School of Chemistry and Chemical Engineering, Nanjing University of Science and Technology, Nanjing 210094, China*

<sup>4</sup>*Department of Physics, Faculty of Science and Technology (FCT), University of Coimbra (UC), Rua Larga, 3004-516 Coimbra, Portugal*

Correspondence should be addressed to Lin-Hua Xu; 474860864@qq.com

Received 7 September 2015; Accepted 7 September 2015

Copyright © 2015 Lin-Hua Xu et al. This is an open access article distributed under the Creative Commons Attribution License, which permits unrestricted use, distribution, and reproduction in any medium, provided the original work is properly cited.

In recent years, nanostructured materials have attracted wide attention due to their fascinating optical and electrical properties, which make these materials potentially suitable for applications in electronics, optics, photonics, and sensors. Some metal oxides show a wide variety of morphologies such as nanowires, nanorods, nanotubes, nanorings, and nanobelts. Synthesis and investigation of these metal-oxide nanostructures are beneficial not only for understanding the fundamental phenomena in low dimensional systems, but also for developing new-generation nanodevices with high performance.

This special issue is focused on synthesis, properties, characterizations, and numerical modeling of metal-oxide nanomaterials and nanostructures with potential applications in photocatalysts, wastewater purification, chemical sensors, and so on.

B. Dai et al. reported that an environment-friendly biomaterial bacterial cellulose (BC) was introduced to substitute for general organic polymers to assist the preparation of ZnO/CdS/BC photocatalyst hybrid nanofiber through coprecipitation method under the low-temperature condition. The photocatalytic activities of ZnO/CdS/BC were influenced by the added amount of CdS. It is found that ZnO/CdS/BC nanohybrid fibers (CdS: 10%) show the best photocatalytic efficiency among the samples.

R. Liu and H. Tai Ou reported that IC lead frame scraps were used in their research as raw materials to fabricate

magnetic ferrite powders and combined subsequently with titanium sulfate and urea to produce magnetic photocatalysts by coprecipitation for effective waste utilization. They found that wastes can be transformed to valuable magnetic photocatalysts in their research to solve the separation problem of wastewater and TiO<sub>2</sub> photocatalysts by magnetic field.

M. Mahlambe et al. studied the TiO<sub>2</sub> nanocatalysts supported on a hybrid carbon-covered alumina (CCA) support and carried out a comparison between visible light and UV light degradation of Rhodamine B. The CCA/TiO<sub>2</sub> nanocatalysts had a much larger surface area than the unsupported titania and they exhibited overall higher photodegradation efficiency under both UV and visible light than unsupported TiO<sub>2</sub>.

T. Le et al. reported that the enzyme CPO was successfully entrapped inside a silica nanostructure prepared from the precursor TMOS with or without addition of the hydrophobic modifier MTMS. The catalytic performance of optimized CPO sol-gel beads approached 18% relative to free CPO in solution as assessed via the pyrogallol peroxidation assay.

M. Daud et al. carried out a research work for the removal of nitrate from raw water for a drinking water supply using Fe/Pt bimetallic nanoparticles and anion exchange resins. The overall results indicate that Fe/Pt nanoparticles having a large surface area (627 m<sup>2</sup>/g) are potentially more efficient than the commercially used anionic resins for nitrate removal from water.

Growth mechanisms of nanostructured titania in turbulent reacting flows were studied by S. C. Garrick. Direct numerical simulation is utilized in simulating the hydrolysis of titanium tetrachloride to produce titania in a turbulent, planar jet. Results show that, in the proximal region of the jet, nucleation and condensation are the dominant mechanisms. However, once the jet potential core collapses and turbulent mixing begins, coagulation is the dominant mechanism. The data also shows that the coagulation growth rate is as much as twice the condensation growth rate.

## **Acknowledgments**

The guest editorial team would like to thank the authors for their contributions to this special issue and the reviewers for their precious time and dedication.

*Lin-Hua Xu*  
*Dnyaneshwar S. Patil*  
*Jiazhi Yang*  
*Jingzhong Xiao*

## Research Article

# Growth Mechanisms of Nanostructured Titania in Turbulent Reacting Flows

Sean C. Garrick

*Department of Mechanical Engineering, University of Minnesota, 111 Church Street SE, Minneapolis, MN 55455-0111, USA*

Correspondence should be addressed to Sean C. Garrick; [sgarrick@umn.edu](mailto:sgarrick@umn.edu)

Received 5 June 2015; Accepted 22 July 2015

Academic Editor: Lin-Hua Xu

Copyright © 2015 Sean C. Garrick. This is an open access article distributed under the Creative Commons Attribution License, which permits unrestricted use, distribution, and reproduction in any medium, provided the original work is properly cited.

Titanium dioxide (titania) is used in chemical sensors, pigments, and paints and holds promise as an antimicrobial agent. This is due to its photoinduced activity and, in nanostructured form, its high specific surface area. Particle size and surface area result from the interplay of fluid, chemical, and thermal dynamics as well as nucleation, condensation and coagulation. After nucleation, condensation, and coagulation are the dominant phenomena affecting the particle size distribution. Manufacture of nanostructured titania via gas-phase synthesis often occurs under turbulent flow conditions. This study examines the competition between coagulation and condensation in the growth of nanostructured titania. Direct numerical simulation is utilized in simulating the hydrolysis of titanium tetrachloride to produce titania in a turbulent, planar jet. The fluid, chemical, and particle fields are resolved as a function of space and time. As a result, knowledge of titania is available as a function of space, time, and phase (vapor or particle), facilitating the analysis of the particle dynamics by mechanism. Results show that in the proximal region of the jet nucleation and condensation are the dominant mechanisms. However once the jet potential core collapses and turbulent mixing begins, coagulation is the dominant mechanism. The data also shows that the coagulation growth-rate is as much as twice the condensation growth-rate.

## 1. Introduction

High rate synthesis of nanoparticles from vapor requires operation in the turbulent flow regime [1]. The variety of length and time scales present in turbulent multiphase flows makes them not very amenable to physical observation or analysis. This is especially true in the early stages of the nanoparticle formation and growth processes [2]. Computational fluid dynamics (CFD) has been developed for many years and a variety of numerical techniques have been developed and utilized for studying particle dynamics [3–10]. CFD has enabled engineers to achieve their goals more rapidly and cost effectively [11]. It has also become an effective tool for understanding physicochemical dynamics.

Nakaso et al. [12] modeled the titania nanoparticle growth of both agglomerates and primary particles simultaneously by using spatial zero-dimensional fluid dynamics. Johannessen et al. [13] combined CFD with a mathematical model for the particle dynamics to compare with experimental data from the synthesis of titanium dioxide particles in diffusion

flames. Tsantilis et al. [5] used a moving sectional aerosol dynamics model accounting for gas-phase chemical reactions, coagulation, surface growth, and sintering with zero-dimensional fluid dynamics to investigate flame synthesis of titania nanoparticles. Also one study by Moody and Collins [14] considered titania nanoparticle nucleation and growth in a turbulent “box” located near the center of the reactor via three-dimensional DNS coupled with moment method in particle dynamics. Researchers have also considered the effects of turbulence on particle growth. Strakey et al. [15] studied the role of turbulence on the characteristics of  $\text{TiO}_2$  powder made by  $\text{TiCl}_4$  oxidation and they found that the increased turbulence intensity narrowed the size distribution of the product powder indicating that the particle growth may be dominated by reactant mixing rather than by particle-particle collisions. These computations are quite compute intensive as they resolve all of the appropriate length and time scales. Garrick and his group studied the effects of turbulence on particle coagulation intensively and indicated that turbulence has a positive effect on the particle growth

[16, 17]. The effects of turbulence on nucleation have also been elucidated [18–20]. To obtain physically accurate data, simulations must be three-dimensional and must be model-free. That is, the results must be obtained without the use of turbulence or subgrid scale models [21]. A review of the literature reveals a lack of the detailed information, especially via high-resolution direct simulation, on the interplay between the different mechanisms affecting nanoparticle growth.

In this work, the hydrolysis of titanium tetrachloride ( $\text{TiCl}_4$ ) to produce titanium dioxide ( $\text{TiO}_2$ ) is simulated via direct numerical simulation. The turbulent, reacting, multiphase flow is obtained by solving the Navier-Stokes equations in conjunction with transport equations for all of the relevant chemical species and a nodal approach is used to represent the particle field [22, 23]. With the chemical and particle fields available as a function of space, time, and size, particle nucleation, condensation, and coagulation are illustrated individually. Additionally the two growth mechanisms are elucidated.

## 2. Methodology

The mass, momentum, and energy equations are solved to obtain the fluid velocity  $u_i(\bar{x}, t)$ , pressure  $p(\bar{x}, t)$ , density  $\rho(\bar{x}, t)$ , and the enthalpy  $h(\bar{x}, t)$ . These variables are governed by the following conservation equations:

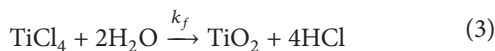
$$\begin{aligned} \frac{\partial \rho}{\partial t} + \frac{\partial \rho u_j}{\partial x_j} &= 0, \\ \frac{\partial \rho u_i}{\partial t} + \frac{\partial \rho u_i u_j}{\partial x_j} &= -\frac{\partial p}{\partial x_i} + \frac{\partial \tau_{ij}}{\partial x_j}, \\ \frac{\partial \rho h}{\partial t} + \frac{\partial \rho u_j h}{\partial x_j} &= \frac{\partial}{\partial x_j} \left( \frac{k}{C_p} \frac{\partial h}{\partial x_j} \right), \end{aligned} \quad (1)$$

where  $\tau_{ij}$  is the viscous stress tensor for a Newtonian fluid,  $k$  is the coefficient of thermal conduction, and  $C_p$  is the specific heat at constant pressure.

**2.1. Chemical Transport.** The fluid contains five chemical species, the transport of which is given by the conservation of species equations:

$$\frac{\partial \rho Y_m}{\partial t} + \frac{\partial \rho u_j Y_m}{\partial x_j} = \frac{\partial}{\partial x_j} \left( \rho \mathcal{D}_m \frac{\partial Y_m}{\partial x_j} \right) + \dot{\omega}_m, \quad (2)$$

where  $Y_m$  is the mass concentration of species  $m$  and  $\mathcal{D}_m$  is the diffusion coefficient of species  $m$ . The reactants,  $\text{TiCl}_4$  and water vapor ( $\text{H}_2\text{O}$ ), undergo an irreversible one-step, isothermal chemical reaction at a temperature of 300 K and atmospheric pressure, which produces titanium dioxide ( $\text{TiO}_2$ ) and hydrochloric acid ( $\text{HCl}$ ):



The source term  $\dot{\omega}_m$  in (2) represents the effects of chemical reaction, the rate of creation or consumption of species  $m$ .

The system is closed with the ideal gas equation of state,  $p = \rho RT$  and  $R = \sum R_m Y_m / MW_m$ , where  $R_m$  and  $MW_m$  are the gas constant and molecular weight of species  $m$ , respectively. The fluid temperature,  $T$ , is obtained using the enthalpy via  $dh = C_p dT$ . The fifth chemical species, nitrogen ( $\text{N}_2$ ), does not participate in any chemical reactions and serves as the carrier gas.

**2.2. Particle Field.** The aerosol general dynamic equation (GDE) describes particle dynamics under the influence of various physicochemical phenomena, convection, diffusion, coagulation, surface growth, nucleation, and other internal/external forces. The GDE is utilized in discrete form as a population balance on each cluster or particle size. The methodology uses the nodal/sectional method of to approximate the GDE [23–26]. This approach effectively divides the aerosol population into three classes, monomers, clusters, and particles [16]. The GDE is therefore solved as a set of  $N_s$  transport equations, one for each bin  $Q_k$ ,  $k = 1, 2, \dots, N_s$  [27]. Monomers of size 0.5 nm in diameter populate bin 1 while bins 2 and 3 are populated by clusters of molecules. Molecular clusters of size 1 nm and larger are considered “particles” [28]. The general transport equation for the concentration of monomers, clusters, and particles in bin  $k$ ,  $Q_k$ , is written as

$$\frac{\partial \rho Q_k}{\partial t} + \frac{\partial \rho u_j Q_k}{\partial x_j} = \frac{\partial}{\partial x_j} \left( \rho D_Q \frac{\partial Q_k}{\partial x_j} \right) + \dot{\omega}_k^Q, \quad (4)$$

where  $D_Q$  is the diffusivity given by

$$D_Q = k_b T \frac{C_c}{3\pi \mu d_p}, \quad (5)$$

where  $k_b$  is the Boltzmann constant,  $C_c$  is the Cunningham correction factor, and  $d_p$  is the mean volume particle diameter [29]. The source term  $\dot{\omega}_k^Q$  represents particle formation and growth processes and is given by

$$\dot{\omega}_k^Q = \begin{cases} J - \rho \sum_{i=1}^{N_s} \beta_{i1} Q_i Q_1, & k = 1, \\ \frac{1}{2} \sum_{i=1}^{N_s} \sum_{j=1}^{N_s} \chi_{ijk} \rho \beta_{ij} Q_i Q_j - \rho \sum_{i=1}^{N_s} \beta_{ik} Q_i Q_k, & k > 1, \end{cases} \quad (6)$$

where  $J$  accounts for the formation of monomers in bin  $k = 1$  via chemical reaction [30–33] and  $\chi_{ijk}$  is given by

$$\chi_{ijk} = \begin{cases} \frac{v_{k+1} - (v_i + v_j)}{v_{k+1} - v_k}, & \text{if } v_k \leq v_i + v_j < v_{k+1}, \\ \frac{(v_i + v_j) - v_{k-1}}{v_k - v_{k-1}}, & \text{if } v_{k-1} \leq v_i + v_j < v_k, \\ 0, & \text{otherwise.} \end{cases} \quad (7)$$

The source term in (6),  $\omega_k^Q$ , represents the effects of nucleation, condensation (via monomer-cluster, monomer-particle and cluster-particle collisions), and Brownian coagulation. In this study, all particle formation and growth processes occur at 300 K. This means that all particles considered

are agglomerates, meaning growth via coagulation results in fractal-like aggregate particles, consisting of primary particles (monomers). The collision frequency function,  $\beta_{ij}$ , is well documented in both the free-molecular and continuum regimes [29, 34–37]. Collisions of all particles (monomers, clusters, etc.) are considered and  $\beta_{ij}$  is given by

$$\beta_{ij} = \begin{cases} a_1 (i^{1/D_f} + j^{1/D_f})^{D_f} \left( \frac{1}{i} + \frac{1}{j} \right)^{1/2}, & D_f < 2 \text{ free-molecular regime,} \\ a \left( i^{1/D_f} + j^{1/D_f} \right)^2 \left( \frac{1}{i} + \frac{1}{j} \right)^{1/2}, & D_f \geq 2 \text{ free-molecular regime,} \\ \frac{2k_b T}{3\mu} \left( \frac{1}{v_i^{1/D_f}} + \frac{1}{v_j^{1/D_f}} \right) (v_i^{1/D_f} + v_j^{1/D_f}), & \text{in continuum regime,} \end{cases} \quad (8)$$

where

$$a = \left( \frac{3v_o}{4\pi} \right)^{1/6} \left( \frac{6k_b T}{\rho_p} \right)^{1/2}, \quad (9)$$

$$a_1 = \frac{2^{D_f} a}{4.89},$$

where  $v_o$  is the primary particle volume,  $v_i$  is the volume of an agglomerate in the  $i$ th section,  $\rho_p$  is the particle density,  $i$  and  $j$  are the primary particle numbers in bins  $i$  and  $j$ , respectively, and  $D_f$  is the fractal dimension. The particles generated by the industrial aerosol processes are usually nonspherical and the products are composed of groups of adhering particles ranging from loosely linked particles, sometimes termed agglomerates, to strongly necked particles, called aggregates or hard agglomerates. The fractal dimension is used to represent the shape of the aggregate or particle structure. A statistical concept, the fractal (or Hausdorff) dimension  $D_f$ , was introduced to describe the shape of the agglomerate, which is obtained after averaging over many agglomerates with the same number of primary particles. The value of the fractal dimension ranges from  $D_f = 1$  to  $D_f = 3$  depending on the details of the agglomerate formation process [29]. The bins are organized in such a manner that the volume of particles in two successive bins is doubled; that is,  $v_k = 2 \times v_{k-1}$  [23, 38].

### 3. Results

**3.1. Flow Configuration.** The flow under consideration is a three-dimensional, isothermal, turbulent reacting jet issuing from an orifice of diameter  $D$  into a coflowing stream. The jet is composed of titanium tetrachloride ( $\text{TiCl}_4$ ) diluted in nitrogen ( $\text{N}_2$ ), while the coflowing stream is composed of water vapor ( $\text{H}_2\text{O}$ ) diluted in  $\text{N}_2$ . The initial velocities are  $U_o = 100$  m/s for the jet and  $U_\infty$  for the coflowing stream. The fluid field is characterized by the velocity ratio  $U_\infty/U_o = 0.2$ . The Reynolds number based on velocity of the high-speed stream and the jet diameter is  $\text{Re} = U_o D/\nu = 3,000$ . The

simulation is performed at 300 K and atmosphere pressure (1 atm). To accelerate the development of large-scale structures, random perturbations with a maximum intensity of 5% are added to the cross-stream  $v$ -velocity. The chemical composition of the jet stream is 0.01%  $\text{TiCl}_4$  and 99.99%  $\text{N}_2$  by mass. The simulation utilizes stoichiometric mixtures and the molar ratio of 1:2 for  $\text{TiCl}_4$  and  $\text{H}_2\text{O}$ .

In this work, several assumptions and approximations are utilized. These are stated below for clarity.

- (1) Ceramic powders such as  $\text{TiO}_2$  have low equilibrium vapor pressures implying that single molecules may be considered particles [31]. As  $\text{TiO}_2$  is formed, it appears as 0.5 nm diameter free spherical  $\text{TiO}_2$  “monomers,” populating bin  $k = 1$ ; hence nucleation is treated as an instantaneous process.
- (2) The nanoparticles are small enough to follow the fluid path lines. Additionally, the particle volume fraction is of order  $10^{-7}$ . As a result the presence of the particles does not affect the fluid field.
- (3) Condensation is dominated by the collision rate of monomers with other monomers, clusters, and particles. This means the condensable species in the simulations is the  $\text{TiO}_2$  “vapor.”
- (4) The clusters and particles are stable because of the high supersaturation of the monomers. As a result, at these temperatures, there is no evaporation or sublimation of particles back to the gas-phase.
- (5) The fractal dimension,  $D_f$ , is based on the collision time,  $\tau_c$ , and sintering time,  $\tau_f$ . In this work, all processes occur at  $T = 300$  K. At this temperature,  $\text{TiO}_2$  particles do not sinter as  $\tau_c \ll \tau_f$  [39].
- (6) A fractal dimension of  $D_f = 3$  is used when collisions occur between monomers while  $D_f = 2$  is used when monomers and dimers collide. For all other particle interactions (collisions between larger particles) a fractal dimension of  $D_f = 1.8$  is used [39, 40].



**3.2. Numerical Specifications.** Ten bins are used to discretize the particle field ( $N_s = 10$ ). The computational domain is of size  $20D \times 15D \times 4D$  and is comprised of  $500 \times 375 \times 100$  grid points in the  $x$ -,  $y$ -, and  $z$ -directions, respectively. The governing transport equations representing both the fluid and particle fields are solved using a MacCormack-based finite difference scheme [41, 42]. The scheme is of second order, accurate in time, and of fourth order, accurate in space. The boundary conditions are periodic in the span-wise  $z$ -direction and zero-derivative in the cross-stream  $y$ -direction and nonreflecting boundary conditions are used in both inflow and outflow boundaries ( $x$ -direction) [43]. The simulation is performed up to a nondimensional time of  $t^* = U_o t/D = 100$  which corresponds to a physical time of 0.48 ms. Both instantaneous and mean or averaged data are presented. We average in the  $z$ -direction as it is the spatially homogeneous direction in planar jets. Quantities such as contours, isosurfaces, and mean data are useful in making qualitative and quantitative assessments of the nanoparticle growth dynamics as well as the underlying fluid and particle fields.

**3.3. Flow Field.** The vorticity is the curl of the velocity vector and is an indicator of fluid mixing. The vorticity magnitude is the local rate of rotation. In nonpremixed chemically reacting flows, vorticity has the effect of increasing the interfacial area between the reactants. An isosurface of the instantaneous vorticity magnitude, the  $|\omega| = 3$  level-set, is shown in Figure 1 at time  $t^* = 100$ . The image shows that the flow is initially laminar and becomes turbulent as the jet travels downstream. Near  $x/D = 6$ , the two boundary layers initially located at  $y/D = \pm 0.5$  merge and the jet spreads across the domain. This is aided by the presence of vortex braids, the tubular structures oriented in the stream-wise  $x$ -direction, which act to draw the surrounding fluid into contact with the fluid issuing through the nozzle. Further downstream, vortex bending and stretching acts to generate small-scale structures as the flow becomes fully turbulent. It is evident that the jet suddenly spreads/amplifies near  $x/D = 8$ . Near  $x/D = 10$ , the contours reveal a high concentration of intense mixing that persists throughout the latter half of the computational domain. These small-scale structures result in an increased chemical reaction as they serve to bring the reactants into contact. High-resolution DNS facilitates the capturing of the small-scale structures. If turbulence models were used, then the effects of the small-scale interactions on the chemical reaction (and particle formation and growth) would need to be accounted for [18, 44].

**3.4. Titanium Dioxide.** The chemical conversion of the  $\text{TiCl}_4$  and  $\text{H}_2\text{O}$  to produce  $\text{TiO}_2$  is the first step in the particle synthesis process. Instantaneous contours of the  $\text{TiO}_2$  mass fraction at the  $z = 0$  plane and time  $t^* = 100$  are shown in Figure 2. The image reveals that  $\text{TiO}_2$  is initially formed along the interface of the two streams and subsequently where the reactants are well mixed. The  $\text{TiO}_2$  is convected downstream and across the jet. The maximum  $\text{TiO}_2$  mass fraction appears far downstream and  $\text{TiO}_2$  mass spreads out. Because of

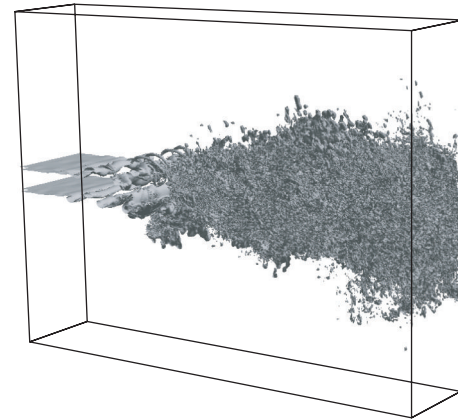


FIGURE 1: An instantaneous isosurface of the vorticity magnitude,  $|\omega| = 3$ , at time  $t^* = 100$ .

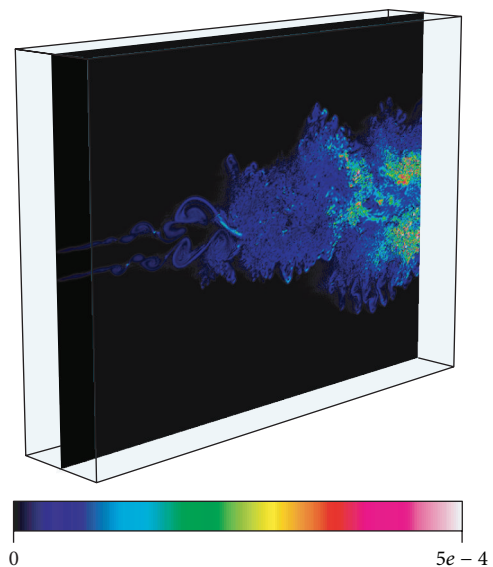


FIGURE 2: Instantaneous contour of the  $\text{TiO}_2$  mass fraction at  $z = 0$  plane at  $t^* = 100$ .

the infinite-rate chemistry, at least one of the reactants is consumed immediately upon contact. Turbulent mixing brings “fresh” reactants together (via large-scale transport) to produce  $\text{TiO}_2$  (via molecular scale transport). As the  $\text{TiO}_2$  is produced, molecular diffusion acts to transport it from  $\text{TiO}_2$ -rich to  $\text{TiO}_2$ -free regions.

**3.5. Particle Concentrations.** As the chemical reaction proceeds, more titania is produced. The monomers collide with each other to produce dimers; those dimers collide with monomers (condensation) to produce trimers and collide with each other to produce larger particles (coagulation). An advantage of the nodal approach is the fact that the particle field is obtained as a function of size (in addition to space and time). A detailed view of the  $\text{TiO}_2$  nanoparticle field can be obtained by observing the particle number concentrations distributed throughout the domain. Instantaneous contours

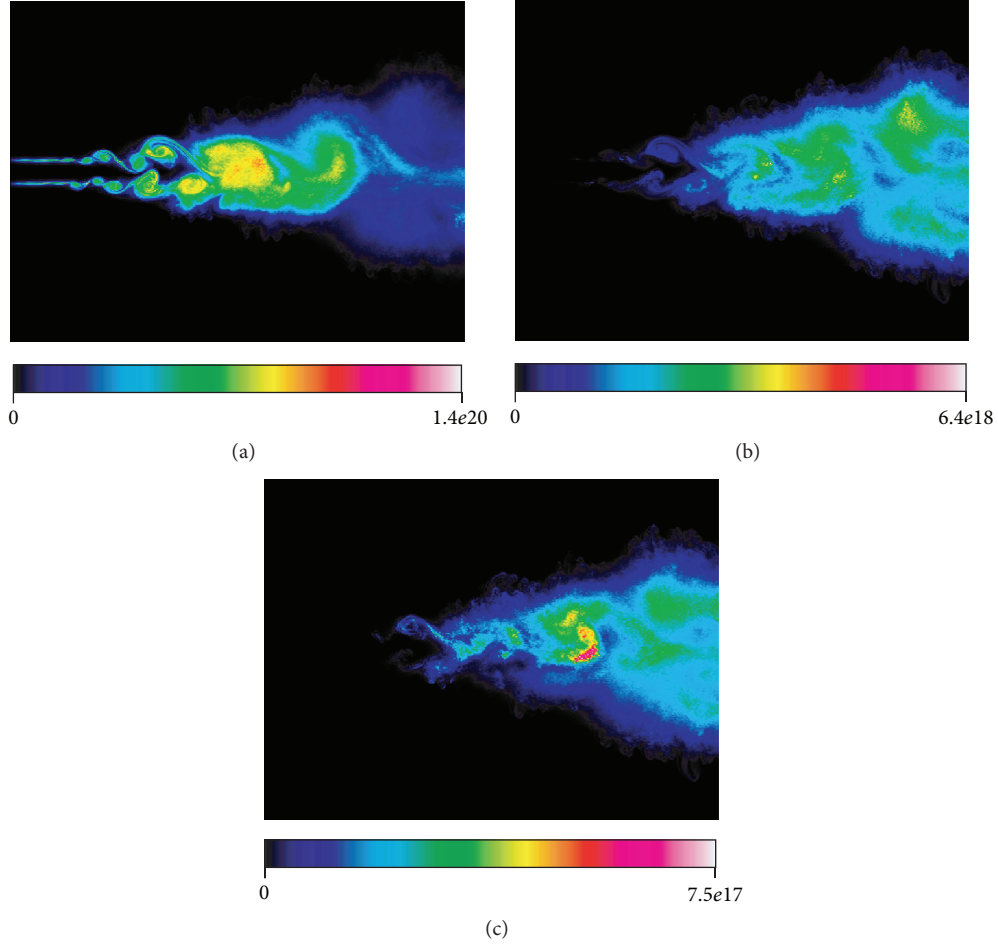


FIGURE 3: Instantaneous contours of the  $z$ -direction averaged particle number concentrations: (a) monomers; (b) 1 nm; (c) 2 nm.

of the  $z$ -direction averaged particle number concentrations of monomers, 1 nm and 2 nm particles at  $t^* = 100$ , are shown in Figure 3. Figure 3(a) shows that monomers initially appear at the interface of the two streams and the concentration increases significantly near  $x/D = 10$ , after collapse of the jet potential core. Figure 3(b) shows that the 1 nm diameter particles begin to appear near  $x/D = 5$ , and high concentrations are found between  $x/D = 10$  and  $x/D = 20$ . Figure 3(c) shows a similar trend for the 2 nm particles.

To convey the spatial inhomogeneity of the particle field, a three-dimensional view is presented in Figure 4. The figure shows three isosurfaces colored to show the large concentration of 1 nm, 2 nm, and 3 nm nanoparticles. The presence of 1 nm particles (colored green) throughout the domain reflects the ongoing chemical reaction and nucleation that occurs when large-scale convective mixing brings  $\text{TiCl}_4$  and  $\text{H}_2\text{O}$  into contact. The increase in particle size with downstream distance is evident in the image as the 3 nm diameter particles are only found in the last third of the domain.

**3.6. Mean Nanoparticle Size and Geometric Standard Deviation.** Particle size distributions (PSDs) are often characterized by the mean diameter and the geometric standard

deviation (GSD). Though the nodal approach employed contains the full PSD, conveying that all of the information is not trivial [45, 46], the information conveyed by the first two moments can be quite useful. The mean diameter used here is the volume-equivalent mean particle diameter and is given by  $d_p = (6v_p/\pi)^{1/3}$ , where the mean volume is given by

$$v_p = \frac{\sum_{i=1}^{N_s} Q_i v_i}{\sum_{i=1}^{N_s} Q_i}. \quad (10)$$

The GSD represents the width of the PSD and is given by

$$[\log(\sigma_g)]^2 = \frac{\sum_{k=1}^{N_s} Q_k (\log(d_{p_k}) - \log(\tilde{d}_{p_k}))^2}{\sum_{k=1}^{N_s} Q_k}, \quad (11)$$

where  $\tilde{d}_{p_k}$  is a number mean diameter given by

$$\log(\tilde{d}_{p_k}) = \frac{\sum_{k=1}^{N_s} Q_k \log(d_{p_k})}{\sum_{k=1}^{N_s} Q_k}. \quad (12)$$

Larger GSD values indicate that the size distribution is relatively broad while smaller GSD values ( $\sigma_g = 1$ ) indicate a relatively narrow distribution [47]. The GSD for the

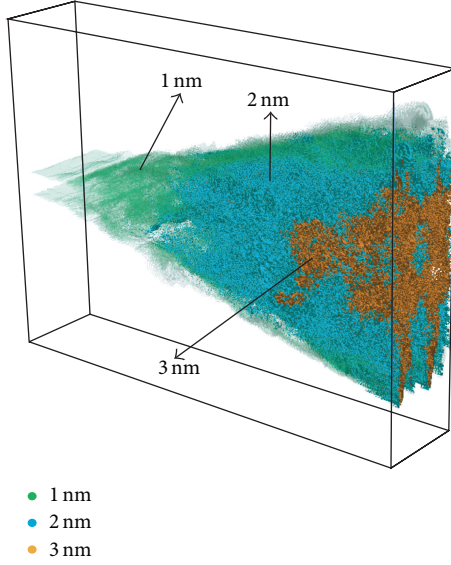


FIGURE 4: Instantaneous isosurfaces of 1 nm, 2 nm, and 3 nm particles at  $t^* = 100$ .

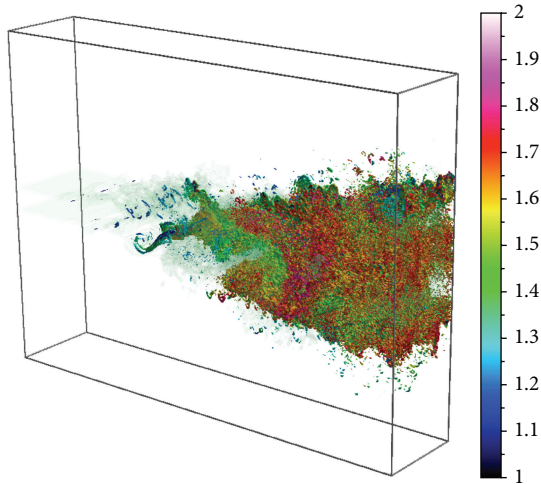


FIGURE 5: An instantaneous isosurface of vorticity colored by the geometric standard deviation,  $\sigma_g$ .

hydrolysis of  $\text{TiCl}_4$  in a planar jet is shown on an isosurface of vorticity magnitude at time  $t^* = 100$  in Figure 5. The figure reveals that the GSD generally increases as the jet travels downstream. This implies that mixing (due to turbulence) is a significant contribution to particle polydispersity. If nucleation were absent, there would be no monomers, and the coagulating particles would achieve the so-called self-preserving value ( $\sigma_g = 1.5$ ) [48, 49]. Locations where  $\sigma_g > 1.5$ , in Figure 5, reflect where nucleation, condensation, and coagulation simultaneously occur. That is, “newly” formed particles by nucleation/mixing and old particles generated by coagulation exist.

More insight into the particle field may be obtained by considering the relationship between the mean diameter and the GSD. A scatter plot of  $\sigma_g$  versus  $d_p$  is shown in Figure 6.

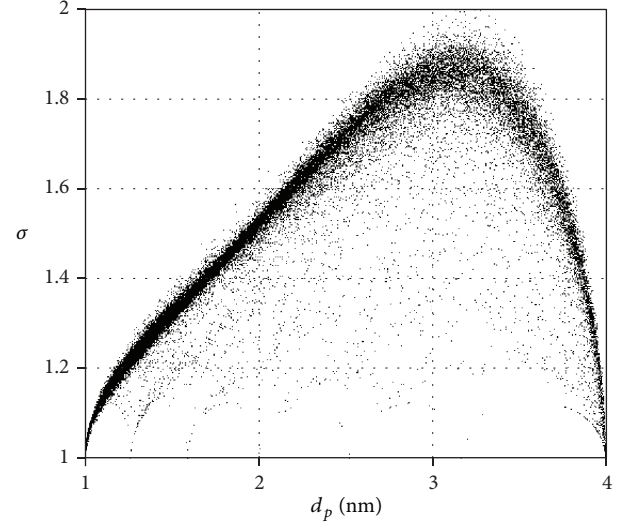


FIGURE 6: Scatter plot of the geometric standard deviation,  $\sigma_g$ , versus the mean particle diameter,  $d_p$ .

The figure shows that at the two ends of the size distribution,  $d_p = 1$  nm and  $d_p = 4$  nm, the distribution is fairly narrow or unimodal, while the GSD is largest ( $1.8 < \sigma_g < 2$ ) when the mean diameter is near  $d_p = 3.2$  nm. This relatively large GSD indicates that there are a variety of particle dynamics present in regions of the flow where the mean diameter is  $d_p = 3.2$  nm.

**3.7. Particle Growth.** The particle growth-rate is an important parameter to consider as, in combination with residence time or reactor size, it is a predictor of particle size. A diameter-based growth-rate  $\Omega_{nm}$  (with units of nm/s) is defined based on

$$\Omega_{nm} = \left( \frac{6\Omega}{\pi} \right)^{1/3} \times 10^9, \quad (13)$$

where  $\Omega$  is the particle volumetric growth-rate given by

$$\Omega = \frac{\sum_k^{N_s} (v_k)^2 \omega_k}{\sum_k^{N_s} Q_k v_k} - \frac{\sum_k^{N_s} (v_k)^2 Q_k}{\left( \sum_k^{N_s} Q_k v_k \right)^2} \sum_k^{N_s} v_k \omega_k. \quad (14)$$

A contour plot of the  $z$ -averaged growth-rate,  $\langle \Omega_{nm} \rangle_z$ , is shown in Figure 7. The figure shows that within the first 6 diameters,  $0 \leq x/D \leq 6$ , growth is confined to roughly  $\langle \Omega_{nm} \rangle_z = 10$  nm/s at the interface of the jet and the coflowing stream, where the hydrolysis reaction produces  $\text{TiO}_2$  vapor. Near  $x/D = 10$ , when the shear layers merge, the particles begin to grow faster, with the rate approaching  $\langle \Omega_{nm} \rangle_z = 25$  nm/s. This occurs after the potential core collapses. Further downstream, the growth-rate increases to roughly  $\langle \Omega_{nm} \rangle_z = 50$  nm/s and this value is maintained for  $x/D > 14$ . (It should be noted that this is the average growth-rate and at other points in the domain the values of  $\Omega_{nm}$  may be smaller or larger.)

The particles grow via two mechanisms: condensation (collisions between monomers and particles) and

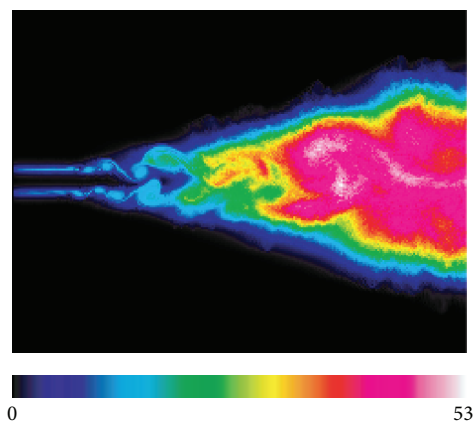


FIGURE 7: Instantaneous contours of the  $z$ -direction averaged particle growth-rate,  $\langle \Omega_{nm} \rangle_z$  at  $t^* = 100$ .

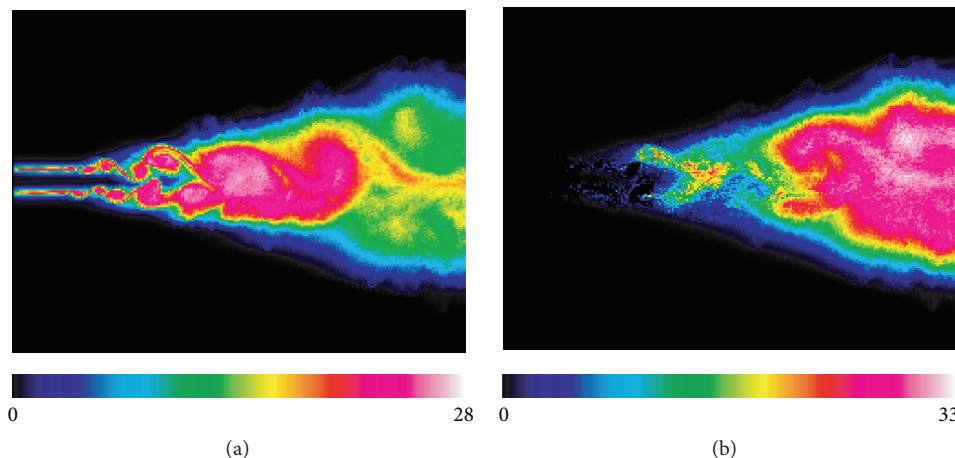


FIGURE 8: Instantaneous contours of the nanoparticle growth-rate decomposed by mechanism;  $z$ -direction averaged particle growth-rate (a) by condensation, (b) by coagulation.

coagulation (collisions between particles). Because the particle data is available as a function of size, the contribution of each mechanism is readily available. Particle growth, by mechanism, is shown in Figure 8. The interactions between monomers and particles, or the condensation growth-rate, is shown in Figure 8(a). (This image looks similar to the monomer number concentration shown in Figure 3(a) because the condensation is represented by the collision between monomers and particles.) The contours show that large condensation growth occurs both in the proximal region of the jet and after collapse of the jet core. This reflects the ongoing hydrolysis of  $\text{TiCl}_4$  and production of  $\text{TiO}_2$  and its deposition on existing particles.

Particle growth by coagulation is shown in Figure 8(b). The contours of the  $z$ -averaged growth-rate shows that growth by coagulation begins after collapse of the jet potential core. The growth-rate in the region  $4 < x/D < 8$  is as high as  $\Omega_{nm} = 16 \text{ nm/s}$ . Farther downstream the  $z$ -averaged

coagulation growth-rate doubles. This region of the flow is dominated by mixing and small-scale turbulence (evident in Figure 1). That region of the flow also contains particles of a variety of sizes, small and large, as reflected by  $\sigma_g$  in Figure 5. The small-scale turbulence means dissipation and increased residence times, while the disparate particle sizes mean an efficient collision efficiency. These two combine to increase coagulation.

The spatial relationship between condensation growth and coagulation growth is elucidated by showing the contribution of each at every grid point in the computational domain. A scatter plot of the two growth-rates is shown in Figure 9. The growth-rates are not averaged in the  $z$ -direction and while a spatial relationship is not directly evident from this figure, one may be reliably inferred along with the previous data. Figure 9 shows that where condensation growth is low, coagulation growth is high. This trend is evident in Figure 8 as well. However, Figure 9 shows that in these regions the coagulation growth-rate can be as much as an



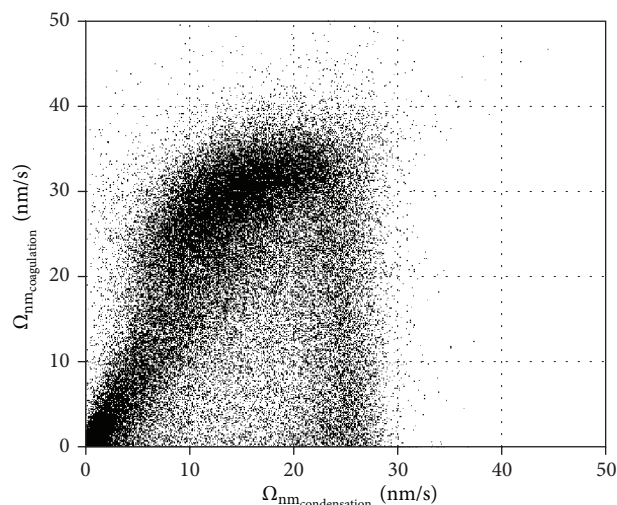


FIGURE 9: Scatter plot of the particle growth-rate by condensation versus the particle growth-rate by coagulation.

order of magnitude greater than the condensation growth-rate.

#### 4. Summary and Conclusions

The growth mechanisms of titania during hydrolysis of titanium tetrachloride in a three-dimensional planar jet are studied via direct numerical simulation. The mass, momentum, enthalpy, and species transport equations are solved in a model-free manner. Titania was produced via the hydrolysis of titanium tetrachloride, modeled via a 1-step infinitely fast chemical mechanism. The particle field was represented using a nodal method and solves for the evolution of the concentration of particles of various sizes in an Eulerian manner. When coupled to the Navier-Stokes solver, the fluid, thermal, chemical, and particle fields are obtained as a function of space and time.

The results show that fluid turbulence/gas mixing plays a very important role in particle growth. The results indicate that the particle formation and growth are greatly affected if not dominated by mixing and chemical reaction. Reactant conversion or titania production is limited by the ability of the flow to bring the  $\text{TiCl}_4$  and  $\text{H}_2\text{O}$  into contact. Evidence for this is the particle formation throughout the domain. Additionally, the results show that where the turbulence is more intense, the particles are larger and the particle size distribution, as characterized by the geometric standard deviation, is wider. Particle growth in the proximal region of the jet is dominated by condensation. After collapse of the jet core, nanoparticle growth due to coagulation increases significantly. Though  $\text{TiO}_2$  is produced after core collapse, producing condensable species, particle growth due to coagulation is as much as an order of magnitude greater than that due to condensation. While both condensation and coagulation act to increase polydispersity, coagulation has been shown to increase the width of the particle size distribution faster, or greater, than condensation [50].

These results help to shed light on, and improve our understanding of, the underlying growth dynamics occurring in nanoparticle synthesis processes. The change from condensation-dominated to coagulation-dominated growth is useful in modeling the complete synthesis process, including sintering, and the formation of hard and soft agglomerates. Spanning the size range from single molecules (particle inception) to hundreds of nanometers, as the particles found in many industrial processes and applications, is compute intensive [18]. However, knowing that condensation and molecular growth is relatively minor could facilitate the use of more affordable modeling strategies that do not need to account for every phenomena [6, 51]. Additionally, a highly desired attribute of metal oxide nanoparticles is their specific surface area. The ability to synthesize narrow size distributions which are desired is advantageous in that it removes the processing necessary to separate particles by size. This is advantageous in that it lowers cost [52–55].

One strategy to reduce polydispersity may be to delay the transition to turbulence via a vis delaying collapse of the jet core. While the particle field is known as a function of size, it should be noted that in this work we are unable to distinguish the various phases of titania, rutile, anatase, or brookite [56, 57]. The phase composition of titania is very much a function of the synthesis process, for example, precursor composition and temperature history, which are greatly simplified in this work. Such capability requires phenomenological models that account for particle dynamics as a function of space, time, and temperature, as well as solid-state diffusion processes, and is quite beyond the scope of this work.

#### Conflict of Interests

The author declares that there is no conflict of interests regarding the publication of this paper.

#### Acknowledgments

Funding for this research was provided by the University of Minnesota. Computational resources were provided by Minnesota Supercomputing Institute.

#### References

- [1] S. E. Pratsinis and S. Vemury, "Particle formation in gases: a review," *Powder Technology*, vol. 88, no. 3, pp. 267–273, 1996.
- [2] G. Beaucage, H. Kammler, P. Mueller et al., "Probing the dynamics of nanoparticle growth in a flame using synchrotron radiation," *Nature Materials*, vol. 3, no. 6, pp. 370–373, 2004.
- [3] S. Panda and S. E. Pratsinis, "Modeling the synthesis of aluminum particles by evaporation-condensation in an aerosol flow reactor," *Nanostructured Materials*, vol. 5, no. 7-8, pp. 755–767, 1995.
- [4] S. Yuu, K. Ikeda, and T. Umekage, "Flow-field prediction and experimental verification of low Reynolds number gas-particle turbulent jets," *Colloids and Surfaces A: Physicochemical and Engineering Aspects*, vol. 109, pp. 13–27, 1996.
- [5] S. Tsantilis, H. K. Kammler, and S. E. Pratsinis, "Population balance modeling of flame synthesis of titania nanoparticles,"

- Chemical Engineering Science*, vol. 57, no. 12, pp. 2139–2156, 2002.
- [6] N. Settumba and S. C. Garrick, “Direct numerical simulation of nanoparticle coagulation in a temporal mixing layer via a moment method,” *Journal of Aerosol Science*, vol. 34, no. 2, pp. 149–167, 2003.
- [7] D. L. Marchisio and R. O. Fox, “Solution of population balance equations using the direct quadrature method of moments,” *Journal of Aerosol Science*, vol. 36, pp. 43–73, 2005.
- [8] F. Aristizabal, R. J. Munz, and D. Berk, “Modeling of the production of ultra fine Aluminium particles in rapid quenching turbulent flow,” *Journal of Aerosol Science*, vol. 37, no. 2, pp. 162–186, 2006.
- [9] S. Rigopoulos, “PDF method for population balance in turbulent reactive flow,” *Chemical Engineering Science*, vol. 62, no. 23, pp. 6865–6878, 2007.
- [10] K. Zhou, A. Attili, A. Alshaarawi, and F. Bisetti, “Simulation of aerosol nucleation and growth in a turbulent mixing layer,” *Physics of Fluids*, vol. 26, no. 6, Article ID 065106, 2014.
- [11] S. A. Orszag and I. Staroselsky, “CFD: progress and problems,” *Computer Physics Communications*, vol. 127, no. 1, pp. 165–171, 2000.
- [12] K. Nakaso, T. Fujimoto, T. Seto, M. Shimada, K. Okuyama, and M. M. Lunden, “Size distribution change of titania nanoparticle agglomerates generated by gas phase reaction, agglomeration, and sintering,” *Aerosol Science and Technology*, vol. 35, no. 5, pp. 929–947, 2001.
- [13] T. Johannessen, S. E. Pratsinis, and H. Livbjerg, “Computational analysis of coagulation and coalescence in the flame synthesis of titania particles,” *Powder Technology*, vol. 118, no. 3, pp. 242–250, 2001.
- [14] E. G. Moody and L. R. Collins, “Effect of mixing on the nucleation and growth of titania particles,” *Aerosol Science and Technology*, vol. 37, no. 5, pp. 403–424, 2003.
- [15] G. Wang and S. C. Garrick, “Modeling and simulation of titania formation and growth in temporal mixing layers,” *Journal of Aerosol Science*, vol. 37, no. 4, pp. 431–451, 2006.
- [16] S. Das and S. C. Garrick, “The effects of turbulence on nanoparticle growth in turbulent reacting jets,” *Physics of Fluids*, vol. 22, no. 10, Article ID 103303, 2010.
- [17] S. C. Garrick, “Effects of turbulent fluctuations on nanoparticle coagulation in shear flows,” *Aerosol Science and Technology*, vol. 45, no. 10, pp. 1272–1285, 2011.
- [18] A. J. Fager, J. Liu, and S. C. Garrick, “Hybrid simulations of metal particle nucleation: a priori and a posteriori analyses of the effects of unresolved scalar interactions on nanoparticle nucleation,” *Physics of Fluids*, vol. 24, no. 7, Article ID 075110, 2012.
- [19] N. J. Murfield and S. C. Garrick, “Large eddy simulation and direct numerical simulation of homogeneous nucleation in turbulent wakes,” *Journal of Aerosol Science*, vol. 60, pp. 21–33, 2013.
- [20] N. J. Murfield and S. C. Garrick, “The effects of unresolved scalar fluctuations during homogeneous nucleation,” *Aerosol Science and Technology*, vol. 47, no. 7, pp. 806–817, 2013.
- [21] P. Givi, “Model free simulations of turbulent reactive flows,” *Progress in Energy and Combustion Science*, vol. 15, no. 1, pp. 1–107, 1989.
- [22] K. E. J. Lehtinen and M. R. Zachariah, “Self-preserving theory for the volume distribution of particles undergoing brownian coagulation,” *Journal of Colloid and Interface Science*, vol. 242, no. 2, pp. 314–318, 2001.
- [23] S. C. Garrick, K. E. J. Lehtinen, and M. R. Zachariah, “Nanoparticle coagulation via a Navier-Stokes/nodal methodology: evolution of the particle field,” *Journal of Aerosol Science*, vol. 37, no. 5, pp. 555–576, 2006.
- [24] F. Gelbard and J. H. Seinfeld, “Simulation of multicomponent aerosol dynamics,” *Journal of Colloid And Interface Science*, vol. 78, no. 2, pp. 485–501, 1980.
- [25] P. Biswas, C. Y. Wu, M. R. Zachariah, and B. McMillin, “Characterization of iron oxide-silica nanocomposites in flames: part II: comparison of discrete-sectional model predictions to experimental data,” *Journal of Materials Research*, vol. 12, no. 3, pp. 714–723, 1997.
- [26] K. E. J. Lehtinen and M. R. Zachariah, “Energy accumulation in nanoparticle collision and coalescence processes,” *Journal of Aerosol Science*, vol. 33, no. 2, pp. 357–368, 2002.
- [27] G. Wang and S. C. Garrick, “Modeling and simulation of titania formation and growth in temporal mixing layers,” *Journal of Aerosol Science*, vol. 37, no. 4, pp. 431–451, 2006.
- [28] J. Loeffler, S. Das, and S. C. Garrick, “Large eddy simulation of titanium dioxide nanoparticle formation and growth in turbulent jets,” *Aerosol Science and Technology*, vol. 45, no. 5, pp. 616–628, 2011.
- [29] K. S. Friedlander, *Smoke, Dust and Haze: Fundamentals of Aerosol Dynamics*, Oxford University Press, New York, NY, USA, 2000.
- [30] M. Frenklach and S. J. Harris, “Aerosol dynamics modeling using the method of moments,” *Journal of Colloid and Interface Science*, vol. 118, no. 1, pp. 252–261, 1987.
- [31] S. E. Pratsinis, “Particle production by gas-to-particle conversion in turbulent flows,” *Journal of Aerosol Science*, vol. 20, no. 8, pp. 1461–1464, 1989.
- [32] J. D. Landgrebe and S. E. Pratsinis, “A discrete-sectional model for particulate production by gas-phase chemical reaction and aerosol coagulation in the free-molecular regime,” *Journal of Colloid and Interface Science*, vol. 139, no. 1, pp. 63–86, 1990.
- [33] G. Wang and S. C. Garrick, “Modeling and simulation of titania synthesis in two-dimensional methane-air flames,” *Journal of Nanoparticle Research*, vol. 7, no. 6, pp. 621–632, 2005.
- [34] G. W. Mulholland, R. J. Samson, R. D. Mountain, and M. H. Ernst, “Cluster size distribution for free molecular agglomeration,” *Energy & Fuels*, vol. 2, no. 4, pp. 481–486, 1988.
- [35] J. Cai, N. Lu, and C. M. Sorensen, “Analysis of fractal cluster morphology parameters: structural coefficient and density autocorrelation function cutoff,” *Journal of Colloid And Interface Science*, vol. 171, no. 2, pp. 470–473, 1995.
- [36] R. Jullien and P. Meakin, “Simple models for the restructuring of three-dimensional ballistic aggregates,” *Journal of Colloid And Interface Science*, vol. 127, no. 1, pp. 265–272, 1989.
- [37] S. N. Rogak and R. C. Flagan, “Coagulation of aerosol agglomerates in the transition regime,” *Journal of Colloid and Interface Science*, vol. 151, no. 1, pp. 203–224, 1992.
- [38] S. Modem, S. C. Garrick, M. R. Zachariah, and K. E. J. Lehtinen, “Direct numerical simulation of nanoparticle coagulation in a temporal mixing layer,” in *Proceedings of the 29th Symposium (International) on Combustion*, pp. 1071–1077, The Combustion Institute, Pittsburgh, Pa, USA, 2002.
- [39] S. C. Garrick and G. Wang, “Modeling and simulation of titanium dioxide nanoparticle synthesis with finite-rate sintering in planar jets,” *Journal of Nanoparticle Research*, vol. 13, no. 3, pp. 973–984, 2011.

- [40] M. C. Heine and S. E. Pratsinis, "Polydispersity of primary particles in agglomerates made by coagulation and sintering," *Journal of Aerosol Science*, vol. 38, no. 1, pp. 17–38, 2007.
- [41] R. W. MacCormack, "The effect of viscosity in hypervelocity impact catering," AIAA Paper 69-354, 1969.
- [42] M. H. Carpenter, "A high-order compact numerical algorithm for supersonic flows," in *Twelfth International Conference on Numerical Methods in Fluid Dynamics*, K. W. Morton, Ed., vol. 371 of *Lecture Notes in Physics*, pp. 254–258, Springer, Berlin, Germany, 1990.
- [43] D. H. Rudy and J. C. Strikwerda, "Boundary conditions for subsonic compressible navier-stokes calculations," *Computers and Fluids*, vol. 9, no. 3, pp. 327–338, 1981.
- [44] P. Givi, "Filtered density function for subgrid scale modeling of turbulent combustion," *AIAA Journal*, vol. 44, no. 1, pp. 16–23, 2006.
- [45] S. Modem and S. C. Garrick, "Nanoparticle coagulation in a temporal mixing layer mean and size-selected images," *Journal of Visualization*, vol. 6, no. 3, pp. 293–302, 2003.
- [46] D. L. Wright, S. Yu, P. S. Kasibhatla et al., "Retrieval of aerosol properties from moments of the particle size distribution for kernels involving the step function: cloud droplet activation," *Journal of Aerosol Science*, vol. 33, no. 2, pp. 319–337, 2002.
- [47] H. K. Kammler, R. Jossen, P. W. Morrison Jr., S. E. Pratsinis, and G. Beaucage, "The effect of external electric fields during flame synthesis of titania," *Powder Technology*, vol. 135-136, pp. 310–320, 2003.
- [48] W. C. Hinds, *Aerosol Technology: Properties, Behavior and Measurement of Air-Borne Particles*, John Wiley & Sons, New York, NY, USA, 2nd edition, 1999.
- [49] N. Settumba and S. C. Garrick, "A comparison of diffusive transport in a moment method for nanoparticle coagulation," *Journal of Aerosol Science*, vol. 35, no. 1, pp. 93–101, 2004.
- [50] S. E. Pratsinis, "Simultaneous nucleation, condensation, and coagulation in aerosol reactors," *Journal of Colloid And Interface Science*, vol. 124, no. 2, pp. 416–427, 1988.
- [51] R. McGraw, "Description of aerosol dynamics by the quadrature method of moments," *Aerosol Science and Technology*, vol. 27, no. 2, pp. 255–265, 1997.
- [52] J. Bai, Y.-H. Xu, and J.-P. Wang, "Cubic and spherical high-moment FeCo nanoparticles with narrow size distribution," *IEEE Transactions on Magnetics*, vol. 43, no. 7, pp. 3340–3342, 2007.
- [53] A. Khorsand Zak, R. Razali, W. H. Abd Majid, and M. Darroudi, "Synthesis and characterization of a narrow size distribution of zinc oxide nanoparticles," *International Journal of Nanomedicine*, vol. 6, no. 1, pp. 1399–1403, 2011.
- [54] M. Asemi and M. Ghanaatshoar, "Preparation of CuCrO<sub>2</sub> nanoparticles with narrow size distribution by sol-gel method," *Journal of Sol-Gel Science and Technology*, vol. 70, no. 3, pp. 416–421, 2014.
- [55] A. M. Ahadi, O. Polonskyi, U. Schürmann, T. Strunskus, and F. Faupel, "Stable production of TiO<sub>x</sub> nanoparticles with narrow size distribution by reactive pulsed dc magnetron sputtering," *Journal of Physics D: Applied Physics*, vol. 48, no. 3, Article ID 035501, 2015.
- [56] W. W. So, S. B. Park, K. J. Kim, C. J. Shin, and S. J. Moon, "The crystalline phase stability of titania particles prepared at room temperature by the sol-gel method," *Journal of Materials Science*, vol. 36, no. 17, pp. 4299–4305, 2001.
- [57] A. Teleki, R. Wengeler, L. Wengeler, H. Nirschl, and S. E. Pratsinis, "Distinguishing between aggregates and agglomerates of flame-made TiO<sub>2</sub> by high-pressure dispersion," *Powder Technology*, vol. 181, no. 3, pp. 292–300, 2008.



## Research Article

# Preparation of ZnO/CdS/BC Photocatalyst Hybrid Fiber and Research of Its Photocatalytic Properties

**Beibei Dai, Cheng Chao, Xiaoyu Lu, Qingcheng Xia, Jing Han, Fei Mao, Jiazhi Yang, and Dongping Sun**

*Chemicobiology and Functional Materials Institute, Nanjing University of Science and Technology, Nanjing 210094, China*

Correspondence should be addressed to Jiazhi Yang; [jzhyangb504@163.com](mailto:jzhyangb504@163.com)

Received 6 May 2015; Revised 3 July 2015; Accepted 9 July 2015

Academic Editor: Enkelela Dervishi

Copyright © 2015 Beibei Dai et al. This is an open access article distributed under the Creative Commons Attribution License, which permits unrestricted use, distribution, and reproduction in any medium, provided the original work is properly cited.

An environment-friendly biomaterial bacterial cellulose (BC) is introduced to substitute general organic polymers to assist the preparation of ZnO/CdS/BC photocatalyst hybrid nanofiber through coprecipitation method under the low-temperature condition. The XRD, XPS, and SEM results show that high load of ZnO/CdS/BC ternary hybrid fiber can be produced. TGA curves scan shows that ZnO/CdS/BC hybrid fiber has better thermal properties than bacterial cellulose. The UV-Vis spectra of the ZnO/CdS/BC hybrid nanofiber (0, 10, 20, and 50 wt%, resp.) show that photocatalytic activities of ZnO/CdS/BC are influenced by the added amount of CdS. The degradation curve of methyl shows that ZnO/CdS/BC nanohybrid fibers exhibit excellent photocatalytic efficiency.

## 1. Introduction

Zinc oxide (ZnO) is deemed to be one of the most important photocatalysts because of its high photosensitivity, nontoxicity, and great stability [1–5]. However, it is known that ZnO could not effectively absorb and utilize the visible region of the solar light, because of the fast recombination of the photogenerated electron hole pairs in the single phase semiconductor [6, 7]. CdS, as a representative II–VI compound semiconductor, has been used as a visible-light photocatalyst [8] and also as a photosensitizer of various wide band-gap semiconductor photoanodes in photoelectrochemical cells due to its narrow direct band-gap (2.4 eV) [9]. However, it is very easy etching, resulting in the decreased service life [10, 11]. The combined ZnO and CdS system in nanosize area has attracted a great deal of attention in recent years. It can enhance the photocatalytic efficiency of ZnO under visible light and the service life of CdS, due to the fast separation of the photogenerated electron hole pairs [12–17].

However, there are disadvantages such as the aggregation and the bleeding of the photocatalyst of the CdS/ZnO suspended photocatalyst. It can be overcome through the photocatalyst fixation instead of the recovery of the photocatalyst [10–20]. The key of immobilized technique is

the performance of adopted immobilized carriers. Selection of carriers for supported CdS/ZnO suspended photocatalyst was systematically studied in earlier reports. Glass cloth, activated carbon, refractory brick, sand particle, hollow glass beads, ceramic, silica, and so forth are common catalyst supporters with broad application potentials [19]. However, the absorption and activity of catalyst could be decreased by using such supporter for immobilization of catalyst due to their low specific surface area and nonhomogeneous porosity. In order to improve the performance of the catalyst, nanometer fiber/nanotubes as the catalyst supporters have been conducted recently. As a new kind of materials, nanometer fiber/nanotubes carriers have attracted considerable interest because of their unique structural, mechanic, electronic, and potential applications [21].

Cellulose is one of the most abundant natural resources. Bacterial cellulose (BC) fiber produced by *Acetobacter xylinum* is considered as a cleaner sustainable biomaterial and attracts much attention due to its remarkable advantages of good mechanic properties, good chemical stability, high purity, high specific surface area, high crystallinity, great compatibility, and being environmentally friendly [22]. The diameter of BC fiber is common of 10–100 nm. It has been found that biomaterials were widely used as

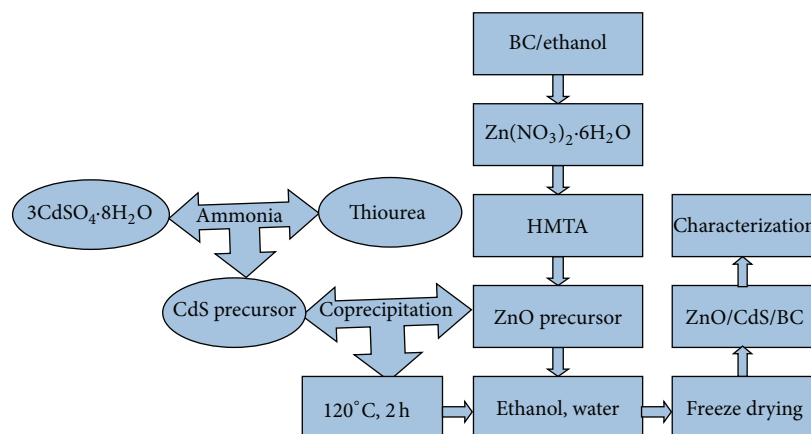


FIGURE 1: Schematic preparation process of hybrid ZnO/CdS/BC fibers.

a template in the synthesis of various inorganic nanostructures. Various methods have been reported for the synthesis of ZnO/CdS nanorods including colloidal chemical synthesis [16], electrochemical deposition [23], chemical bath deposition technique [24], facile chemical route [25], combined sol-gel/hydrothermal/SILAR method [26], chemical precipitation method [27], and sonochemical synthesis [28]. Among these methods, coprecipitation process is a simple and low-cost method that can be performed at low temperature and ambient pressure.

In this study, we used BC as template to prepare ZnO/CdS/BC ternary hybrid fiber. The samples were characterized by X-ray diffraction (XRD), scanning electron microscopy (SEM), thermogravimetric analysis (TGA), X-ray photoelectron spectra (XPS), UV-Vis absorption spectroscopy (UV-Vis), and the photocatalytic activity measurements. This study would provide a new type of nanofiber photocatalysis materials. It also opened up a new field of potential applications of BC materials.

## 2. Experimental

**2.1. Materials.** Bacterial cellulose (BC) was biosynthesized by *Acetobacter xylinum* NUST5.2. The cadmium sulfate octahydrate ( $3\text{CdSO}_4 \cdot 8\text{H}_2\text{O}$ ) was purchased from Guangdong Company (Guangdong, China). Analytical-grade sodium hydroxide (NaOH), zinc nitrate hexahydrate ( $\text{Zn}(\text{NO}_3)_2 \cdot 6\text{H}_2\text{O}$ ), hexamethylenetetramine (HMTA), ethanol ( $\text{C}_2\text{H}_5\text{OH}$ ), ammonia water ( $\text{NH}_3 \cdot \text{H}_2\text{O}$ ), dibasic sodium phosphate ( $\text{Na}_2\text{HPO}_4$ ), glucose ( $\text{C}_6\text{H}_{12}\text{O}_6$ ) were purchased from Sinopharm Chemical Reagent Co., Ltd. All aqueous solutions were prepared with deionized water produced by laboratory water purification system. All other chemicals were analytical reagent unless stated otherwise.

**2.2. Preparation of BC Fibers.** The pristine BC substrate was synthesized and purified as reported [29]. BC fibers were purified by soaking in DI at  $70^\circ\text{C}$  for 3 h and then 4 wt% NaOH in DI at  $80^\circ\text{C}$  for 180 min. Samples were then rinsed

with DI to pH = 7 and stored in refrigerator at  $4^\circ\text{C}$  prior to use.

**2.3. Preparation of Hybrid ZnO/CdS/BC Fibers.** Figure 1 showed the preparation process of hybrid ZnO/CdS/BC fibers. In a typical procedure, the BC fibers were immersed in the ethanol solution with certain concentrations under magnetic stirring. Then, the BC fibers were dipped into an ethanol solution containing 0.5 g zinc nitrate hexahydrate [ $\text{Zn}(\text{NO}_3)_2 \cdot 6\text{H}_2\text{O}$ ] with mechanical stirring (200 rpm) at  $30^\circ\text{C}$  for 10 h. Subsequently, hexamethylenetetramine (HMTA) was added into the above solvent and treated with ultrasonic for 1 h. Finally, different amounts of cadmium sulfate octahydrate [ $3\text{CdSO}_4 \cdot 8\text{H}_2\text{O}$ ] (0.01 g/mL) solution including 5 mL, 10 mL, and 25 mL were added to the above as-prepared ZnO solution and labeled as 10 wt% ZnO/CdS/BC, 20 wt% ZnO/CdS/BC, and 50 wt% ZnO/CdS/BC, respectively. The mixture was stirred at  $120^\circ\text{C}$  temperature for another 12 h. The products were washed with distilled water and ethanol for several times to remove the possible residues and were dried in vacuum at  $50^\circ\text{C}$  for 24 h. After the reaction, the white solution turned light yellow with the CdS content increasing, indicating the formation of hybrid ZnO/CdS/BC fibers.

**2.4. Characterization of Samples.** The X-ray diffraction patterns (XRD) were recorded on a Bruker D8 ADVANCE X-ray diffractometer equipped with graphite monochromatized high-intensity  $\text{CuK}\alpha$  radiation ( $\lambda = 0.15418 \text{ nm}$ ). Scanning electron microscopy (SEM) images were performed on JSM-6380LV to obtain the morphology of the samples. The UV-visible spectra were recorded on a Cary 5000 spectrophotometer equipped with an integrated sphere accessory for diffusive reflectance spectra. Thermogravimetric analyses (TGA) were performed on a Boyuan DTU-2C thermogravimetric analyzer from  $50$  to  $800^\circ\text{C}$  at a heating rate of  $10^\circ\text{C} \cdot \text{min}^{-1}$  in air flow. High resolution XPS and wide XPS spectra were achieved to investigate the composition and chemical states of the samples. X-ray photoelectron

spectra (XPS) were carried out on a RBD upgraded PHI-5000C ESCA system (Perkin Elmer) with Mg K $\alpha$  radiation ( $h\nu = 1253.6$  eV). The XPS peaks were deconvoluted using Lorentzian-Gaussian components after a Shirley background subtraction.

**2.5. Photocatalytic Activity Measurements.** The photocatalytic activities of the samples were evaluated by photodegradation of the methyl orange under a simulated sunlight from a 500 W Xe lamp at room temperature. The reaction suspensions formed by 20 mg ZnO/CdS/BC hybrid nanofiber (10%) and 40 mL methyl orange (20 mg/L). Prior to irradiation, the suspensions were stirred in the dark for 30 min to achieve the adsorption/desorption equilibrium. After a given irradiation time, a small amount of the solution was withdrawn for analysis of the methyl orange concentration after centrifuging. The photodegradation of the methyl orange solution was investigated by measuring its absorbance by the UV-Vis spectrophotometer (Evolution 220) at the maximum absorption around  $\lambda_{\max} = 500$  nm. A good linear relationship between the concentration and absorbance at low concentration is presented according to Lambert-Beer's law:

$$\eta = \frac{C_0 - C_t}{C_0} \times 100\% = \frac{A_0 - A_t}{A_0} \times 100\%, \quad (1)$$

where  $C_0$  is the initial concentration of methyl orange solution,  $A_0$  means the initial absorbance,  $C_t$  is the concentration at the  $t$  moment, and  $A_t$  is the concentration at the moment.

### 3. Results and Discussion

**3.1. X-Ray Diffraction Patterns (XRD).** The XRD patterns of bacterial cellulose, pure ZnO, and ZnO/BC hybrid fiber are described in Figure 2. Figure 2(a) shows the pronounced diffraction peaks with  $2\theta = 14.5^\circ$ ,  $16.6^\circ$ , and  $22.5^\circ$  corresponding to the (101), (101 $^-$ ), and (002) planes of the BC fibers [22]. Figure 2(c) shows the peaks of pure ZnO nanorod. It indicates that the presence of ZnO nanorod attributes to peaks at  $2\theta = 31.8^\circ$ ,  $34.4^\circ$ ,  $36.3^\circ$ ,  $47.5^\circ$ ,  $56.6^\circ$ ,  $62.9^\circ$ ,  $66.4^\circ$ ,  $68.0^\circ$ , and  $69.1^\circ$ . These are associated with the (100), (002), (101), (102), (110), (103), (200), (112), and (201) planes of the ZnO hexagonal wurtzite structure [9]. Figure 2(b) shows XRD patterns of ZnO/BC hybrid nanofiber. It can be seen that all diffraction peaks could be identified to BC fibers and ZnO peaks with hexagonal wurtzite structure. No other peaks related to impurities are detected in the pattern which further confirms that the synthesized hybrid nanofibers were BC and single phase of ZnO with hexagonal wurtzite structure. Meanwhile, three characteristic peaks located at  $14.5^\circ$ ,  $16.6^\circ$ , and  $22.5^\circ$  from BC fibers are weakened due to a lot of nanorods wrapped on the surface of BC fibers.

Figure 3 presents the XRD patterns of the ZnO/CdS/BC hybrid fiber. There are two sets of diffraction peaks for ZnO/CdS/BC nanoheterostructure, which can be ascribed to hexagonal wurtzite ZnO and cubic CdS, respectively. In contrast to the standard diffraction peaks (JCPDS number 36-1451), the pronounced and high diffraction peaks with

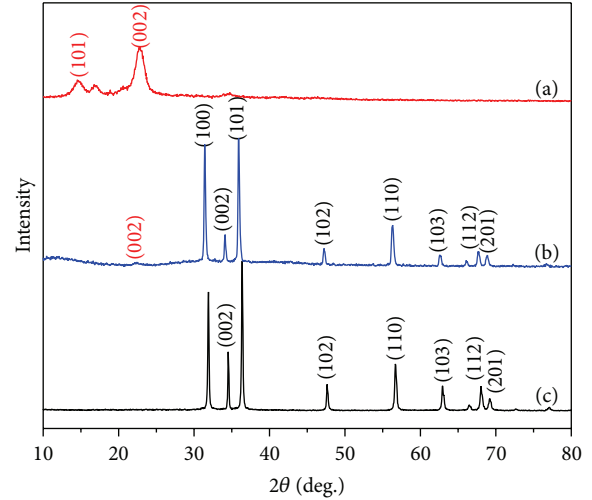


FIGURE 2: XRD patterns of (a) bacterial cellulose, (b) ZnO/BC hybrid fiber, and (c) ZnO.

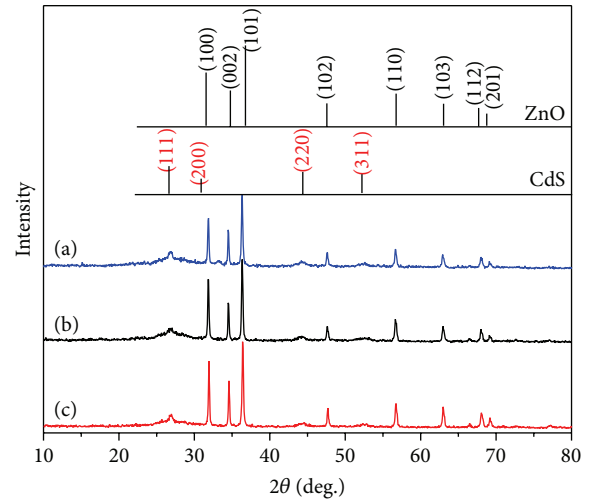


FIGURE 3: XRD patterns of (a) ZnO/CdS/BC hybrid fiber (50%), (b) ZnO/CdS/BC hybrid fiber (20%), and (c) ZnO/CdS/BC hybrid fiber (10%).

$2\theta = 31.8^\circ$ ,  $34.4^\circ$ ,  $36.3^\circ$ ,  $47.5^\circ$ ,  $56.6^\circ$ ,  $62.9^\circ$ ,  $66.4^\circ$ ,  $68.0^\circ$ , and  $69.1^\circ$  correspond to the (100), (002), (101), (102), (110), (103), (200), (112), and (201) planes of the hexagonal ZnO, respectively [9]. Meanwhile, broader and weaker diffraction peaks with  $2\theta = 26.5^\circ$ ,  $43.9^\circ$ , and  $52.0^\circ$  are observed and they are found to be consistent with those of the standard CdS (JCPDS number 89-0440), corresponding to the (111), (220), and (311) planes of the CdS, respectively, suggesting the existence of ZnO and CdS [8]. And the ZnO diffraction peaks get weaker with increasing contents of CdS. It implies the highly crystalline character of ZnO and the little crystal size of CdS in the sample.

**3.2. Scanning Electron Microscopy (SEM).** The morphologies of BC and ZnO/CdS/BC hybrid nanofiber (10, 20, and 50 wt%, resp.) structure are investigated by SEM.



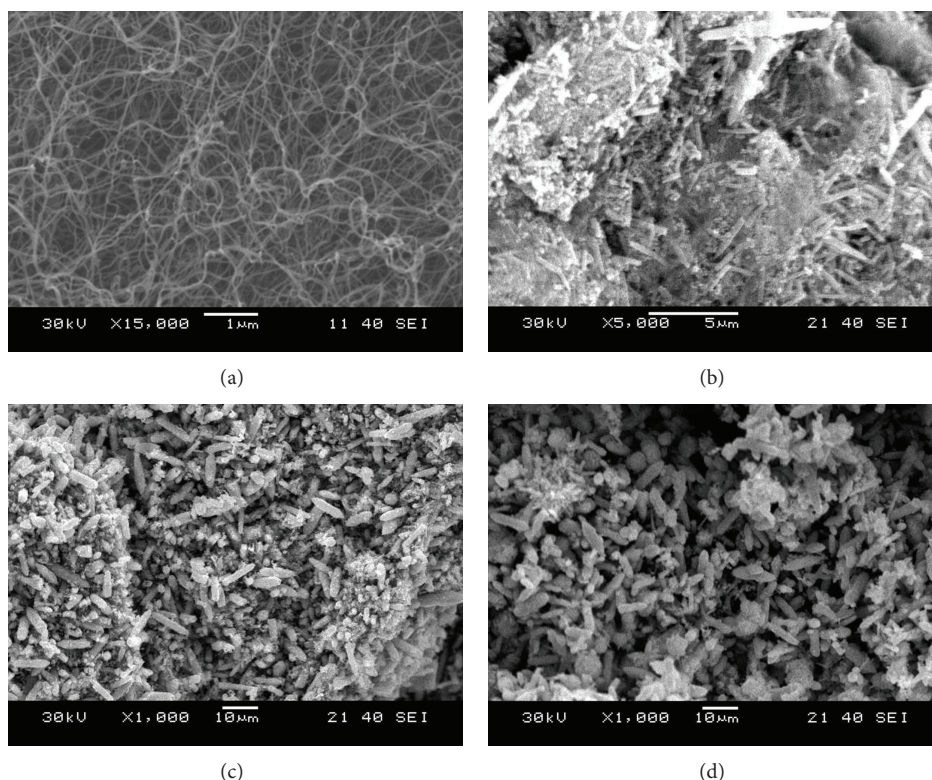


FIGURE 4: (a) SEM of bacterial cellulose and ((b)–(d)) samples prepared at 120°C with CdS contents at 10%, 20%, and 50%.

Figure 4(a) shows SEM images of bacterial cellulose nanofibers biosynthesized by *Acetobacter xylinum* NUST 5.2. It presents a three-dimensional network structure with an average diameter of about 30 nm. The three-dimensional network structure contains a lot of lone pair electrons in the hydroxyl groups, which play an active role in anchoring the nanoparticles. Figure 4(b) shows SEM images of ZnO/CdS/BC (10%) nanoheterostructure, there are many nanoparticles with the sizes of several nanometers growing on the surfaces of the hybrid fiber, and the particle has a spherical shape. The surfaces become coarse compared with those of ZnO nanorods. Figure 4(c) shows SEM images of ZnO/CdS/BC (20%) nanoheterostructure. It clearly indicates that there are a large number of CdS nanoparticles growing on the surfaces and the surrounding of the hybrid fiber. The SEM of the ZnO/CdS/BC hybrid nanofiber (50 wt%) is shown in Figure 4(d). It is found that the whole hybrid fiber was coated by CdS nanoparticles. Therefore, the formation of hybrid ZnO/CdS/BC fibers was established.

**3.3. Thermogravimetric Analysis (TGA).** Thermal stability of the polymer films was examined at the temperature range of 50–800°C with a heat in grate of 10°C/min, under nitrogen flushed at 200 mL/min using Boyuan DTU-2C thermogravimetric analyzer. As the temperature increased, a graph of weight loss (%) versus temperature was plotted. Bacterial cellulose and ZnO/CdS/BC hybrid fiber (50%) were subjected

to TGA to determine the thermal stability and decomposition characteristics.

Figure 5 shows TGA curves of bacterial cellulose and ZnO/CdS/BC hybrid fiber (50%). The TGA curve of bacterial cellulose shows one main weight loss stage ranging from 280°C to 380°C followed by the final decomposition of the polymer, which can be attributed to the decomposition of main chain of the polymers. At higher heating temperatures, the BC continues to decompose until about 99.8% was lost at temperatures above 600°C. However, only 22% weight was lost when the ZnO/CdS/BC hybrid fibers (50%) were decomposed at 600°C. TGA curves scan indicates that ZnO/CdS/BC hybrid fiber has better thermal properties than BC because ZnO/CdS/BC hybrid fiber does not completely lose weight at the temperature range. It can also indicate there is an interaction between BC and ZnO/CdS nanorod. It was evident that high load of ZnO/CdS/BC ternary hybrid fiber can be achieved in coprecipitation method, which agrees with the results from the latter X-ray photoelectron spectroscopy (XPS).

**3.4. X-Ray Photoelectron Spectroscopy (XPS).** High resolution XPS and wide XPS spectra are conducted to investigate the composition and chemical states of samples. Figure 6 shows the survey spectrum of the ZnO/CdS/BC hybrid fiber (50%). The Zn, O, Cd, C, and S peaks can be clearly observed in the survey spectrum. Carbon might come from the original

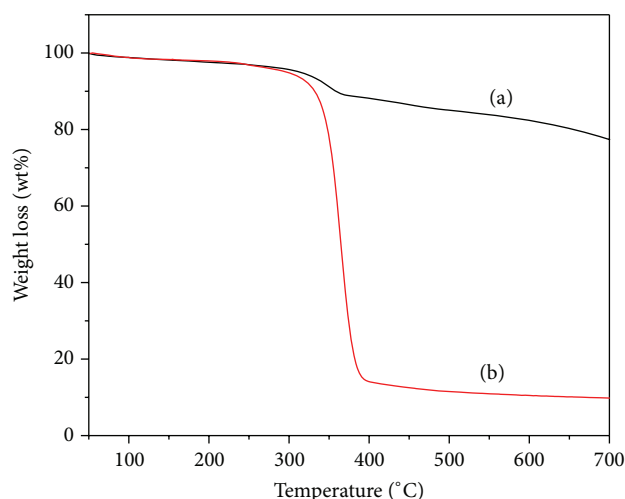


FIGURE 5: TG spectra of (a) ZnO/CdS/BC hybrid fiber (50%) and (b) bacterial cellulose.

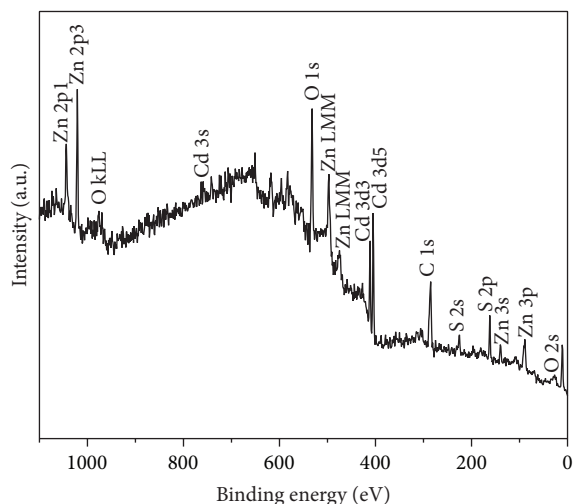


FIGURE 6: XPS of ZnO/CdS/BC hybrid fiber (50%).

source such as bacterial cellulose. Cadmium, zinc, sulfur, and oxygen are expected from the chemical composition of CdS and ZnO.

The narrow spectrum of Cd (a), O (b), S (c), and Zn (d) elements in ZnO/CdS/BC hybrid fiber (50%) is given in Figure 7. Figure 7(a) shows the multiplex spectrum of cadmium peaks. The peaks at binding energies of 411.9 eV and 404.7 eV can be assigned to Cd 3d<sub>3/2</sub> and Cd 3d<sub>5/2</sub> of Cd-S bond, respectively [30]. This is consistent with the binding energies reported in the literature [31, 32]. Figure 7(b) shows the multiplex spectrum of oxygen peaks. The peaks at binding energies of 539 eV can be assigned to O 1s [33]. In addition, Figure 7(c) shows the multiplex spectrum of sulfur peaks. The peaks at binding energies of 161.2 eV can be assigned to S 2p [34]. Figure 7(d) shows the multiplex spectrum of zinc peaks. The peaks at binding energies of 1021.7 eV can be assigned to Zn 2p<sub>3/2</sub> of the Zn-O bond [35]. Moreover, by calculating determination of the peak area of XPS curve, we can see that

the atom ratio of Cd/Zn is about 1, which is close to that of the theoretical standard.

As a result, XPS analysis reveals that a large number of ZnO/CdS nanorods are wrapped on the surface of BC fibers, successfully. It implies that the ternary hybrid fiber can be prepared with coprecipitation method under the low-temperature condition.

**3.5. UV-Vis Absorption Spectroscopy (UV-Vis).** The strong absorption edge of pure ZnO nanorods occurs at the wavelength of 387 nm and their band-gaps can be estimated to 3.21 eV. Compared to the pure ZnO sample, the high absorption edge of pure CdS nanorods occurs at the wavelength of 551 nm and their band-gaps can be estimated to 2.25 eV. Although CdS has a stronger absorption than ZnO in visible light region, the easy occurrence of photochemical corrosion limited its application ranges and lifespan. Therefore, the optimized combined treatment is more effective in preventing photochemical corrosion from CdS and extending the range of spectral response from ZnO. Meanwhile, the efficiency of electron cavity separated is increased and the activity of catalysts is improved.

Figure 8 shows the UV-Vis spectra of the ZnO/CdS/BC hybrid nanofiber (0, 10, 20, and 50 wt%, resp.) under 120°C condition. It is interesting to note that, by increasing the percentage of CdS from 0 to 50%, the absorption is much higher, which can be ascribed to the larger amount of deposited CdS. Compared to the pure ZnO sample, the red shift of ZnO/CdS/BC hybrid nanofiber is becoming more and more obvious. The results indicate that enhancement of the absorption in the visible spectral range could improve the activity of catalysts obviously.

**3.6. Photocatalytic Activity Measurements.** To evaluate the photocatalytic activity of the samples, the photodegradation of the methyl orange was investigated under the simulated sunlight from a 500 W Xe lamp. In the experiment, 20 mg of photocatalyst was suspended in 40 mL of a 20 mg/L aqueous solution of methyl orange. Prior to irradiation, the suspensions were stirred in the dark for 30 min to achieve an adsorption/desorption equilibrium. And then the suspensions were added to photocatalytic reactor. We took a sample in 30 min. The sample was first naturally precipitated and the absorbance for the supernatant was determined.

The photodegradation curves of the samples under UV irradiation are given in Figure 9. A blank test (methyl orange without any catalyst) under irradiation exhibited little decrease in the concentration of methyl orange and its degradation percentage of methyl orange reaches only 12% at 90 min in Figure 9(a). ZnO/BC hybrid fibers as a photocatalyst, by contract, its degradation percentage of methyl orange reached 58% at 90 min in Figure 9(b). For ZnO/CdS, its degradation percentage of methyl orange reaches 90% at 90 min in Figure 9(c). However, for ZnO/CdS/BC nanohybrid fibers (10%) as a photocatalyst, the photodegradation of methyl orange reached nearly 100% after 90 min of the light irradiation in Figure 9(d). It is found that ZnO/CdS/BC

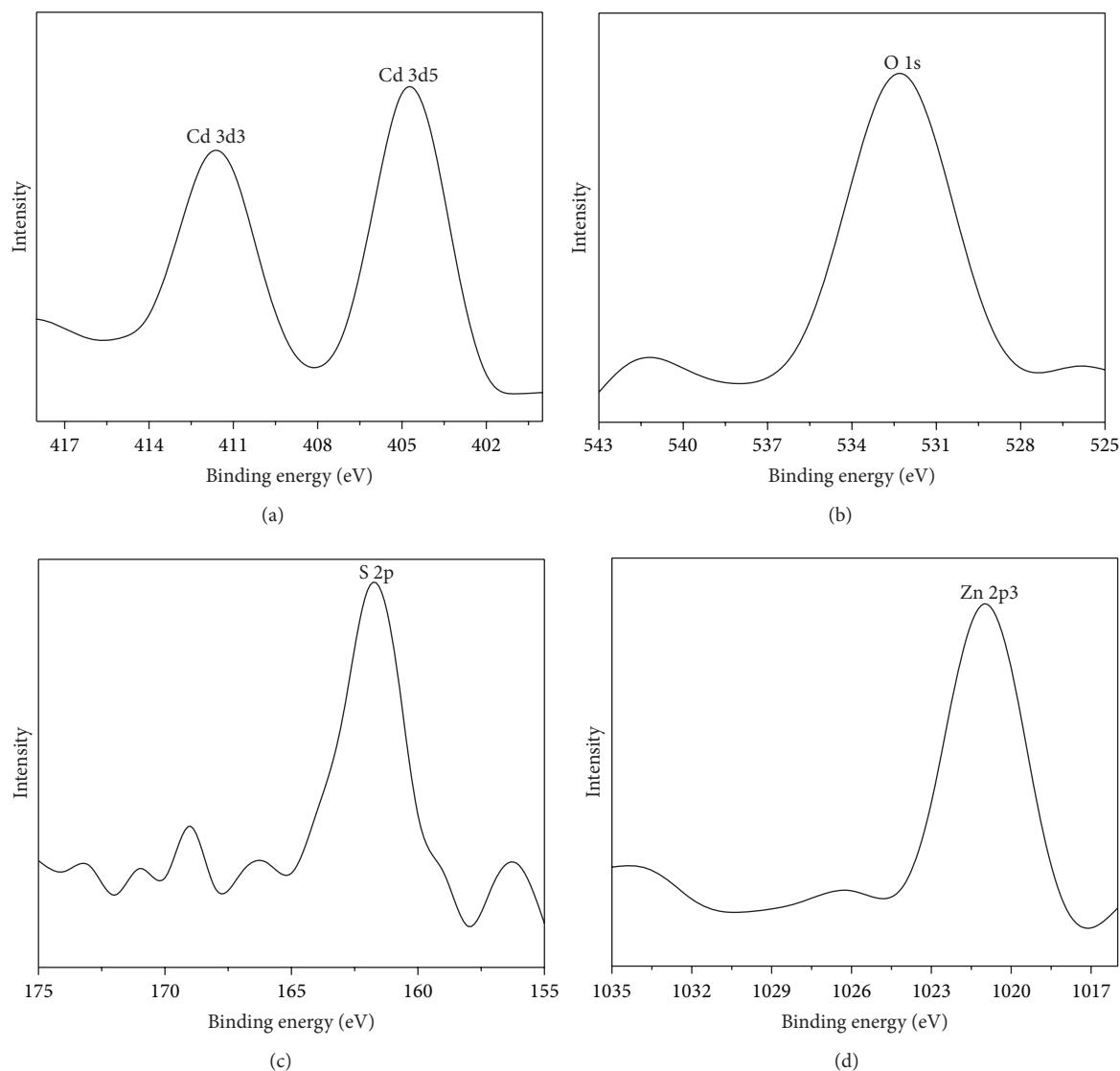


FIGURE 7: Narrow spectrum of (a) Cd, (b) O, (c) S, and (d) Zn, elements in ZnO/CdS/BC hybrid fiber (50%).

nanohybrid fibers (10%) show the best photocatalytic efficiency among the samples, which was mainly attributed to the extended photoresponding range toward visible light. Meanwhile, the BC has good fixation effects on ZnO/CdS nanoheterostructure; it provides greater specific surface area as well as more uniform morphology and helps reduce agglomeration.

#### 4. Conclusions

In summary, an environment-friendly biomaterial bacterial cellulose (BC) was introduced to substitute general organic polymers to assist the preparation of ZnO/CdS/BC ternary hybrid fiber through coprecipitation method under the low-temperature condition. The XRD, XPS, and SEM results showed that high load of ZnO/CdS/BC ternary hybrid fiber could be produced. TGA curves scan revealed that

ZnO/CdS/BC hybrid fiber had better thermal properties. The UV-Vis spectra of the ZnO/CdS/BC hybrid nanofiber (0, 10, 20, and 50 wt%, resp.) under 120°C condition indicated that photocatalytic activities of ZnO/CdS/BC were influenced by the added amount of CdS. It was noted that, by increasing the percentage of CdS from 0 to 50%, the absorption was more higher. Meanwhile, ZnO/CdS/BC nanohybrid fibers showed the best photocatalytic efficiency among the samples. In brief, the application of our ZnO/CdS/BC hybrid in photocatalysis would be promising because of its excellent photocatalytic performance and simple synthetic route.

#### Conflict of Interests

The authors declare that there is no conflict of interests regarding the publication of this paper.

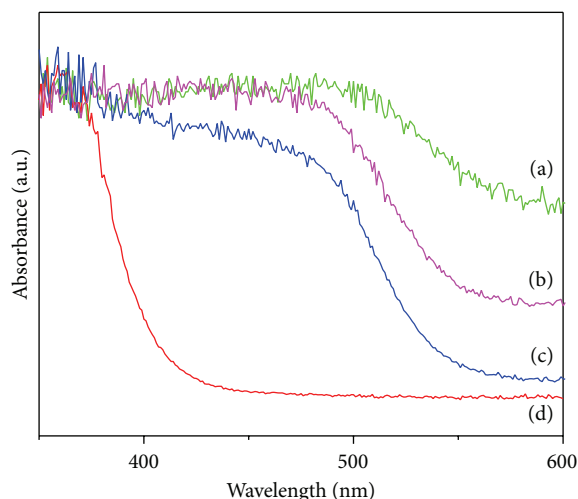


FIGURE 8: UV-Vis absorption spectrum of samples prepared at 120°C with CdS contents at 0, 10%, 20%, and 50%.

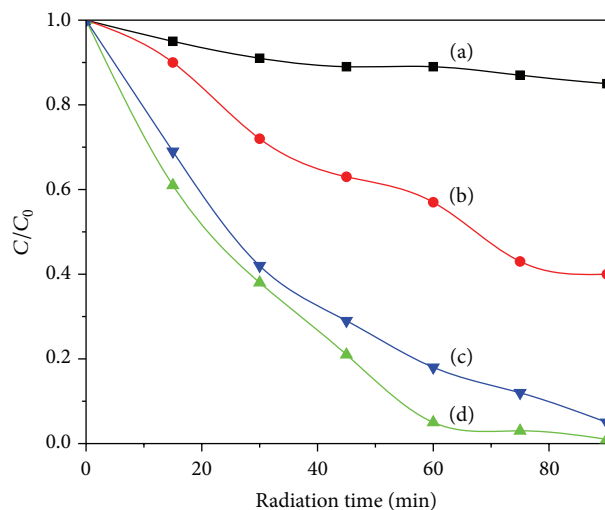


FIGURE 9: Degradation curve of methyl orange: (a) self-degradation of methyl orange, (b) ZnO/BC hybrid fibers, (c) ZnO/CdS, and (d) ZnO/CdS/BC hybrid fibers (10%).

## Acknowledgments

The authors acknowledged the financial support from the National Natural Science Foundation of China (no. 21206076) and the Natural Science Foundation of Jiangsu Province (no. BK 2012401).

## References

- [1] F. Lu, W. P. Cai, and Y. Zhang, "ZnO hierarchical micro/nano-architectures: solvothermal synthesis and structurally enhanced photocatalytic performance," *Advanced Functional Materials*, vol. 18, no. 7, pp. 1047–1056, 2008.
- [2] Y. Guo, H. S. Wang, C. I. He, L. J. Qiu, and X. B. Cao, "Uniform carbon-coated ZnO nanorods: microwave-assisted preparation, cytotoxicity, and photocatalytic activity," *Langmuir*, vol. 25, no. 8, pp. 4678–4684, 2009.
- [3] R. Kitture, S. J. Koppikar, R. Kaul-Ghanekar, and S. N. Kale, "Catalyst efficiency, photostability and reusability study of ZnO nanoparticles in visible light for dye degradation," *Journal of Physics and Chemistry of Solids*, vol. 72, no. 1, pp. 60–66, 2011.
- [4] X. Fang, Y. Bando, U. K. Gautam et al., "ZnO and ZnS nanostructures: ultraviolet-light emitters, lasers, and sensors," *Critical Reviews in Solid State and Materials Sciences*, vol. 34, no. 3-4, pp. 190–223, 2009.
- [5] X. S. Fang and L. D. Zhang, "Controlled growth of one-dimensional oxide nanomaterials," *Journal of Materials Science and Technology*, vol. 22, no. 1, pp. 1–18, 2006.
- [6] H. Herrmann, S. T. Martin, and M. R. Hoffmann, "Time-Resolved Radio Frequency Conductivity (TRRFC) studies of charge-carrier dynamics in aqueous semiconductor suspensions," *Journal of Physical chemistry*, vol. 99, no. 45, pp. 16641–16645, 1995.
- [7] A. L. Linsebigler, G. Q. Lu, and J. T. Yates Jr., "Photocatalysis on TiO<sub>2</sub> surfaces: principles, mechanisms, and selected results," *Chemical Reviews*, vol. 95, no. 3, pp. 735–758, 1995.
- [8] Q. Wang, G. Chen, C. Zhou, R. Jin, and L. Wang, "Sacrificial template method for the synthesis of CdS nanosponges and their photocatalytic properties," *Journal of Alloys and Compounds*, vol. 503, no. 2, pp. 485–489, 2010.
- [9] Y. Tak, S. J. Hong, J. S. Lee, and K. Yong, "Fabrication of ZnO/CdS core/shell nanowire arrays for efficient solar energy conversion," *Journal of Materials Chemistry*, vol. 19, no. 33, pp. 5945–5951, 2009.
- [10] G. Dukovic, M. G. Merkle, J. H. Nelson, S. M. Hughes, and A. P. Alivisatos, "Photodeposition of Pt on colloidal CdS and CdSe/CdS semiconductor nanostructures," *Advanced Materials*, vol. 20, no. 22, pp. 4306–4311, 2008.
- [11] C.-S. Yang, D. D. Awschalom, and G. D. Stucky, "Kinetic-dependent crystal growth of size-tunable CdS nanoparticles," *Chemistry of Materials*, vol. 13, no. 2, pp. 594–598, 2001.
- [12] M. Sharma and P. Jeevanandam, "Synthesis, characterization and studies on optical properties of hierarchical ZnO-CdS nanocomposites," *Materials Research Bulletin*, vol. 47, no. 7, pp. 1755–1761, 2012.
- [13] K. Yuan, L. Chen, F. Li, and Y. Chen, "Nanostructured hybrid ZnO@CdS nanowalls grown in situ for inverted polymer solar cells," *Journal of Materials Chemistry C*, vol. 2, no. 6, pp. 1018–1027, 2014.
- [14] M. Zirak, O. Akhavan, O. Moradlou, Y. T. Nien, and A. Z. Moshfegh, "Vertically aligned ZnO@CdS nanorod heterostructures for visible light photoinactivation of bacteria," *Journal of Alloys and Compounds*, vol. 590, pp. 507–513, 2014.
- [15] M. Misra, P. Kapur, C. Ghanshyam, and M. L. Singla, "ZnO@CdS core-shell thin film: fabrication and enhancement of exciton life time by CdS nanoparticle," *Journal of Materials Science: Materials in Electronics*, vol. 24, no. 10, pp. 3800–3804, 2013.
- [16] M. Zirak, O. Moradlou, M. R. Bayati, Y. T. Nien, and A. Z. Moshfegh, "On the growth and photocatalytic activity of the vertically aligned ZnO nanorods grafted by CdS shells," *Applied Surface Science*, vol. 273, pp. 391–398, 2013.
- [17] X. Wang, G. Liu, G. Q. Lu, and H.-M. Cheng, "Stable photocatalytic hydrogen evolution from water over ZnO-CdS core-shell nanorods," *International Journal of Hydrogen Energy*, vol. 35, no. 15, pp. 8199–8205, 2010.
- [18] R. Wu, C. S. Xie, H. Xia, J. Hu, and A. Wang, "The thermal physical formation of ZnO nanoparticles and their morphology," *Journal of Crystal Growth*, vol. 217, no. 3, pp. 274–280, 2000.



- [19] H. Park, W. Choi, and M. R. Hoffmann, "Effects of the preparation method of the ternary CdS/TiO<sub>2</sub>/Pt hybrid photocatalysts on visible light-induced hydrogen production," *Journal of Materials Chemistry*, vol. 18, no. 20, pp. 2379–2385, 2008.
- [20] J. Cao, J.-Z. Sun, J. Hong, H.-Y. Li, H.-Z. Chen, and M. Wang, "Carbon nanotube/CdS Core-shell nanowires prepared by a simple room-temperature chemical reduction method," *Advanced Materials*, vol. 16, no. 1, pp. 84–87, 2004.
- [21] J. Juntaro, M. Pommet, G. Kalinka, A. Mantalaris, M. S. P. Shaffer, and A. Bismarck, "Creating hierarchical structures in renewable composites by attaching bacterial cellulose onto sisal fibers," *Advanced Materials*, vol. 20, no. 16, pp. 3122–3126, 2008.
- [22] J. Z. Yang, J. Yu, J. Fan, D. Sun, W. Tang, and X. Yang, "Biotemplated preparation of CdS nanoparticles/bacterial cellulose hybrid nanofibers for photocatalysis application," *Journal of Hazardous Materials*, vol. 189, no. 1-2, pp. 377–383, 2011.
- [23] C. Li, T. Ahmed, M. Ma, T. Edvinsson, and J. Zhu, "A facile approach to ZnO/CdS nanoarrays and their photocatalytic and photoelectrochemical properties," *Applied Catalysis B: Environmental*, vol. 138-139, pp. 175–183, 2013.
- [24] L. Irimpan, D. Ambika, V. Kumar, V. P. N. Nampoori, and P. Radhakrishnan, "Effect of annealing on the spectral and nonlinear optical characteristics of thin films of nano-ZnO," *Journal of Applied Physics*, vol. 104, no. 3, Article ID 033118, 2008.
- [25] T. K. Jana, A. Pal, and K. Chatterjee, "Self assembled flower like CdS-ZnO nanocomposite and its photo catalytic activity," *Journal of Alloys and Compounds*, vol. 583, pp. 510–515, 2014.
- [26] J. Nayak, "Enhanced light to electricity conversion efficiency of CdS-ZnO composite nanorod based electrochemical solar cell," *Materials Chemistry and Physics*, vol. 133, no. 1, pp. 523–527, 2012.
- [27] G. Murugadoss, "ZnO/CdS nanocomposites: synthesis, structure and morphology," *Particuology*, vol. 10, no. 6, pp. 722–728, 2012.
- [28] X. Hou and L. Wang, "Sonochemical synthesis and charge transfer property of core/shell ZnO/CdS nanohybrids," *Materials Letters*, vol. 122, pp. 29–32, 2014.
- [29] D. Sun, J. Yang, and X. Wang, "Bacterial cellulose/TiO<sub>2</sub> hybrid nanofibers prepared by the surface hydrolysis method with molecular precision," *Nanoscale*, vol. 2, no. 2, pp. 287–292, 2010.
- [30] W. F. Liu, C. Jia, C. G. Jin, L. Z. Yao, W. L. Cai, and X. G. Li, "Growth mechanism and photoluminescence of CdS nanobelts on Si substrate," *Journal of Crystal Growth*, vol. 269, no. 2–4, pp. 304–309, 2004.
- [31] T. Y. Zhai, X. S. Fang, Y. Bando et al., "Morphology-dependent stimulated emission and field emission of ordered CdS nanostructure arrays," *ACS Nano*, vol. 3, no. 4, pp. 949–959, 2009.
- [32] W.-S. Chae, S.-W. Lee, M.-J. An et al., "Nanostructures and optical properties of mesoporous composite nanofibers containing CdS quantum dots," *Chemistry of Materials*, vol. 17, no. 23, pp. 5651–5657, 2005.
- [33] S. M. Hosseini, I. A. Sarsari, P. Kameli, and H. Salamati, "Effect of Ag doping on structural, optical, and photocatalytic properties of ZnO nanoparticles," *Journal of Alloys and Compounds*, vol. 640, pp. 408–415, 2015.
- [34] D.-P. Kim, C.-I. Kim, and K.-H. Kwon, "Etching properties of ZnS thin films in Cl<sub>2</sub>/CF<sub>4</sub>/Ar plasma," *Thin Solid Films*, vol. 459, no. 1-2, pp. 131–136, 2004.
- [35] Y. Jin, Q. Cui, K. Wang, J. Hao, Q. Wang, and J. Zhang, "Investigation of photoluminescence in undoped and Ag-doped ZnO flowerlike nanocrystals," *Journal of Applied Physics*, vol. 109, no. 5, Article ID 053521, 2011.

## Research Article

# Comparing and Optimizing Nitrate Adsorption from Aqueous Solution Using Fe/Pt Bimetallic Nanoparticles and Anion Exchange Resins

Muhammad Daud, Zahiruddin Khan, Aisha Ashgar, M. Ihsan Danish, and Ishtiaq A. Qazi

*Institute of Environmental Sciences and Engineering, School of Civil and Environmental Engineering,  
National University of Sciences and Technology, Islamabad 44000, Pakistan*

Correspondence should be addressed to Aisha Ashgar; [aisha.iiui@yahoo.com](mailto:aisha.iiui@yahoo.com)

Received 23 February 2015; Revised 3 July 2015; Accepted 7 July 2015

Academic Editor: Jiazhi Yang

Copyright © 2015 Muhammad Daud et al. This is an open access article distributed under the Creative Commons Attribution License, which permits unrestricted use, distribution, and reproduction in any medium, provided the original work is properly cited.

This research work was carried out for the removal of nitrate from raw water for a drinking water supply. Nitrate is a widespread ground water contaminant. Methodology employed in this study included adsorption on metal based nanoparticles and ion exchange using anionic resins. Fe/Pt bimetallic nanoparticles were prepared in the laboratory, by the reduction of their respective salts using sodium borohydride. Scanning electron microscope, X-ray diffraction, energy dispersive spectrometry, and X-ray florescence techniques were utilized for characterization of bimetallic Fe/Pt nanoparticles. Optimum dose, pH, temperature, and contact time were determined for  $\text{NO}_3^-$  removal through batch tests, both for metal based nanoparticles and anionic exchange resin. Adsorption data fitted well the Langmuir isotherm and conformed to the pseudofirst-order kinetic model. Results indicated 97% reduction in nitrate by 0.25 mg/L of Fe/Pt nanoparticles at pH 7 and 83% reduction in nitrate was observed using 0.50 mg/L anionic exchange resins at pH 4 and contact time of one hour. Overall, Fe/Pt bimetallic nanoparticles demonstrated greater  $\text{NO}_3^-$  removal efficiency due to the small particle size, extremely large surface area ( $627 \text{ m}^2/\text{g}$ ), and high adsorption capacity.

## 1. Introduction

Nitrate is the most widely available contaminant in ground and surface waters [1]. Excess of nitrate in drinking water results from anthropogenic sources, for example, overfertilization in agriculture, cattle shed discharge, untreated sewage, leakage from septic systems, infiltration of landfill leachate, and industrial waste water [2–5]. Out of these, synthetic fertilizers are the major contributors of nitrate pollution [6]. Nitrate concentration above the maximum permissible limit in drinking water is injurious to human health. Nitrate exposure can also lead to several health issues such as blue baby syndrome, increased infant mortality, birth defects, abdominal pain, diarrhea, vomiting, diabetes, hypertension, respiratory tract infections, and changes in the immune system [7–11]. To limit the risk to human health from nitrate in drinking water, the Maximum Contaminant Level (MCL) is set to be  $10 \text{ mg NO}_3^-/\text{L}$  ( $45 \text{ mg NO}_3^-/\text{L}$ ) by USEPA,

while the World Health Organization (WHO) and the European Community have set the MCL at  $11.3 \text{ mg NO}_3^-/\text{L}$  ( $50 \text{ mg NO}_3^-/\text{L}$ ) [12, 13]. Numerous technologies are available for removal of nitrate from water. These include reverse osmosis, electrodialysis, biological denitrification, and ion exchange methods. In case of reverse osmosis (RO) water passes through a semipermeable membrane, and nitrate and other ions are rejected because their size is greater than the membrane pore size [14, 15]. Biological denitrification is widely practiced for the treatment of municipal and industrial wastewater but is less commonly used in drinking water applications [16]. Ion exchange is a process in which the target ion gets exchanged with a loosely adsorbed ion on a resin. Ion exchange is also like a reversible chemical process in which ions from an insoluble permanent solid medium (the ion exchanger is usually a resin) are exchanged for ions in a solution [17]. This process is widely adopted for nitrate removal because of its simplicity, effectiveness, and

relatively low cost [15–17]. Most of the on-going research has focused on nanosized zerovalent iron (NZVI) particles which typically have their size within the range of 1–100 nm [18, 19]. The nanosized iron have larger surface area, about ten to hundreds times larger than microscopic iron powder, which results in more exposure of particles surface leading to enhanced adsorption efficiency [20].

NZVI supplemented with the secondary metal is a new technique for nitrate removal, which enhances the catalytic reactivity through hydrogenation [21, 22]. Secondary metal also enhances reaction rate [23]. In order to improve the nitrate removal, various bimetallic nanoparticles were tested in batch studies and the most efficient combination of metals, that is, (Fe/Pt) nanoparticles, was compared with commonly used, strong base anionic exchange resins (Amberlite IRA402 Cl). Langmuir and Freundlich isotherm models were used to study favorability of adsorption. To study kinetics of the chemical reactions pseudosecond-order kinetics model was applied.

## 2. Materials and Methods

**2.1. Materials.** Chemicals used in this research work included  $\text{NaBH}_4$  (Sigma-Aldrich),  $\text{FeCl}_3 \cdot 6\text{H}_2\text{O}$  (Merck),  $\text{FeSO}_4 \cdot 7\text{H}_2\text{O}$  (Merck),  $\text{PtCl}_4$  (Merck), PEG-4000 (Merck), and  $\text{CuSO}_4 \cdot 6\text{H}_2\text{O}$  (Merck). For solution preparation, known quantities of the compounds were dissolved in deionized water ( $\text{EC} < 0.7 \mu\text{S}/\text{cm}$ , Labconco Waterpro PS).  $\text{KNO}_3$  was used for the nitrate solutions. For ion exchange experiments, strong base anion exchange resins (Amberlite IRA402 Cl) were purchased from Sigma-Aldrich. 0.1 M. Hydrochloric acid (HCl) and sodium hydroxide (NaOH) were used to adjust pH of the nitrate solutions. 10% NaCl was used for regeneration of anionic exchange resins.

### 2.2. Methodology

**2.2.1. Synthesis of Pt/Fe Bimetallic Nanoparticles.** Fe/Pt bimetallic nanoparticles were synthesized in the laboratory in a Vacuum Glove Box (model: CV-1000 SAMPLATEC Corp., Japan) in an inert atmosphere. To synthesize Fe/Pt nanoparticles,  $\text{NaBH}_4$  (0.2 M, 99% Aldrich) solution was prepared in DI water/ethanol in 4:1 (v/v) and added slowly at the rate of 2 mL/min to  $\text{FeCl}_3 \cdot 6\text{H}_2\text{O}$  (0.05 M, 99% Merck) and  $\text{PtCl}_4$  (0.05 M, 99% Merck) aqueous solution at 400 rpm in nitrogen atmosphere in glove box. The solution was filtered using  $0.45 \mu\text{m}$  membrane filter in inert atmosphere to avoid contact of nanoparticles with air, prior to titration against  $\text{HNO}_3$ . The resulting nanoparticles were washed thrice with distilled water and ethanol and stored in the dark.

**2.2.2. Characterization of Fe/Pt Bimetallic Nanoparticles.** Bimetallic nanoparticles were analyzed through X-ray diffraction (XRD, JEOL JDX-II, Japan). X-ray fluorescence analysis was performed using XRF-JEOL (Model JSX-3202M, Japan). The scanning electron microscope (JSM-6460, JEOL Ltd., Japan) attached with energy dispersive spectrometer (EDS, JSM-6460, JEOL Ltd., Japan) was used to find out surface morphology and composition of nanoparticles.

The porous texture characterization of the samples was recorded by  $\text{N}_2$  adsorption data at  $-196^\circ\text{C}$  (Autosorb-6B apparatus from Quantachrome [20]) the specific BET surface area ( $S_{\text{BET}}$ ) was determined by applying using Brunauer-Emmett-Teller (BET) equation.

### 2.2.3. Batch Experiments Using Fe/Pt Bimetallic Nanoparticles.

Batch experiments were carried out in 250 mL glass beaker covered with aluminum foil. All of the apparatus was covered, during experimentation, to restrict photocatalytic activity of nanoparticles and, moreover, to study adsorption efficiency of nanoparticles only. All experimental conditions optimization experiments were performed with 100 mg/L nitrate solutions. For dosage optimization, test solutions containing different concentrations of Fe/Pt bimetallic nanoparticles (0.1, 0.25, 0.50, 0.75, and 1 g) were placed at an orbital shaker at 200 rpm for one hour at room temperature. After dosage optimization, test solution with optimized dosage was tested at 200 rpm for one hour, at three different pH levels (4, 7, and 10). Subsequent to dose and pH optimization, test solutions with optimized dosage were tested for different contact times (5, 10, 15, 20, 30, 45, 60, 90, and 120 min), with optimized dosage and optimized pH. Finally, effect of temperature on removal efficiencies was studied at 15, 25, and  $40^\circ\text{C}$ , with all other optimized conditions.

### 2.2.4. Batch Experiments Using Anionic Exchange Resins.

Slurry based anionic exchange experiments were performed at different temperatures (i.e., 25, 45, and  $60^\circ\text{C}$ ), in 250 mL beaker containing nitrate solution added with varying quantities of anionic resin. Mixing was maintained by orbital shaker. After providing specific mixing time, the sample was filtered and tested. Parameters such as pH (4, 7, and 10), effect of initial nitrate concentrations (10, 25, 50, 100, 200, 300, 400, and 500 mg/L) on removal efficiencies, and reaction times (5, 10, 15, 30, 45, 60, 90, and 120 min) were investigated using spectrophotometer.

**2.2.5. Adsorption and Kinetic Isotherm Experiments.** In order to evaluate the surface properties and nanoparticles adsorption capacity, the experimental data were applied to the Langmuir equation. Isotherm experiments were performed with different initial nitrate concentration solution (10–500 mg/L), and the contact time of 1 hour, pH values of  $4 \pm 0.05$ , and temperature of  $25^\circ\text{C}$  were chosen as the experimental conditions to determine the adsorption isotherm of nitrate ions. For kinetic studies similar reaction conditions were used and reaction time was extended, till 2.5 hours, and samples were taken from time to time for final nitrate concentration analysis.

## 3. Results and Discussion

**3.1. Characterization of Fe/Pt Bimetallic Nanoparticles.** Characterization of Fe/Pt bimetallic nanoparticles is represented in Figure 1. The Pt is loaded at the surface of Fe nanoparticles, giving it a kind of bimetallic alloy nature. SEM images confirmed the presence of uniform spheroid, macroporous, sponge-like structure of high roughness and complexity. Such

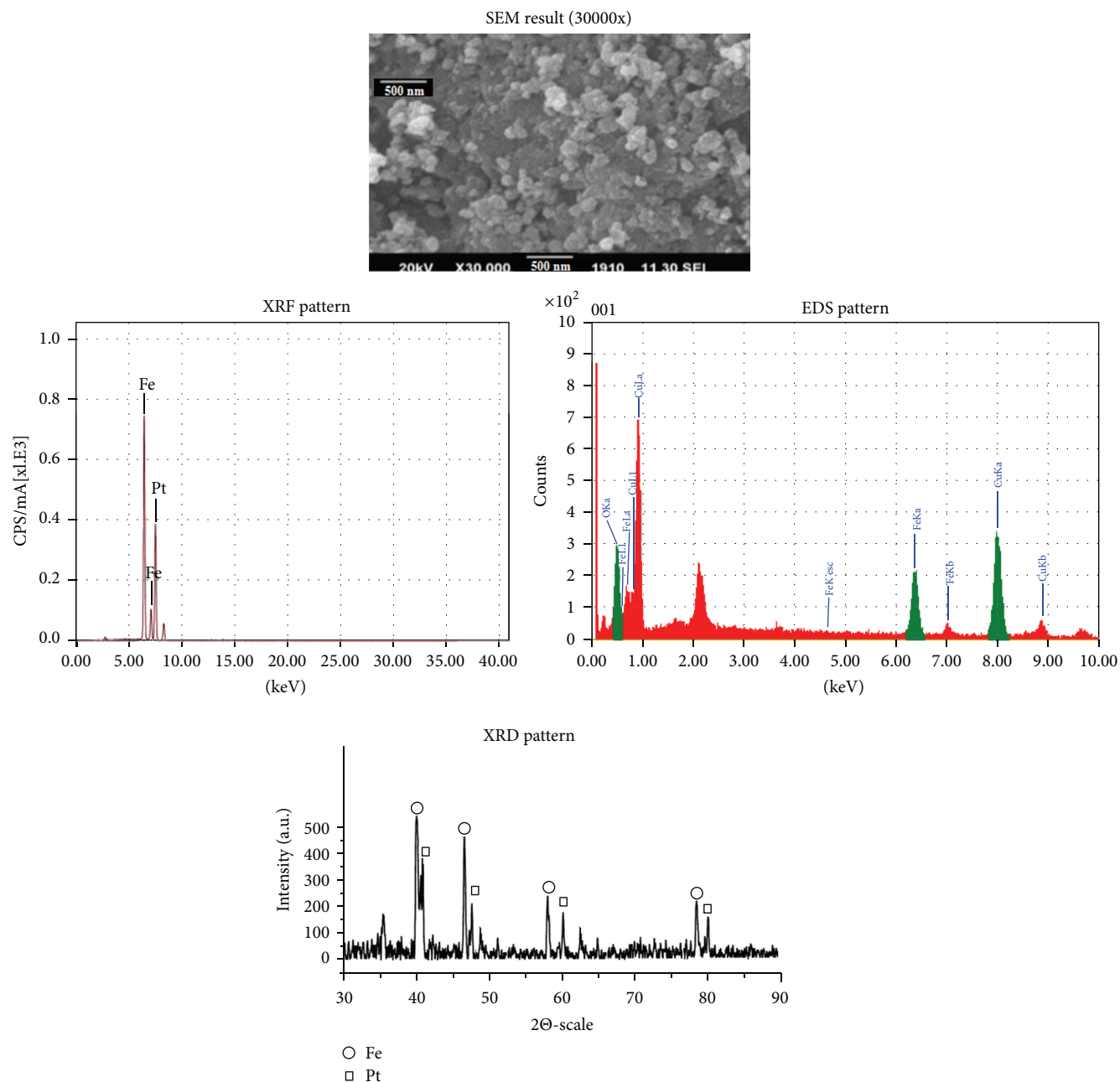


FIGURE 1: Characterization of Fe/Pt nanoparticles.

structure indicated the high surface area ( $627 \text{ m}^2/\text{g}$ ) which has been proven to be efficient for photocatalytic degradation purposes. XRF analysis confirmed that nanoparticles were composed of Fe and Pt metals in equimolar ratio. All of the samples show the superlattice reflections (001) and (110) as well as some splitting of the (200)/(002) peak which signifies a tetragonality, as shown in Figure 1. EDS pattern revealed that the Fe/Pt nanoparticles were composed of almost 50% of each metal. X-ray diffraction was used to investigate the crystal phase composition bimetallic nanoparticles. XRD patterns showed that the nanoparticles contained pure anatase phase with the average crystallite sizes of 19 to 42 nm.

### 3.2. Experiment Conditions Optimization

**3.2.1. Effect of Adsorbent Dose.** To study the removal efficiencies of adsorbent doses, 200 mg/L of the initial nitrate solution was used. Dosages for both anion exchange resin and Fe/Pt bimetallic nanoparticles were varied among 100 mg/L to 1000 mg/L, at pH 7 within the contact time of 60 min for both adsorbents. It is clear from Figure 2 that  $\text{NO}_3^-$  removal is directly proportional to the adsorbent dose till 500 mg/L. Doses higher than 500 mg/L for resins and 250 mg/L for nanoparticles did not show significant  $\text{NO}_3^-$ , so it would not be economical. The higher removal of nitrate was because of

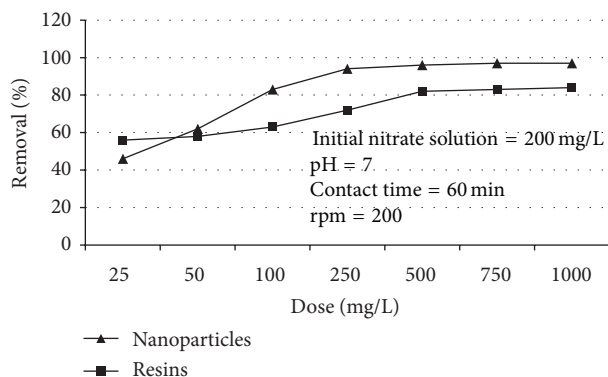


FIGURE 2: Effect of dose on nitrate removal by resins and Fe/Pt bimetallic nanoparticles.

greater surface area of Fe/Pt nanoparticles requiring smaller dose as compared to anionic exchange resins.

**3.2.2. Effect of pH.** The effect of pH on nitrate removal using Fe/Pt bimetallic nanoparticles and anionic exchange resins was studied at three different pH values (4, 7, and 10) with the optimized dosage (0.50 mg/L resins, 0.25 mg/L nanoparticles) against 200 mg/L nitrate solution, within the contact time of one hour. Nitrate removal by Fe/Pt bimetallic nanoparticles and anionic exchange resins as a function of pH is shown in Figure 3. Results showed that, for anionic resin, nitrate was removed at all pH levels to a varying degree, at a contact time of 60 minutes. A maximum of 82.5% removal was achieved, using resin at 4 pH. Nitrate reduction efficiency by resins decreased notably with raising pH of the solution. The removal efficiency of nanoparticles, after contact time of 60 min and pH value of 4–10, varied between 92 and 83%. Rate of nitrate removal at pH 7 was distinctively higher than for pH 4 or 10.

**3.2.3. Effect of Contact Time.** Effect of adsorption of nitrate on Fe/Pt nanoparticles and anionic exchange resins as a function of contact time of adsorbents is shown in Figure 4. A pH 7 was maintained for nanoparticles and pH 4 for anionic exchange resins. Optimized dose of each adsorbent was used for initial 200 mg/L nitrate solution. As reflected from the results, with increasing reaction time, the nitrate removal efficiency increased, for both adsorbents.

The distinct slopes in Fe/Pt nanoparticles curve showed that overall adsorption characteristics of nanoparticles changed with contact time over 45 min and continuously yielding slope reflected that extension in contact time would not have any dramatic effect on  $\text{NO}_3$  removal. The ion exchange resin however smoothly exhausted at about 70 min. This also confirmed that minimum contact time of 60 minutes used in this experiment would be logical. For the contact time of 60 min, nitrate removal efficiency was 91% vis-à-vis 83% under all other optimized conditions and the same contact time.

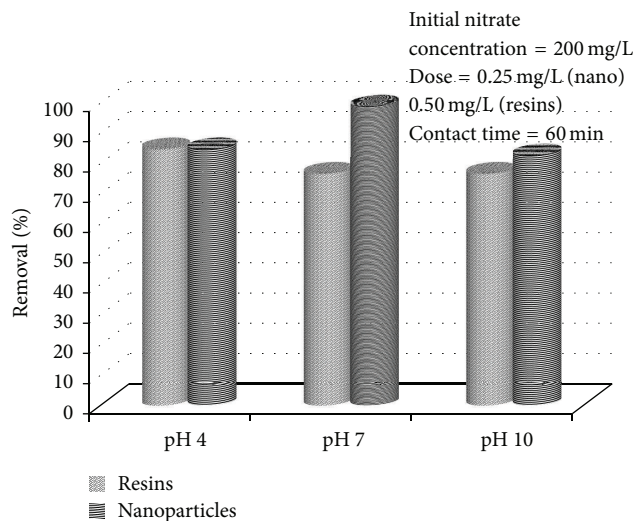


FIGURE 3: Effect of pH on nitrate removal by resins and Fe/Pt bimetallic nanoparticles.

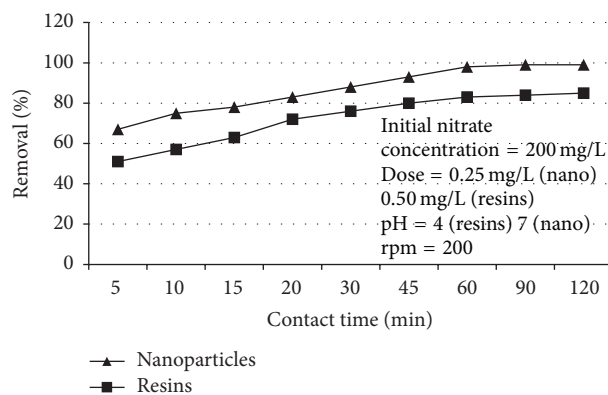


FIGURE 4: Effect of contact time on nitrate removal by resins Fe/Pt bimetallic nanoparticles.

**3.2.4. Effect of Temperature.** The effect of temperature on nitrate was studied using optimized dosage, pH, and contact time, against 200 mg/L nitrate solution at three different temperatures, that is, 15, 25, and 35°C. Figure 5 shows the results. The effect of temperature on nitrate removal via anionic exchange resins indicated that nitrate removal increased, by increasing temperature. For Fe/Pt nanoparticles, during contact time of 60 min and at temperature 25°C, about 87–90% of nitrate was removed. For resin rise in temperature up to 35°C helps improving  $\text{NO}_3$  removal. For Fe/Pt bimetallic nanoparticles, rise in temperature lowers  $\text{NO}_3$  removal efficiency.

**3.2.5. Effect of Initial Nitrate Concentration.** In the batch experimentation using anionic resin, the adsorption efficiency of resins under all other optimized conditions decreased from 83% to 48%, when the initial nitrate concentration increased from 10 to 400 mg/L as shown in Figure 6. For similar changes in initial concentration of nitrate, with



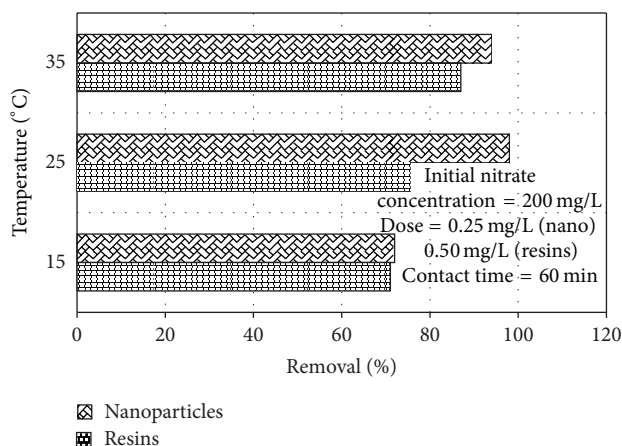


FIGURE 5: Effect of temperature on nitrate removal by resins and Fe/Pt bimetallic nanoparticles.

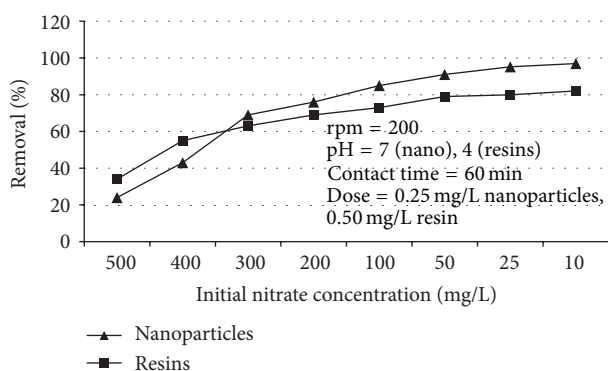


FIGURE 6: Effect of initial nitrate concentration and its removal by resin and Fe/Pt bimetallic nanoparticles.

Fe/Pt nanoparticles and nitrate adsorption efficiency gradually reduced from 98% to 51%.

It seems to be an ion exchange resin support ion exchange phenomenon, till the  $\text{NO}_3^-$  concentration rises beyond its exchange capacity. There is however a smooth reduction in Fe/Pt nanoparticle effectiveness with increase in initial concentration of  $\text{NO}_3^-$ .

### 3.3. Adsorption and Kinetic Isotherms

**3.3.1. Langmuir Isotherm.** Capacity of the adsorbent can be estimated by adsorption studies. In order to evaluate the surface properties and resins adsorbent or exchange capacity the experimental data of varying initial nitrate concentrations was applied to the Langmuir equations. The linear Langmuir adsorption isotherms of nitrate ions are illustrated in Figure 7. The Langmuir parameters,  $q_m$  and  $b$ , are calculated from the slope and intercept of the graphs and are given in Table 1. The linear fitting of models was examined by calculation of correlation factors ( $R^2$ ). The correlation values are also given in Table 1. These values for Langmuir constants are higher in case of Fe/Pt bimetallic nanoparticles indicating that Langmuir isotherm better fits adsorption data

TABLE 1: Langmuir isotherms constants of nitrate ions adsorption by nanoparticles and resins.

Materials	$q_m$ (mg/g)	$b$	$R_L$	$R^2$
Resins	83.55	0.057	0.08	0.984
Fe/Pt nanoparticles	103	0.647	0.01	0.998

of nanoparticles, compared to the resin. Data clearly suggests that the adsorption of nitrates ions is monolayer-type in both cases; moreover, it agrees with the observation that the adsorption from an aqueous solution usually forms a layer on the adsorbent surface. The higher values of Langmuir constant  $b$  shows the enhanced affinity of binding sites and suggests that a chemical interaction between adsorbent and adsorbate occurs much better in case of nanoparticles. The  $R_L$  values (see Table 1) are all found to be within 0 and 1 indicating a highly favorable adsorption of nitrate ions onto ion exchange resins.

The Langmuir model assumes that adsorption occurs in monolayer or that adsorption may only occur at fixed number of localized sites on the surface with all adsorption sites identical and energetically equivalent.

**3.3.2. Kinetic Isotherms.** Adsorption kinetics determines the efficiency of adsorption; therefore, pseudosecond-order kinetic model was applied on the adsorption data. The correlation coefficients values indicate that the experimental data fits the kinetic model as shown in Figure 8.

Results explicitly explain that nitrate adsorption on nanoparticles and resins is a function of time and pH 4. For a 200 ppm initial nitrate concentration and resins dose of 0.5 mg/L, 12% of the total nitrate was removed after the first 5 min; this value promptly increased to about 53% after 20 min. After 120 min, the maximum removal was 97%. Nitrate adsorption on bimetallic nanoparticles is also a function of contact time and dose at pH 7 as removal efficiency increased with the increase of contact time. For a 200 ppm initial nitrate concentration and bimetallic nanoparticles dose of 0.25 mg/L, after the first 5 min, 15.5% of the total nitrate was removed and removal percentage drastically increased to about 68% after 20 min. After 120 min the maximum removal was 83.5%. Parameters for kinetic isotherm for both adsorbents are represented in Table 2, and all values are higher in case of nanoparticles, compared to resins. It is clear from the results that adsorption using nanoparticles gives much better removal efficiency.

## 4. Conclusions

The overall results indicate that Fe/Pt nanoparticles having a large surface area ( $627 \text{ m}^2/\text{g}$ ) are potentially more efficient than the commercially used anionic resins for nitrate removal from water. Literature review demonstrates that, in bimetallic system, Fe is considered reductant for water to generate hydrogen, and the second metal, that is, Pt, which has a high ability to dissociate  $\text{H}_2$  acts as catalyst [24]. For hydrochlorination of halogenated compounds, the coating of

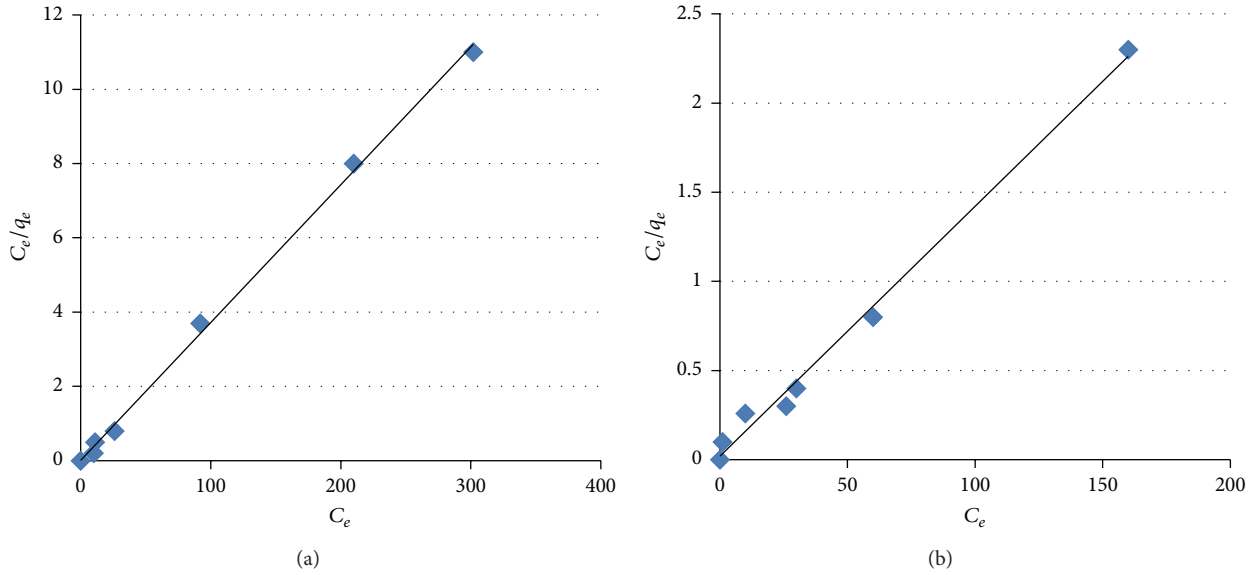


FIGURE 7: Langmuir adsorption model for (a) Fe/Pt bimetallic nanoparticles  $25 \pm 1^\circ\text{C}$  and (b) resins at  $35 \pm 1^\circ\text{C}$ .

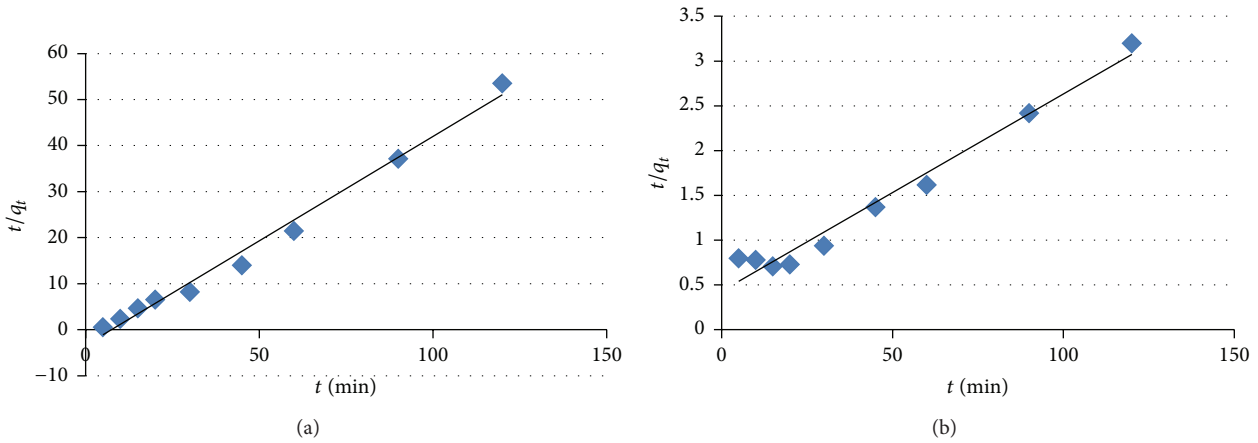


FIGURE 8: Pseudosecond-order kinetics model for (a) Fe/Pt bimetallic nanoparticles and (b) resins at  $25 \pm 1^\circ\text{C}$ .

TABLE 2: Pseudosecond-order kinetic plots for the adsorption of nitrate ions on nanoparticles.

Materials	$q_e$ (mg/g)	$K$ (g/mg min)	$R^2$
Fe/Pt nanoparticles	45.45	0.432	0.973
Resins	22.075	0.146	0.984

secondary metal not only enhances the reactivity but also lowered the accumulation of toxic byproducts. Presence of Pt dramatically increased the reactivity of Fe nanoparticles for nitrate reduction.

During the catalytic reduction process of nitrate, nitrite was tested as intermediate product with the trend of first rising and then decreasing; no nitrite existed in solution at the end of reaction. This indicates that nitrate reduction with Fe/Pt nanoparticles undergoes two steps: firstly, nitrate is adsorbed to nanoparticles surface and afterward is reduced

to nitrite; as a result of strong affinity of particles surface to nitrite, only a little nitrite was detected in the solution during the reaction. Finally adsorbed nitrite reduced to ammonium followed by desorption of ammonium due to the weak affinity between Fe/Pt bimetallic particles surface and ammonium [25].

Adsorption of nitrate was determined to be a pseudofirst-order reaction, with rates influenced by the initial concentration of the nitrate; furthermore, adsorption rate using nanoparticles were maximum at 7 pH and  $25^\circ\text{C}$  with an optimized nanoparticles dose of 0.25 mg/L. While adsorption results generated for both adsorbents fitted well the Langmuir isotherm, all Langmuir constants showed higher values in case of nanoparticles. Using optimized adsorption conditions resins showed maximum 83% removal; however, nanoparticles gave 97% nitrate removal for an initial nitrate solution of 200 mg/L in water. Experiments are currently underway (at IESE, NUST) in attempt to test and to study adsorption



and photocatalytic effect of Pt/Fe bimetallic nanoparticles on other ions present in waste water, through rapid small scale filter column tests.

## Conflict of Interests

The authors declare that there is no conflict of interests regarding the publication of this paper.

## Acknowledgment

The authors gratefully acknowledge financial support from the National University of Science and Technology, Islamabad, Pakistan.

## References

- [1] A. Liu, J. Ming, and R. O. Ankumah, "Nitrate contamination in private wells in rural Alabama, United States," *Science of the Total Environment*, vol. 346, no. 1–3, pp. 112–120, 2005.
- [2] A. Nuhoglu, T. Pekdemir, E. Yildiz, B. Keskinler, and G. Akay, "Drinking water denitrification by a membrane bio-reactor," *Water Research*, vol. 36, no. 5, pp. 1155–1166, 2002.
- [3] F. Hell, J. Lahnsteiner, H. Frischherz, and G. Baumgartner, "Experience with full-scale electrodialysis for nitrate and hardness removal," *Desalination*, vol. 117, no. 1–3, pp. 173–180, 1998.
- [4] S. Samatya, N. Kabay, Ü. Yüksel, M. Arda, and M. Yüksel, "Removal of nitrate from aqueous solution by nitrate selective ion exchange resins," *Reactive and Functional Polymers*, vol. 66, no. 11, pp. 1206–1214, 2006.
- [5] S. K. Nataraj, K. M. Hosamani, and T. M. Aminabhavi, "Electrodialytic removal of nitrates and hardness from simulated mixtures using ion-exchange membranes," *Journal of Applied Polymer Science*, vol. 99, no. 4, pp. 1788–1794, 2006.
- [6] M. G. Rupert, "Decadal-scale changes of nitrate in ground water of the United States, 1988–2004," *Journal of Environmental Quality*, vol. 37, no. 5, pp. S240–S248, 2008.
- [7] D. Majumdar and N. Gupta, "Nitrate pollution of groundwater and associated human health disorders," *Indian Journal of Environmental Health*, vol. 42, no. 1, pp. 28–39, 2000.
- [8] B. C. Kross, A. D. Ayebo, and L. J. Fuortes, "Methemoglobinemia: nitrate toxicity in rural America," *American Family Physician*, vol. 46, no. 1, pp. 183–188, 1992.
- [9] L. Fewtrell, "Drinking-water nitrate, methemoglobinemia, and global burden of disease: a discussion," *Environmental Health Perspectives*, vol. 114, no. 11, pp. 1371–1374, 2004.
- [10] F. R. Greer and M. Shannon, "Infant methemoglobinemia: the role of dietary nitrate in food and water," *Pediatrics*, vol. 116, no. 3, pp. 784–786, 2005.
- [11] M. H. Ward, T. M. deKok, P. Levallois et al., "Workgroup report: drinking-water nitrate and health—recent findings and research needs," *Environmental Health Perspectives*, vol. 113, no. 11, pp. 1607–1614, 2005.
- [12] P. J. Squillace, J. C. Scott, M. J. Moran, B. T. Nolan, and D. W. Kolpin, "VOCs, pesticides, nitrate, and their mixtures in groundwater used for drinking water in the United States," *Environmental Science and Technology*, vol. 36, no. 9, pp. 1923–1930, 2002.
- [13] World Health Organization, *Revisions of the WHO Guidelines for Drinking Water Quality Report on a WHO Consultation*, WHO Regional Office for Europe, Medmenham, UK, 1992.
- [14] J. M. Symons, L. C. Bradley Jr., and T. C. Cleveland, *The Drinking Water Dictionary*, AWWA, McGraw-Hill, New York, NY, USA, 2001.
- [15] MWH, *Water Treatment Principles and Design*, John Wiley & Sons, Hoboken, NJ, USA, 2005.
- [16] A. Kapoor and T. Viraraghavan, "Nitrate removal from drinking water review," *Journal of Environmental Engineering*, vol. 123, no. 4, pp. 371–380, 1997.
- [17] A. Darbi, T. Viraraghavan, R. Butler, and D. Corkal, "Pilot-scale evaluation of select nitrate removal technologies," *Journal of Environmental Science and Health*, vol. 38, no. 9, pp. 1703–1715, 2003.
- [18] M. I. M. Soares, "Biological denitrification of groundwater," *Water, Air, and Soil Pollution*, vol. 123, no. 1–4, pp. 183–193, 2000.
- [19] I. F. Cheng, R. Muftikian, Q. Fernando, and N. Korte, "Reduction of nitrate to ammonia by zero-valent iron," *Chemosphere*, vol. 35, no. 11, pp. 2689–2695, 1997.
- [20] G. Yang and H. Lee, "Chemical reduction of nitrate by nano-sized iron: kinetics and pathways," *Water Research*, vol. 39, no. 5, pp. 884–894, 2005.
- [21] M. Kumar and S. Chakraborty, "Chemical denitrification of water by zero-valent magnesium powder," *Journal of Hazardous Materials*, vol. 135, no. 1–3, pp. 112–121, 2006.
- [22] F. He and D. Y. Zhao, "Preparation and characterization of a new class of starch-stabilized bimetallic nanoparticles for degradation of chlorinated hydrocarbons in water," *Environmental Science and Technology*, vol. 39, no. 9, pp. 3314–3320, 2005.
- [23] B. Schrick, J. L. Blough, A. D. Jones, and T. E. Mallouk, "Hydrodechlorination of trichloroethylene to hydrocarbons using bimetallic nickel-iron nanoparticles," *Chemistry of Materials*, vol. 14, no. 12, pp. 5140–5147, 2002.
- [24] F. He and D. Zhao, "Preparation and characterization of a new class of starch-stabilized bimetallic nanoparticles for degradation of chlorinated hydrocarbons in water," *Environmental Science and Technology*, vol. 39, no. 9, pp. 3314–3320, 2005.
- [25] S. Anders, M. F. Toney, T. Thomson et al., "X-ray absorption and diffraction studies of thin polymer/FePt nanoparticle assemblies," *Journal of Applied Physics*, vol. 93, no. 10, p. 6299, 2003.

## Research Article

# Silica Sol-Gel Entrapment of the Enzyme Chloroperoxidase

Tuan Le, Selina Chan, Bassem Ebaid, and Monika Sommerhalter

Department of Chemistry and Biochemistry, California State University East Bay, 25800 Carlos Bee Boulevard, Hayward, CA 94542, USA

Correspondence should be addressed to Monika Sommerhalter; [monika.sommerhalter@csueastbay.edu](mailto:monika.sommerhalter@csueastbay.edu)

Received 3 June 2015; Revised 24 August 2015; Accepted 31 August 2015

Academic Editor: Jiazhi Yang

Copyright © 2015 Tuan Le et al. This is an open access article distributed under the Creative Commons Attribution License, which permits unrestricted use, distribution, and reproduction in any medium, provided the original work is properly cited.

The enzyme chloroperoxidase (CPO) was immobilized in silica sol-gel beads prepared from tetramethoxysilane. The average pore diameter of the silica host structure (~3 nm) was smaller than the globular CPO diameter (~6 nm) and the enzyme remained entrapped after sol-gel maturation. The catalytic performance of the entrapped enzyme was assessed via the pyrogallol peroxidation reaction. Sol-gel beads loaded with 4  $\mu$ g CPO per mL sol solution reached 9–12% relative activity compared to free CPO in solution. Enzyme kinetic analysis revealed a decrease in  $k_{\text{cat}}$  but no changes in  $K_M$  or  $K_I$ . Product release or enzyme damage might thus limit catalytic performance. Yet circular dichroism and visible absorption spectra of transparent CPO sol-gel sheets did not indicate enzyme damage. Activity decline due to methanol exposure was shown to be reversible in solution. To improve catalytic performance the sol-gel protocol was modified. The incorporation of 5, 20, or 40% methyltrimethoxysilane resulted in more brittle sol-gel beads but the catalytic performance increased to 14% relative to free CPO in solution. The use of more acidic casting buffers (pH 4.5 or 5.5 instead of 6.5) resulted in a more porous silica host reaching up to 18% relative activity.

## 1. Introduction

Silica nanostructures can be fabricated using a room temperature sol-gel process that is compatible with biomolecules [1, 2]. The entrapment of enzymes inside these silica nanostructures has facilitated diverse applications in biocatalysis and biosensing [3]. Here, we demonstrate the use of sol-gel technology to make a biocatalyst based on entrapment of the enzyme chloroperoxidase (CPO) inside a silica nanostructure.

CPO (EC 1.11.1.10) is one of the most versatile heme enzymes known to date. It can be obtained as a secreted, glycosylated protein from the marine fungus *Caldariomyces fumago* [4, 5]. CPO catalyzes halogenation, sulfoxidation, hydroxylation, and epoxidation reactions with high substrate promiscuity under environmentally benign conditions [6]. CPO catalyzed oxidative transformations are based on hydrogen peroxide or an alkyl peroxide as oxidant, whereas the equivalent traditional chemical reactions require stoichiometric amounts of heavy metal salts [7]. Another advantageous feature of CPO is its ability to perform these reactions in a highly enantioselective manner [8]. Transforming CPO into a practical biocatalyst for oxidative transformations in

biosynthetic chemistry is therefore highly desirable. Further possible biotechnological applications of CPO include wastewater treatment or upgrading petroleum products [9–11]. The use of CPO as biocatalyst, however, is hampered by its loss of activity in the presence of organic solvents, deactivation at high concentrations of the oxidant  $\text{H}_2\text{O}_2$ , and instability at elevated temperatures [8, 12].

Various approaches have been attempted to improve the stability and productivity of CPO in solution [13–16] as well as in immobilized form [12, 17–21]. In our study, CPO was entrapped in a hydrogel prepared from the precursor tetramethoxysilane (TMOS) with or without the addition of methyltrimethoxysilane (MTMS). Enzyme immobilization offers key advantages, most notably ease of enzyme recovery and reusability [22]. Silica-based sol-gels furnish chemically inert and optically transparent immobilization matrices [2, 23]. However, sol-gel immobilization is often accompanied by a loss of enzymatic activity. This loss can be due to enzyme damage, leakage of enzyme from the immobilization host, or limited material transport of substrates and products within the sol-gel nanostructure. We examined each of these possible reasons using absorption and circular dichroism spectroscopy, porosimetry, and an enzyme activity assay for CPO,

that is, the peroxidation of pyrogallol. The effect of methanol on CPO was also investigated since methanol is released from the precursor TMOS during the hydrolysis and condensation reactions of the sol-gel process. In our attempts to optimize the catalytic performance of sol-gel immobilized CPO, we exploited the stability of CPO in acidic solutions [24] and deviated from the pH range of 6.0–7.0 which is typically employed in protein sol-gel immobilization procedures. The use of more acidic solutions in the sol-gel process might also be beneficial for various sol-gel applications based on other proteins that either withstand or thrive in acidic conditions.

## 2. Materials and Methods

**2.1. Materials.** CPO from *C. fumago* was purchased from Sigma-Aldrich. The turbid suspensions were centrifuged at 15,000 rpm for 5 minutes in an Eppendorf microcentrifuge. The concentrations of the CPO supernatants were determined via the intensity of the Soret band [25] and confirmed with protein assays [26]. The CPO samples used in this study had concentrations in the range of 9 to 15 mg/mL. All other reagents were purchased from Sigma-Aldrich or Fisher Scientific. Aqueous solutions were prepared with deionized water obtained from a Millipore Milli-Q device.

**2.2. Sol-Gel Entrapment.** A sol solution was prepared by mixing 50  $\mu$ L deionized water, 4.7  $\mu$ L 0.010 M hydrochloric acid, and 235  $\mu$ L TMOS in a microcentrifuge tube. If MTMS was included, TMOS and MTMS were premixed. The molar ratio of MTMS was either 5, 20, or 40% of the total MTMS and TMOS precursor mixture. The sol solution was sonicated in a Branson 1510 sonicator bath filled with ice water for 30 minutes and either used immediately thereafter or stored for up to a week at 4°C. In a microcentrifuge tube, 140  $\mu$ L sol, 480  $\mu$ L casting buffer, and 500  $\mu$ L diluted CPO solution were mixed. The casting buffers were prepared by mixing 0.1 M citric acid and 0.2 M dibasic sodium phosphate to reach pH values of 4.5, 5.5, 6.0, or 6.5. CPO was diluted in 20 mM potassium phosphate-potassium hydroxide buffer, pH 6.0. Small beads of 50  $\mu$ L volume were prepared by pipetting the mixture onto parafilm sheets. As the pH value of the casting buffer decreased the gelation time increased from approximately 15 minutes (pH 6.5) to 240 min (pH 4.5). The CPO sol-gel beads were transferred into glass tubes in sets of three to eight beads and covered with a storage buffer composed of 2.1 mL deionized water and 0.32 mL 0.1 M citric acid-0.2 M dibasic sodium phosphate buffer, pH 4.2. This storage buffer was typically exchanged with a new portion of storage buffer after one hour, and thereafter each day for seven or ten days. The storage temperature was 4°C.

**2.3. Activity Assays.** Activity assays were typically conducted in 0.1 M citric acid-0.2 M dibasic sodium phosphate buffer, pH 4.2 with 2.7 or 8.6 mM H<sub>2</sub>O<sub>2</sub>, 35 mM pyrogallol, and 0.2  $\mu$ g/mL CPO. CPO was added last to start the reaction. The assay volume was 3 mL. Control reactions without the enzyme were performed in parallel. The hydrogen peroxide and pyrogallol solutions were prepared fresh on the day of the measurements and pyrogallol was kept in the dark.

The absorbance increase at 420 nm was monitored every 3 seconds for 2 minutes using a NanoDrop 2000c (Thermo Fisher Scientific) with cuvette option. A molar absorptivity value of 2640 M<sup>-1</sup> cm<sup>-1</sup> for the product purpurogallin was used to calculate the enzyme activity [24]. One International Unit (IU) corresponds to the formation of one micromole purpurogallin in one minute at room temperature and pH 4.2.

For enzyme kinetic studies, the concentrations of the substrates pyrogallol and H<sub>2</sub>O<sub>2</sub> were varied. The substrate inhibition model described by (1) was used to fit the dependence of the initial reaction velocity,  $v_0$ , on the substrate concentration, [S]. The fit parameters are the Michaelis-Menten constant,  $K_M$ , the substrate inhibition constant,  $K_I$ , and the maximum initial reaction velocity,  $v_{\max}$ . The parameter  $v_{\max}$  depends on the turnover number,  $k_{\text{cat}}$ , and the enzyme concentration, [E]. The fit was carried out with the program EnzFitter from Biosoft:

$$v_0 = \frac{v_{\max} \cdot [S]}{K_M + [S] + [S]^2 / K_I} \quad \text{with } v_{\max} = k_{\text{cat}} \cdot [E]. \quad (1)$$

To detect how much CPO leaked from sol-gel beads, activity assays were conducted with the storage buffers that were removed and replaced during the maturation phase of the sol-gel beads. These assays were conducted in a similar manner as described above with the following exception: the assay was started with the addition of H<sub>2</sub>O<sub>2</sub> as no extra CPO was added.

Activity assays with CPO sol-gel beads were performed with longer time intervals of 20 or 30 seconds for a total duration of 5 minutes. A Milton Roy Spectronic 20D instrument was used to monitor the absorbance at 420 nm. Agitation of the reaction solution and the CPO sol-gel beads via inversion or pipetting was crucial to ensure good mixing in between absorbance recordings. Control reactions with sol-gel beads that did not contain CPO confirmed that the sol-gel beads themselves do not catalyze the peroxidation of pyrogallol.

**2.4. Spectroscopic Studies (CD and UV/VIS).** CD spectra were recorded with an AVIV Model 215 circular dichroism spectrometer at 25°C. The temperature was controlled with a thermostat. We employed the sample preparation method developed by Eggers and Valentine [27]. A buffer of low concentration (2 mM sodium phosphate, pH 7.0) was chosen to minimize total sample absorbance in the UV region. To achieve efficient gelation despite the low concentration of the buffer, a pH value of 7.0 was selected. A sol solution was prepared by sonicating 7.37 mL TMOS, 0.92 mL dH<sub>2</sub>O, and 0.88 mL 0.01 M hydrochloric acid for 20 minutes in an ice-water bath. A portion of 1.75 mL of this sol-gel solution was gently mixed with 2.625 mL CPO solution containing 12  $\mu$ M CPO in 2 mM sodium phosphate, pH 7.0, and cast into a plastic cassette of 1 mm thickness. The cassettes were purchased from Life Technologies. For the first four days, the storage buffer on top of the sol-gel sheet was exchanged daily. For complete maturation inside the more enclosed cassettes, the CPO sol-gel sheets were stored for one month at 4°C. Prior to the actual CD measurements, the cassette housing the CPO sol-gel was opened. A small piece was cut out with a razor blade and

transferred into a CD quartz cuvette of 2 mm thickness. The remaining space was filled with 2 mM sodium phosphate buffer, pH 7.0.

UV/VIS spectra were recorded using a UV mini 1240 Shimadzu single beam spectrophotometer. The CPO sol-gel material was prepared as described in Section 2.2. However, instead of casting beads, the solution was poured into 1 mm thick plastic cassettes and a higher CPO concentration yielding 1.6 mg/mL CPO in the final sol-gel sheet was used. The CPO sol-gel sheet was stored in the cassette for one month at 4°C. A rectangular piece was cut out and placed onto one wall of a plastic cuvette of 10 mm thickness. The CPO sol-gel sheet remained attached to the plastic wall after the cuvette was filled with 50 mM potassium phosphate buffer, pH 6.0. To test the effect of changing the pH value of buffers surrounding the CPO sol-gel sheets, the molarity of the potassium phosphate buffers at various pH values was increased to 0.5 M.

**2.5. Influence of Methanol on CPO's Catalytic Activity and Spectroscopic Properties.** CPO dissolved at concentrations of up to 9  $\mu$ M in 0.1 M citrate-0.2 M phosphate buffer, pH 4.2 was incubated with 11% v/v methanol. After specific time intervals, sample aliquots were removed to record UV/VIS or CD spectra or to measure the enzymatic activity via the pyrogallol peroxidation assay. Reference samples without methanol were prepared in parallel. To test whether any effects caused by methanol exposure might be reversible methanol treated samples were dialyzed for three hours in a Pierce Slide-A-Lyzer (10,000 MWCO) against 1 L of 0.01 M citrate-0.02 M phosphate buffer, pH 4.2 at room temperature.

**2.6. Porosimetry Measurements.** All porosimetry measurements were conducted with an ASAP 2020 physisorption analyzer from Micromeritics using nitrogen gas. To prepare the samples, the solvent exchange procedure described by Harreld and coworkers was used [28]. The sol-gel beads (typically 8) were placed in ~4 mL acetone overnight. The acetone was exchanged each day for three days. For the final two days, n-pentane was used instead of acetone. N-pentane and acetone are miscible with each other, but n-pentane evaporates more readily than acetone. This technique yields dry beads while minimizing the risk of pore collapse. The beads were placed in the sample degas station of the physisorption analyzer for approximately 8 hours at 37°C until constant pressure was reached. Nitrogen adsorption and desorption curves were recorded and analyzed with the Brunauer-Emmett-Teller (BET) algorithm. Proper performance of the instrument was confirmed with a silica-alumina standard provided by Micromeritics.

### 3. Results and Discussion

**3.1. Peroxidation of Pyrogallol Catalyzed by Free and Sol-Gel Entrapped CPO.** The catalytic activity of CPO was assessed by monitoring the peroxidation reaction of pyrogallol. To determine optimal reaction conditions, we varied the pH value of the assay buffer and the concentrations of pyrogallol and hydrogen peroxide. Our observations for free CPO agree well with previous studies [24, 29]. Acidic conditions, with

pH values in the range of 3.5 to 4.5, and pyrogallol concentrations at approximately 35 mM resulted in optimum catalytic performance. Very high pyrogallol concentrations gave rise to substrate inactivation, but the enzyme was even more sensitive towards inactivation by the cosubstrate  $\text{H}_2\text{O}_2$ . The  $\text{H}_2\text{O}_2$  concentration should not exceed 10 mM. The enzyme kinetic data obtained for sol-gel entrapped CPO displayed similar features albeit at much lower specific activity. Notably, sol-gel entrapment did not abolish the detrimental effect of  $\text{H}_2\text{O}_2$ . All data displayed in Figure 1 was thus fitted with a substrate inhibition model (see (1)).

The enzyme kinetic parameters for the peroxidation of pyrogallol catalyzed by free and sol-gel entrapped CPO are summarized in Table 1. Significantly smaller  $v_{\max}$  and thus  $k_{\text{cat}}$  values were obtained for sol-gel entrapped CPO compared to free CPO. The parameters  $K_m$  and  $K_I$  did not change significantly in response to sol-gel entrapment for either substrate. The poor quality of the fit shown in Figure 1(b) for the data on sol-gel entrapped CPO might be caused by large data point variations and the limitations of the substrate inhibition model. Manoj et al. [29] demonstrated that the substrate inhibition model used here (see (1)) can yield acceptable fits for individual substrate variations, but global fit parameters were shown to be unattainable [29]. For example, the  $K_M$  and  $K_I$  values of one substrate depended on the concentration of the other cosubstrate. All kinetic parameters determined here are thus only apparent values and the parameters for sol-gel entrapped CPO are further influenced by additional factors. For example,  $k_{\text{cat}}$  was calculated based on the assumption that all entrapped CPO molecules are able to participate in the catalytic process. This will not be the case for CPO molecules that are entrapped in closed silica pores or are otherwise permanently shielded and for CPO molecules with compromised functionality due to enzyme damage. The decrease in  $k_{\text{cat}}$  (and also  $v_{\max}$ ) might thus signify an apparent decrease in accessible and/or active CPO molecules upon sol-gel entrapment. Notably, hindered product release can also cause a decrease in  $k_{\text{cat}}$ . The  $k_{\text{cat}}$  value is either determined by the rate of catalytic turnover or the rate of product release, depending on which of the two steps is slower and thus rate-limiting. The silica nanostructure does not seem to impose any significant diffusional constraints on the molecules pyrogallol and possibly  $\text{H}_2\text{O}_2$ . If these substrate molecules were encountering substantial diffusional barriers, an increase in their apparent  $K_M$  and  $K_I$  values would be expected.

**3.2. Entrapment and Catalytic Performance of CPO in Sol-Gel Beads.** To further assess the entrapment and catalytic performance of the immobilized enzyme, different amounts of CPO were immobilized inside sol-gel beads corresponding to final concentrations of 40  $\mu$ g/mL, 8  $\mu$ g/mL, and 4  $\mu$ g/mL per total sol-gel solution. The storage buffer was exchanged to remove methanol originating from the hydrolysis and condensation steps of the sol-gel formation. CPO activity was measured in these exchanged buffer samples and compared to a reference sample with free CPO in solution to quantify enzyme leakage (see Figure 2). Higher enzyme loading resulted in more



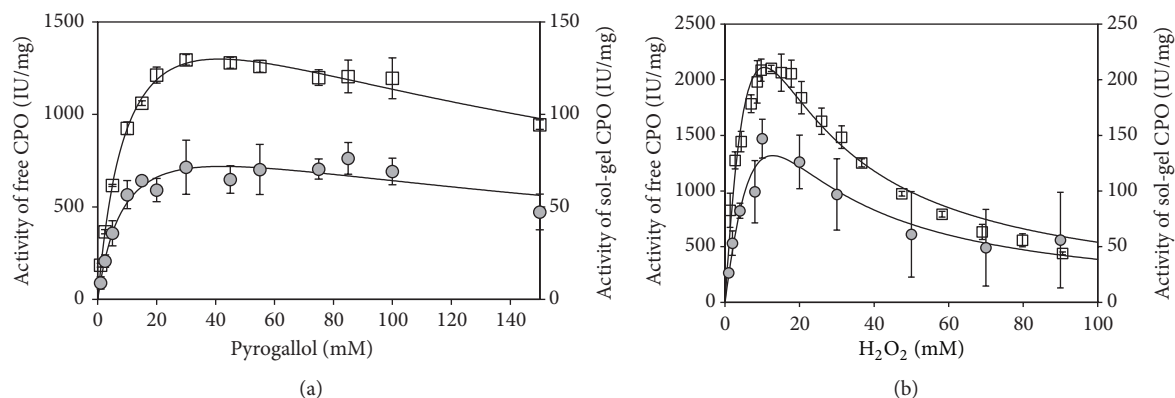


FIGURE 1: Peroxidation of pyrogallol catalyzed by free CPO (open squares; 0.575  $\mu$ g CPO in 3 mL total assay volume) and sol-gel entrapped CPO (grey circles; 0.575  $\mu$ g CPO entrapped in three sol-gel beads placed in 3 mL total assay volume). The CPO sol-gel beads were prepared from TMOS with a pH 6.0 casting buffer and matured for one week with a buffer exchange on every other day. The activity assays were performed in 0.1 M citric acid-0.2 M dibasic sodium phosphate buffer, pH 4.2 with constant concentrations of either 2.7 mM H<sub>2</sub>O<sub>2</sub> (a) or 35 mM pyrogallol (b). All data were measured in triplicate and are displayed as mean values  $\pm$  one standard deviation. The parameters of the curve fits are summarized in Table 1.

TABLE 1: Enzyme kinetic parameters for the CPO catalyzed peroxidation of pyrogallol\*.

	$K_M$ (mM)	$K_I$ (mM)	$v_{max}$ (IU/mg)	$k_{cat}$ (1/sec)
Pyrogallol				
Free CPO ( $R^2 = 0.983$ )	$11 \pm 1.0$	$160 \pm 20$	$2000 \pm 80$	$1400 \pm 60$
Sol-gel entrapped CPO ( $R^2 = 0.847$ )	$9.3 \pm 2.6$	$190 \pm 74$	$100 \pm 12$	$70 \pm 8.4$
H <sub>2</sub> O <sub>2</sub>				
Free CPO ( $R^2 = 0.921$ )	$17 \pm 6.2$	$6.4 \pm 2.2$	$9100 \pm 2500$	$6370 \pm 1750$
Sol-gel entrapped CPO ( $R^2 = 0.657$ )	$27 \pm 39$	$6.1 \pm 8.6$	$680 \pm 830$	$480 \pm 580$

\* Enzyme kinetic parameters were obtained by fitting the data shown in Figure 1(a) (pyrogallol) and Figure 1(b) (H<sub>2</sub>O<sub>2</sub>) to a substrate inhibition model (see (1)). All parameters are presented as value of the fit  $\pm$  one standard error of the fit.

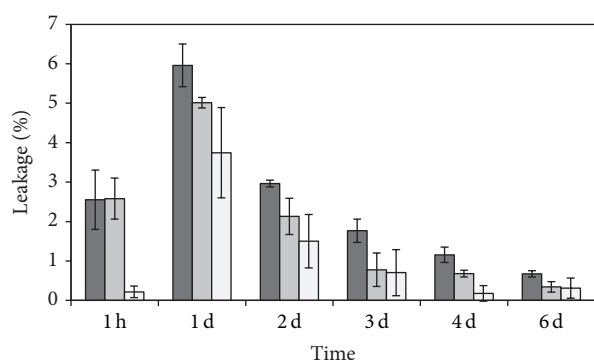


FIGURE 2: Three sets of CPO sol-gel beads with CPO concentrations of 40  $\mu$ g/mL (dark grey bars), 8  $\mu$ g/mL (grey bars), and 4  $\mu$ g/mL (light grey bars) were aged for one week. The storage buffer was replaced in the time intervals indicated on the graph and tested for CPO leakage. Each set was replicated three times and contained three beads per sample tube. The specific activity of the reference sample with free CPO in solution was  $1436 \pm 39$  IU/mg. The column heights represent the mean value and the error bars represent  $\pm$  one standard deviation.

enzyme leakage. As the sol-gel material matured and more connections formed within the silica mesh, enzyme leakage declined.

Table 2 contains the results of the activity measurements with the CPO sol-gel beads and summarizes the cumulative leakage over the first six days. The activity measurements were performed with CPO sol-gel beads that were seven days old. Each assay comprised 0.1 M citric acid-0.2 M dibasic sodium phosphate buffer, pH 4.2, 2.7 mM H<sub>2</sub>O<sub>2</sub>, and 35 mM pyrogallol. The CPO sol-gel beads with the highest CPO loading of 40  $\mu$ g CPO per mL sol-gel yielded the highest absolute activity values of  $249 \pm 33$  mIU. A comparison among specific activity values reported per mg of initially loaded CPO, however, clearly showed that the CPO sol-gel beads with a lower enzyme content of 8 or 4  $\mu$ g/mL performed better. At a higher loading of CPO, more CPO molecules might be obstructed by either other enzyme molecules or the silica nanostructure. Also, some of these CPO molecules might be entrapped in closed pores.

Another set of three tubes each containing three beads loaded with 4  $\mu$ g/mL CPO was aged for one week and tested for reusability (see Figure 3). The CPO sol-gel beads can be reused up to three times in a convenient manner by replacing the liquid phase composed of buffer and product molecules with new buffer and substrate. However, a further decline in catalytic performance was apparent. We also noticed that all CPO sol-gel beads adopted the yellow-orange color of the product purpurogallin after the first use. Gentle washing with



TABLE 2: Catalytic performance of sol-gel beads loaded with different CPO amounts.

CPO loading of sol-gel beads ( $\mu\text{g/mL}$ )	40	8	4
Activity (mIU)*	$249 \pm 33$	$138 \pm 18$	$76 \pm 4$
Specific activity (IU/mg)*	$41 \pm 6$	$115 \pm 15$	$127 \pm 6$
Relative activity compared to free CPO (%) <sup>#</sup>	2.9	8.0	8.80
Cumulative leakage for six days (%) <sup>†</sup>	15	12	7

\* Absolute activity values in mIU ( $\times 10^{-3}$  International Units) and specific activity values per mg initially loaded CPO are presented as mean values  $\pm$  one standard deviation. All sample sets were prepared in triplicate. <sup>#</sup>The relative activity was based on a reference assay with free CPO in solution. The reference value was  $1436 \pm 39$  IU/mg. <sup>†</sup>The cumulative leakage over six days of maturation corresponds to the summation of the leakage data shown in Figure 2.

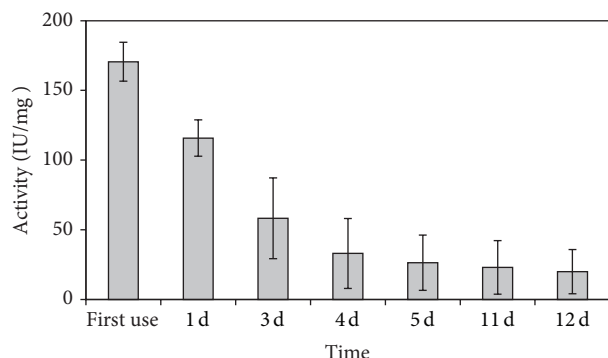


FIGURE 3: Reusability test for CPO sol-gel beads loaded with  $4 \mu\text{g/mL}$  CPO. Three sets, each with three beads per tube, were used in this test. The column heights represent the mean specific activity value and the error bars represent  $\pm$  one standard deviation. The first measurement was taken after the beads were aged for one week with daily buffer exchanges. The number of days that passed before the next reuse is listed on the  $x$ -axis.

the storage buffer diminished the coloration only slightly. Thus, clogging of the sol-gel nanostructure with product molecules was one factor that hampered the reusability of the CPO sol-gel beads. Furthermore, the peroxidation reactions catalyzed by CPO are prone to substrate inhibition (see Figure 1). Trapped pyrogallol and  $\text{H}_2\text{O}_2$  molecules could therefore interfere with effective reuse. Jung and Hartmann demonstrated that *in situ* generation of hydrogen peroxide via coimmobilization of glucose oxidase can improve the reusability of cross-linked CPO molecules entrapped in mesoporous molecular sieves [30].

The specific activity of three independently prepared sets of sol-gel beads all containing  $\sim 4 \mu\text{g/mL}$  CPO was different:  $70 \pm 15$  IU/mg (Figure 1),  $127 \pm 6$  IU/mg (Table 2), and  $171 \pm 14$  IU/mg (Figure 3). The CPO sol-gel materials used for generating the data presented in Table 2 and Figure 3 were prepared from the same CPO vial with a free CPO reference value of  $1436 \pm 39$  IU/mg. The reference value for the first CPO vial was only  $1280 \pm 80$  IU/mg. However, many other experimental parameters, such as the exact sol-gel composition, the quality of all starting materials, humidity, temperature, and duration of sol-gel drying phase, can also influence the properties of the final sol-gel material. Therefore, all CPO sol-gel beads that are compared within one table or graph were prepared on the same day with the same reagent batches in parallel.

**3.3. Modification of Sol-Gel Procedure with respect to Methanol Release.** Next, we tested whether minor modifications in the sol-gel procedure that influence the retention of methanol released from the sol-gel precursor TMOS would result in any significant changes. On the same day, three different sets of CPO sol-gel beads all containing  $4 \mu\text{g/mL}$  CPO were prepared in triplicate. The first set was prepared with a procedure that facilitates methanol release by using an open vessel while sonicating the sol solution and performing daily buffer exchanges during the first week of sol-gel maturation. The second and third sets were prepared using a closed sonication vessel and no buffer exchange was performed for the third set. Despite these modifications, all three sets prepared on the same day yielded virtually identical specific activity values of  $167 \pm 18$  IU/mg,  $164 \pm 10$  IU/mg, and  $178 \pm 21$  IU/mg, respectively. A more vigorous procedure presented by Ferrer et al. [31] involves rotavaporization of the sol solution prior to addition of the buffered enzyme solution. In our laboratory, this method was not successful as sol solidification started to set in too rapidly to achieve consistent gelation.

Overall, the catalytic performance of the best set of sol-gel beads was only  $12.5 \pm 1.5\%$  in comparison to the reference assay with free CPO in solution. Possible reasons for the decline in catalytic performance upon entrapment include (1) loss of enzyme due to leakage from the sol-gel matrix, (2) damage to the enzyme caused by the entrapment procedure, or (3) hindered substrate or product diffusion within the sol-gel nanostructure. As mentioned above, enzyme leakage did occur, but it can only account for a small loss of approximately 10%. In the experiments described below, we tested for the two remaining possible reasons for the decline in catalytic performance of the sol-gel entrapped CPO and also examined the effect of methanol on CPO.

**3.4. CD and UV/VIS Spectroscopy with Sol-Gel Entrapped CPO.** To monitor possible enzyme damage, we exploited the fact that sol-gels prepared from TMOS are transparent. Circular dichroism and visible absorbance spectra of free CPO in solution and CPO in sol-gel entrapped form are shown in Figures 4 and 5, respectively. The spectra of free CPO and sol-gel entrapped CPO are virtually identical to each other. Minor changes in intensity of the spectroscopic signals are most likely due to scattering effects from the sol-gel surface or the shrinkage of the sol-gel material during the maturation process. Shrinkage slightly raises the concentration of the sample but also decreases the spectroscopic path length. The CD spectra are typical for a protein with high alpha helical

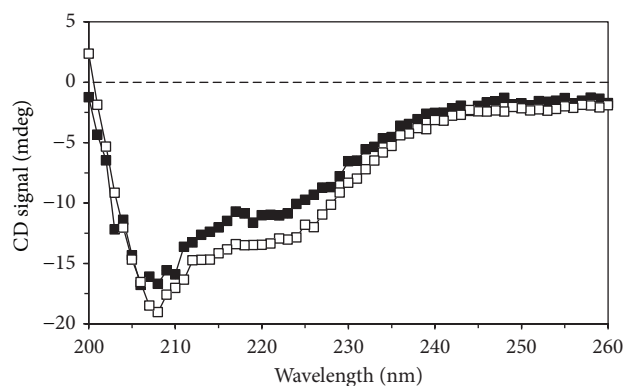


FIGURE 4: CD spectra of sol-gel entrapped CPO (black squares) and free CPO (white squares). The CPO concentration was  $7 \mu\text{M}$  in the silica sol-gel sheet of  $\sim 1 \text{ mm}$  thickness. The solution sample containing  $7 \mu\text{M}$  CPO in  $2 \text{ mM}$  sodium phosphate buffer, pH 7.0, was measured in a cuvette of  $1 \text{ mm}$  path length.

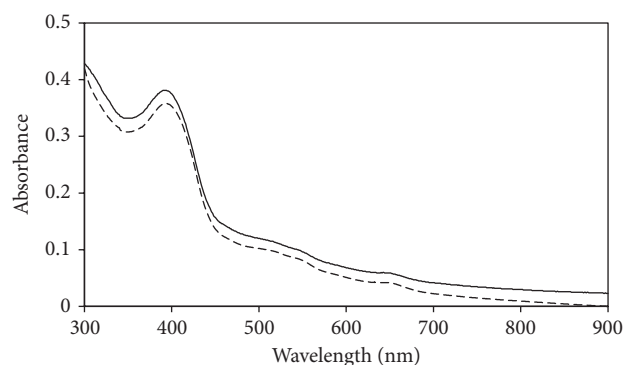


FIGURE 5: Absorbance spectra of sol-gel entrapped CPO (solid line) and free CPO (dashed line). The silica sol-gel sheet was  $\sim 1 \text{ mm}$  thick and contained  $1.6 \text{ mg/mL}$  CPO. The sheet was placed on the wall of a  $10 \text{ mm}$  wide plastic cuvette and immersed in  $50 \text{ mM}$  potassium phosphate buffer, pH 6.0. The solution reference sample was prepared from the same CPO stock via dilution to  $0.16 \text{ mg/mL}$  ( $4 \mu\text{M}$ ) with  $50 \text{ mM}$  potassium phosphate buffer, pH 6.0 in a  $10 \text{ mm}$  thick plastic cuvette.

content. This finding agrees with the X-ray protein structure of CPO [32] and previously determined CD data [15, 33].

The visible absorbance spectra shown in Figure 5 are typical for the active form of CPO with a five-coordinate iron center in the heme chromophore [34]. As the pH value increases above pH 7.0, CPO is inactivated, the iron center in the heme group becomes six-coordinate, and the Soret band shifts to a longer wavelength [34]. This spectroscopic transition can also be observed in CPO sol-gel sheets despite the entrapment of the enzyme inside the silica matrix. Figure 6 displays the absorption spectra of CPO sol-gel sheets immersed in  $0.5 \text{ M}$  phosphate buffers at pH values of 6.0, 8.0, and 10.0. In comparison to solution spectra, more alkaline conditions are necessary to achieve the Soret peak characteristic for sixfold coordinated heme iron centers. It is conceivable that the silanol groups in the sol-gel impose an additional buffering effect. According to Dunn and Zink [35],

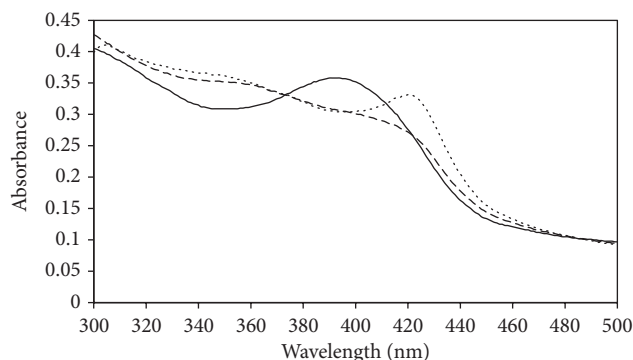


FIGURE 6: Absorbance spectra of sol-gel entrapped CPO immersed in  $0.5 \text{ M}$  potassium phosphate buffer with pH values of 6.0 (solid line), 8.0 (dashed line), and 10.0 (dotted line). The silica sol-gel sheets of  $1 \text{ mm}$  thickness loaded with  $1.6 \text{ mg/mL}$  CPO were placed on the wall of plastic cuvette with a path length of  $10 \text{ mm}$ .

the pH can be up to one pH unit lower inside a sol-gel pore than in the surrounding aqueous buffer.

The low apparent  $k_{\text{cat}}$  values for sol-gel entrapped CPO (see Table 1) indicate that a significant number of entrapped CPO molecules were unable to catalyze the peroxidation of pyrogallol in an effective manner. CD and visible absorption spectra, however, did not indicate any enzyme damage. It should be noted that both spectroscopic methods can only address specific features of the enzyme. These features are the overall secondary structure of the protein, the electronic configuration of the active site chromophore, and the ability to rearrange the coordination sphere of the heme iron center in response to an external change in pH value.

**3.5. Influence of Methanol on the Spectroscopic Features and Activity of Free CPO.** Methanol is released from the sol-gel precursor TMOS. If we assume complete hydrolysis of TMOS and no evaporation of methanol, the protein is exposed to a methanol concentration of 11% v/v as the buffered enzyme solution and the sol are mixed and pipetted onto the parafilm for gelation and drying. The transfer into storage buffer and the subsequent exchange of buffer drastically lower the methanol content during the maturation phase of the sol-gel. After the first buffer exchange, the methanol concentration is only 0.03% v/v.

To study the influence of methanol on the spectroscopic features of CPO, the enzyme was incubated with 11% v/v methanol and UV/VIS and CD spectra were recorded. We did not detect a change in the spectroscopic features of the CD spectra after several hours of incubation (data not shown), but methanol exposure did have a small and immediate effect on UV/VIS absorption spectra (see Figure 7). The absorption maximum of the Soret band shifted from  $396 \text{ nm}$  to  $400 \text{ nm}$ . Notably, this shift was reversible via dialysis. The methanol removal caused a 1.3-fold increase in sample volume. We adjusted the corresponding spectroscopic trace in Figure 7 for this dilution effect.

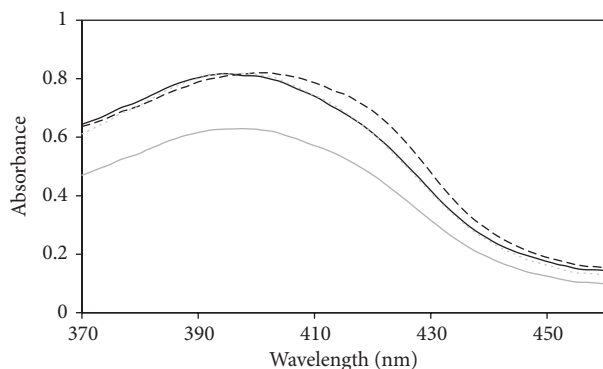


FIGURE 7: Absorption spectra of 9  $\mu\text{M}$  CPO in 0.1 M citrate-0.2 M phosphate buffer, pH 4.2 (solid line), in 11% v/v methanol and 0.1 M citrate-0.2 M phosphate buffer, pH 4.2 (dashed line), dialyzed sample (grey solid line), and dialyzed sample adjusted for 1.3-fold volume increase (grey dotted line).

In agreement with previous studies [36], we observed a drastic decline in CPO's catalytic performance after incubation of CPO with organic solvents. Compared to an aqueous reference sample without methanol, only 57% residual activity was detected after incubation with 11% v/v methanol for 2 hours. After one day, the residual activity still remained at 57%. We further discovered that the detrimental effect of methanol was reversible. Up to 96% of the sample's initial activity was recovered after dialysis. Sample dilution also resulted in the enzyme's recovery. Decreasing the methanol content to 5% or 1% v/v via sample dilution resulted in 90% and 100% relative activity in comparison to identically diluted samples from the same CPO batch that were not exposed to methanol. Our finding that damage caused by methanol was reversible in solution has implications for other studies on the use of CPO in organic solvents or in biphasic solvent systems [36, 37]. Several CPO substrates which can be converted into products of industrial interest have high solubility in nonpolar organic solvents [8].

Also, if any initial damage caused by methanol exposure was also reversible for sol-gel entrapped CPO, immediate reduction in methanol content via evaporation of methanol from the sol solution or daily buffer exchanges during the gel maturation phase would not critically alter the final performance of the CPO sol-gel beads. This might explain why the three different, but parallel, preparations outlined in Section 3.3 resulted in virtually identical performance for the three different CPO sol-gel bead sets. On the other hand, manifestation of unrecoverable enzyme damage would explain the low apparent  $k_{\text{cat}}$  values determined for sol-gel entrapped CPO (see Table 1). It is conceivable that recovery from damage caused by methanol exposure is less effective for CPO molecules entrapped within the silica sol-gel host compared to free CPO in solution.

**3.6. Hindered Material Transport in CPO Sol-Gel Beads.** After their first use, all CPO sol-gel beads adopted a persistent yellow coloration indicating the entrapment of the product purpurogallin. Attractive intermolecular forces and physical

constraints both can delay the release of product molecules from the silica nanostructure. If product release becomes rate-limiting, the apparent  $k_{\text{cat}}$  value decreases as observed in the enzyme kinetic analysis. Hindered substrate diffusion, however, was not supported by enzyme kinetic experiments as the  $K_M$  and  $K_I$  values for the main substrate pyrogallol were virtually identical for sol-gel entrapped and free CPO (see Table 1). We cannot explain why pyrogallol and purpurogallin would show different material transport properties inside the silica nanostructure. Both molecules have similar functional groups and purpurogallin (MW 220 g/mol) is only somewhat larger than pyrogallol (MW 116 g/mol). An alternative explanation would involve side-reactions forming alternate charged products or the trapping of reactive, colored intermediates.

The alternative peroxidation substrate 2,2'-azino-bis(3-ethylbenzothiazoline-6-sulfonic acid) (ABTS) is particularly large (MW 515 g/mol) and the product of the peroxidation reaction carries a positive charge [24]. Deprotonated silanol groups on the sol-gel surface can provide negative countercharges. The catalytic performance of CPO sol-gel beads dropped from  $12.6 \pm 3\%$  with the substrate pyrogallol to  $9 \pm 0.4\%$  with the substrate ABTS relative to the corresponding assay with free CPO in solution. The CPO sol-gel beads adopted the green color of the ABTS peroxidation product. Kadnikova and coworkers observed the formation of several side products for the peroxidation reaction of ABTS by horseradish peroxidase in a sol-gel matrix [38]. The peroxidation reaction with ABTS and possibly other substrates, including pyrogallol, might therefore be more complex than in solution.

We further observed that preequilibration of CPO sol-gel beads with pyrogallol considerably improved catalytic performance. For example, preequilibration with 72 mM pyrogallol for 3 hours in comparison to using 35 mM pyrogallol without preequilibration increased the relative activity from 12.3 to 19.6%. The strategy to preequilibrate enzyme sol-gel materials with an excess of substrate before adding a cosubstrate was already successfully applied by Smith and coworkers [23] in their study on sol-gel encapsulated horseradish peroxidase. Based on the data presented in Figure 1(a), however, we would not expect an increase in catalytic performance for sol-gel entrapped CPO as the pyrogallol concentration is raised from 35 to 72 mM. In fact, substrate inhibition should slightly lower the activity of CPO. Adsorption of pyrogallol molecules to the sol-gel surface or physical entrapment could further enhance the local effective concentration of pyrogallol around the enzyme. One key difference between the experiment leading to Figure 1(a) and the preequilibration experiment is the timing of adding the cosubstrate  $\text{H}_2\text{O}_2$ . Manoj et al. [29] argue that substrate inhibition of CPO is not simply caused by blocking the active site of the enzyme with excess substrate molecules. Instead they propose more complex substrate inhibition mechanisms that involve secondary conversion of an already formed product or competition by transient intermediates leading to alternate products. Both substrate inhibition scenarios require the immediate presence of the cosubstrate  $\text{H}_2\text{O}_2$ .

TABLE 3: Properties of CPO sol-gel beads prepared with different casting buffers.

pH of casting buffer	4.5	5.5	6.5
BET surface area (m <sup>2</sup> /g)	710 ± 40*	740 ± 60	470 ± 40
Total pore volume (cm <sup>3</sup> /g)	0.58 ± 0.02	0.60 ± 0.06	0.32 ± 0.04
Average pore diameter (nm)	3.3 ± 0.3	3.2 ± 0.1	2.7 ± 0.1
Activity (mIU)	251 ± 2	242 ± 29	161 ± 13
Specific activity (IU/mg)	157 ± 1	151 ± 18	100 ± 8
Activity compared to free CPO (%) <sup>#</sup>	18	17	11
Cumulative leakage (%) <sup>†</sup>	13	14	9

\* All data are presented as mean values ± one standard deviation of triplicate data sets. <sup>#</sup>The relative activity was based on a reference assay with free CPO in solution yielding 887 ± 31 IU/mg. <sup>†</sup>The cumulative leakage over ten days of maturation corresponds to the summation of the leakage data shown in Figure 8.

**3.7. Modification of Sol-Gel Procedure Using MTMS.** To modify the surface of the sol-gel material, we incorporated MTMS at molar ratios of 5, 20, and 40% in the sol solution. The addition of MTMS will introduce nonpolar methyl groups rendering the surface of the silica nanostructure more hydrophobic [39]. The casting buffer had a pH value of 6.0 and the total CPO loading was 4 µg/mL. The addition of MTMS resulted in longer gelation times, for example, up to 240 minutes for a molar ratio of 40% MTMS. Unfortunately, the beads prepared with MTMS were more brittle and fragile than any of the other CPO sol-gel beads prepared in this study. The brittleness of the beads rendered their handling more challenging. Regardless of the amount of incorporated MTMS, the activity was approximately 14 ± 1% compared to a solution reference assay. The cumulative leakage often exceeded 20%. We cannot rule out that the physical instability of the beads during and after a buffer exchange might have contributed to higher apparent leakage and higher apparent activity values. In contrast to other enzymes, notably lipase, which showed interfacial activation and performed better inside more hydrophobic nanostructures [40], the incorporation of MTMS into the CPO sol-gel material did not improve catalytic performance in a systematic manner.

**3.8. Modification of Sol-Gel Procedure Using More Acidic Casting Buffers.** The enzyme CPO is stable under acidic conditions [24]. We exploited this CPO specific property and prepared CPO sol-gel beads using casting buffers with pH values of 4.5, 5.5, and 6.5. All sample preparations were conducted in parallel with the same batches of CPO, TMOS, and buffer reagents. The gelation time increased with more acidic casting buffers, but the sol-gel beads remained easy to handle and transparent. The CPO loading was 4 µg/mL. All CPO sol-gel preparations were divided into two portions. One portion was used for porosimetry studies and the other portion was used for leakage and activity measurements (see Table 3). The properties of CPO sol-gel beads cast at pH 4.5 and 5.5 are virtually identical, but the CPO sol-gel beads cast at pH 6.5 show significantly lower values in all categories. This indicates a change in the matrix formation of the sol-gel as the casting pH drops to or below pH 5.5. Overall, the porosimetry data is positively correlated with catalytic performance and, unfortunately, leakage. All three porosimetric properties, including larger average pore size, BET surface area, and pore

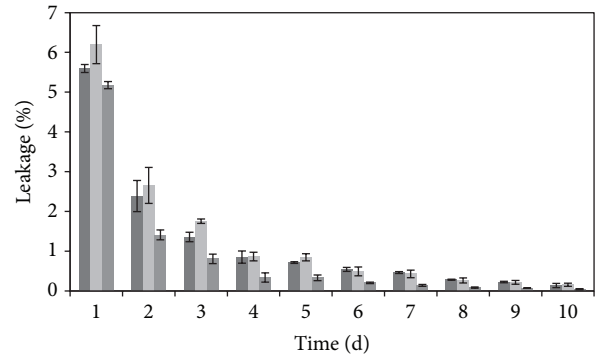


FIGURE 8: The storage buffer of CPO sol-gel beads prepared with casting buffers at pH 4.5 (dark grey bars), 5.5 (grey bars), and 6.5 (light grey bars) was exchanged on a daily basis and monitored for CPO activity. All samples were prepared in triplicate with eight CPO sol-gel beads per sample tube. The bar height represents the mean value and the error bar ± one standard deviation.

volume, indicate reduced steric hindrance for material transport inside the sol-gel nanostructure. As a consequence, catalytic performance increased. Smaller average pore sizes, on the other hand, can aid in the retention of CPO.

The dimensions of the protein CPO are 5.3 nm × 4.6 nm × 6.0 nm [19]. The average pore diameters of approximately 3 nm are only slightly smaller than the size of CPO. Nevertheless, CPO remained well entrapped after completion of the sol-gel maturation phase. Attractive electrostatic forces did not most likely aid in the retention of CPO as the storage buffer had a pH value of 4.2 which is close to the isoelectric point of CPO. The isoelectric point of CPO from *C. fumago* was calculated to be approximately 4.0 [18, 21]. Isoelectric focusing experiments on CPO from *Pseudomonas pyrruginia* yielded an isoelectric point of 4.1 [41]. For all buffer conditions employed in our study, the net charge on the surface of CPO is therefore either close to zero or negative.

Our observation that more acidic casting buffers result in greater porosimetry of sol-gels agrees well with several previous studies [42, 43]. However, not all enzymes will respond well to the use of more acidic casting conditions. Notably, enzymes have different pH profiles and some enzymes are inactive under acidic conditions. Sol-gel entrapped cholinesterase, for example, showed better performance



in silica nanostructures prepared at pH values of 7.0 and 8.0 and then 6.0 [44].

#### 4. Conclusion

The enzyme CPO was successfully entrapped inside a silica nanostructure prepared from the precursor TMOS with or without addition of the hydrophobic modifier MTMS. Since CPO is stable in acidic buffers, we further modified the sol-gel procedure by using casting buffers with pH values of 4.5, 5.5, 6.0, and 6.5. The catalytic performance of optimized CPO sol-gel beads approached 18% relative to free CPO in solution as assessed via the pyrogallol peroxidation assay. A combination of factors, such as enzyme leakage from the sol-gel host, insufficient recovery from inactivation caused by initial methanol exposure, hindered product release, or alternate reaction pathways, are most likely responsible for the decline in catalytic performance of CPO after sol-gel entrapment. The use of more acidic casting buffers in the sol-gel procedure provided the most leverage for optimization by yielding more porous silica nanostructures. Overall, our findings are of importance for the optimization of other sol-gel materials devised for applications in biosensing or biocatalysis or designed for the controlled release of bioactive compounds.

#### Conflict of Interests

The authors declare that there is no conflict of interests regarding the publication of this paper.

#### Acknowledgments

Funding for this project was obtained from the Research Corporation for Science Advancement (Cottrell College Science Award to Monika Sommerhalter) and California State University East Bay (Faculty and Student Research Grants to Monika Sommerhalter, Selina Chan, and Tuan Le and a Sieber-Tombari award to Monika Sommerhalter). Professor Daryl Eggers, San Jose State University, kindly invited the authors to perform the CD measurements in his laboratory. The authors are also grateful to Professor Ann McPartland for providing detailed feedback on their paper.

#### References

- [1] B. C. Dave, B. Dunn, J. S. Valentine, and J. I. Zink, "Nanoconfined proteins and enzymes: sol-gel-based biomolecular materials," *Nanotechnology, ACS Symposium Series*, vol. 622, pp. 351–365, 1996.
- [2] I. Gill and A. Ballesteros, "Bioencapsulation within synthetic polymers (part 1): sol-gel encapsulated biologicals," *Trends in Biotechnology*, vol. 18, no. 7, pp. 282–296, 2000.
- [3] D. Avnir, T. Coradin, O. Lev, and J. Livage, "Recent bio-applications of sol-gel materials," *Journal of Materials Chemistry*, vol. 16, no. 11, pp. 1013–1030, 2006.
- [4] D. R. Morris and L. P. Hager, "Chloroperoxidase. I. Isolation and properties of the crystalline glycoprotein," *The Journal of Biological Chemistry*, vol. 241, no. 8, pp. 1763–1768, 1966.
- [5] V. Yazbik and M. Ansorge-Schumacher, "Fast and efficient purification of chloroperoxidase from *C. fumago*," *Process Biochemistry*, vol. 45, no. 2, pp. 279–283, 2010.
- [6] M. Hofrichter and R. Ullrich, "Heme-thiolate haloperoxidases: versatile biocatalysts with biotechnological and environmental significance," *Applied Microbiology and Biotechnology*, vol. 71, no. 3, pp. 276–288, 2006.
- [7] V. M. Dembitsky, "Oxidation, epoxidation and sulfoxidation reactions catalysed by haloperoxidases," *Tetrahedron*, vol. 59, no. 26, pp. 4701–4720, 2003.
- [8] L. Santhanam and J. S. Dordick, "Chloroperoxidase catalyzed epoxidation of styrene in aqueous and non-aqueous media," *Biocatalysis and Biotransformation*, vol. 20, no. 4, pp. 265–274, 2002.
- [9] M. Ayala, N. R. Robledo, A. Lopez-Munguia, and R. Vazquez-Duhalt, "Substrate specificity and ionization potential in chloroperoxidase-catalyzed oxidation of diesel fuel," *Environmental Science and Technology*, vol. 34, no. 13, pp. 2804–2809, 2000.
- [10] R. Vázquez-Duhalt, M. Ayala, and F. J. Márquez-Rocha, "Biocatalytic chlorination of aromatic hydrocarbons by chloroperoxidase of *Caldariomyces fumago*," *Phytochemistry*, vol. 58, no. 6, pp. 929–933, 2001.
- [11] E. Terrés, M. Montiel, S. Le Borgne, and E. Torres, "Immobilization of chloroperoxidase on mesoporous materials for the oxidation of 4,6-dimethyldibenzothiophene, a recalcitrant organic sulfur compound present in petroleum fractions," *Biotechnology Letters*, vol. 30, no. 1, pp. 173–179, 2008.
- [12] V. Trevisan, M. Signoreto, S. Colonna, V. Pironti, and G. Strukul, "Microencapsulated chloroperoxidase as a recyclable catalyst for the enantioselective oxidation of sulfides with hydrogen peroxide," *Angewandte Chemie International Edition*, vol. 43, no. 31, pp. 4097–4099, 2004.
- [13] N. Spreti, R. Germani, A. Incani, and G. Savelli, "Stabilization of chloroperoxidase by polyethylene glycols in aqueous media: kinetic studies and synthetic applications," *Biotechnology Progress*, vol. 20, no. 1, pp. 96–101, 2004.
- [14] J.-B. Park and D. S. Clark, "New reaction system for hydrocarbon oxidation by chloroperoxidase," *Biotechnology and Bioengineering*, vol. 94, no. 1, pp. 189–192, 2006.
- [15] J.-Z. Liu and M. Wang, "Improvement of activity and stability of chloroperoxidase by chemical modification," *BMC Biotechnology*, vol. 7, no. 1, article 23, 2007.
- [16] L. Zhi, Y. Jiang, Y. Wang, M. Hu, S. Li, and Y. Ma, "Effects of additives on the thermostability of chloroperoxidase," *Biotechnology Progress*, vol. 23, no. 3, pp. 729–733, 2007.
- [17] T. A. Kadima and M. A. Pickard, "Immobilization of chloroperoxidase on aminopropyl-glass," *Applied and Environmental Microbiology*, vol. 56, no. 11, pp. 3473–3477, 1990.
- [18] Y.-J. Han, J. T. Watson, G. D. Stucky, and A. Butler, "Catalytic activity of mesoporous silicate-immobilized chloroperoxidase," *Journal of Molecular Catalysis B: Enzymatic*, vol. 17, no. 1, pp. 1–8, 2002.
- [19] J. Aburto, M. Ayala, I. Bustos-Jaimes et al., "Stability and catalytic properties of chloroperoxidase immobilized on SBA-16 mesoporous materials," *Microporous and Mesoporous Materials*, vol. 83, no. 1–3, pp. 193–200, 2005.
- [20] M. Hartmann and C. Streb, "Selective oxidation of indole by chloroperoxidase immobilized on the mesoporous molecular sieve SBA-15," *Journal of Porous Materials*, vol. 13, no. 3–4, pp. 347–352, 2006.



- [21] S. Hudson, J. Cooney, B. K. Hodnett, and E. Magner, "Chloroperoxidase on periodic mesoporous organosilanes: immobilization and reuse," *Chemistry of Materials*, vol. 19, no. 8, pp. 2049–2055, 2007.
- [22] R. A. Sheldon, "Enzyme immobilization: the quest for optimum performance," *Advanced Synthesis & Catalysis*, vol. 349, no. 8–9, pp. 1289–1307, 2007.
- [23] K. Smith, N. J. Silvernail, K. R. Rodgers, T. E. Elgren, M. Castro, and R. M. Parker, "Sol-gel encapsulated horseradish peroxidase: a catalytic material for peroxidation," *Journal of the American Chemical Society*, vol. 124, no. 16, pp. 4247–4252, 2002.
- [24] K. M. Manoj and L. P. Hager, "Chloroperoxidase, a janus enzyme," *Biochemistry*, vol. 47, no. 9, pp. 2997–3003, 2008.
- [25] V. M. Samokyszyn and P. R. Ortiz de Montellano, "Topology of the chloroperoxidase active site: regiospecificity of heme modification by phenylhydrazine and sodium azide," *Biochemistry*, vol. 30, no. 50, pp. 11646–11653, 1991.
- [26] M. M. Bradford, "A rapid and sensitive method for the quantitation of microgram quantities of protein utilizing the principle of protein-dye binding," *Analytical Biochemistry*, vol. 72, no. 1–2, pp. 248–254, 1976.
- [27] D. K. Eggers and J. S. Valentine, "Molecular confinement influences protein structure and enhances thermal protein stability," *Protein Science*, vol. 10, no. 2, pp. 250–261, 2001.
- [28] J. H. Harreld, T. Ebina, N. Tsubo, and G. Stucky, "Manipulation of pore size distributions in silica and ormosil gels dried under ambient pressure conditions," *Journal of Non-Crystalline Solids*, vol. 298, no. 2–3, pp. 241–251, 2002.
- [29] K. M. Manoj, A. Baburaj, B. Ephraim et al., "Explaining the atypical reaction profiles of heme enzymes with a novel mechanistic hypothesis and kinetic treatment," *PLoS ONE*, vol. 5, no. 5, Article ID e10601, 2010.
- [30] D. Jung and M. Hartmann, "Oxidation of indole with CPO and GOx immobilized on mesoporous molecular sieves," *Catalysis Today*, vol. 157, no. 1–4, pp. 378–383, 2010.
- [31] M. L. Ferrer, F. del Monte, and D. Levy, "A novel and simple alcohol-free sol-gel route for encapsulation of labile proteins," *Chemistry of Materials*, vol. 14, no. 9, pp. 3619–3621, 2002.
- [32] M. Sundaramoorthy, J. Ternner, and T. L. Poulos, "The crystal structure of chloroperoxidase: a heme peroxidase-cytochrome P450 functional hybrid," *Structure*, vol. 3, no. 12, pp. 1367–1377, 1995.
- [33] X. W. Yi, A. Conesa, P. J. Punt, and L. P. Hager, "Examining the role of glutamic acid 183 in chloroperoxidase catalysis," *Journal of Biological Chemistry*, vol. 278, no. 16, pp. 13855–13859, 2003.
- [34] S. R. Blanke, S. A. Martinis, S. G. Sligar, L. P. Hager, J. J. Rux, and J. H. Dawson, "Probing the heme iron coordination structure of alkaline chloroperoxidase," *Biochemistry*, vol. 35, no. 46, pp. 14537–14543, 1996.
- [35] B. Dunn and J. I. Zink, "Probes of pore environment and molecule-matrix interactions in sol-gel materials," *Chemistry of Materials*, vol. 9, no. 11, pp. 2280–2291, 1997.
- [36] W. A. Loughlin and D. B. Hawkes, "Effect of organic solvents on a chloroperoxidase biotransformation," *Bioresource Technology*, vol. 71, no. 2, pp. 167–172, 2000.
- [37] E. Kiljunen and L. T. Kanerva, "Chloroperoxidase-catalysed oxidation of alcohols to aldehydes," *Journal of Molecular Catalysis B: Enzymatic*, vol. 9, no. 4–6, pp. 163–172, 2000.
- [38] E. N. Kadnikova and N. M. Kostić, "Oxidation of ABTS by hydrogen peroxide catalyzed by horseradish peroxidase encapsulated into sol-gel glass. Effects of glass matrix on reactivity," *Journal of Molecular Catalysis B: Enzymatic*, vol. 18, no. 1–3, pp. 39–48, 2002.
- [39] A. Venkateswara Rao and D. Haranath, "Effect of methyltrimethoxysilane as a synthesis component on the hydrophobicity and some physical properties of silica aerogels," *Microporous and Mesoporous Materials*, vol. 30, no. 2–3, pp. 267–273, 1999.
- [40] M. T. Reetz, A. Zonta, and J. Simpelkamp, "Efficient immobilization of lipases by entrapment in hydrophobic sol-gel materials," *Biotechnology and Bioengineering*, vol. 49, no. 5, pp. 527–534, 1996.
- [41] W. Wiesner, K.-H. van Pee, and F. Lingens, "Purification and characterization of a novel bacterial non-heme chloroperoxidase from *Pseudomonas pyrocinia*," *Journal of Biological Chemistry*, vol. 263, no. 27, pp. 13725–13732, 1988.
- [42] Y. Xi, Z. Liangying, and W. Sasa, "Pore size and pore-size distribution control of porous silica," *Sensors and Actuators: B. Chemical*, vol. 25, no. 1–3, pp. 347–352, 1995.
- [43] C. Lin and J. A. Ritter, "Effect of synthesis pH on the structure of carbon xerogels," *Carbon*, vol. 35, no. 9, pp. 1271–1278, 1997.
- [44] M. Altstein, G. Segev, N. Aharonson, O. Ben-Aziz, A. Tur-niansky, and D. Avnir, "Sol-gel entrapped cholinesterases: a microtiter plate method for monitoring anti-cholinesterase compounds," *Journal of Agricultural and Food Chemistry*, vol. 46, no. 8, pp. 3318–3324, 1998.

## Research Article

# Synthesis and Application of Magnetic Photocatalyst of Ni-Zn Ferrite/TiO<sub>2</sub> from IC Lead Frame Scraps

Robert Liu and H. T. Ou

*Department of Chemical and Materials Engineering, Minghsin University of Science and Technology, Hsinchu 30401, Taiwan*

Correspondence should be addressed to Robert Liu; robertl@must.edu.tw

Received 4 June 2015; Accepted 20 August 2015

Academic Editor: Oded Millo

Copyright © 2015 R. Liu and H. T. Ou. This is an open access article distributed under the Creative Commons Attribution License, which permits unrestricted use, distribution, and reproduction in any medium, provided the original work is properly cited.

IC lead frame scraps with about 18.01% tin, 34.33% nickel, and 47.66% iron in composition are industrial wastes of IC lead frame production. The amount of thousand tons of frame scraps in Taiwan each year is treated as scrap irons. Ni-Zn ferrites used in high frequent inductors and filters are produced from Ni-Zn ferrite powders by pressing and sintering. The amount of several ten thousand tons of ferrites of Ni<sub>1-x</sub>Zn<sub>x</sub>Fe<sub>2</sub>O<sub>4</sub> in compositions is consumed annually in the whole world. Therefore, these IC lead frame scraps will be used in this research as raw materials to fabricate magnetic ferrite powders and combined subsequently with titanium sulfate and urea to produce magnetic photocatalysts by coprecipitation for effective waste utilization. The prepared Ni-Zn ferrite powder and magnetic photocatalyst (Ni-Zn ferrite/TiO<sub>2</sub>) were characterized by ICP, XRF, XRD, EDX, SEM, SQUID, and BET. The photocatalytic activity of synthesized magnetic photocatalysts was tested by FBL dye wastewater degradation. TOC and ADMI measurement for degradation studies were carried out, respectively. Langmuir-Hinshelwood kinetic model of the prepared magnetic TiO<sub>2</sub> proved available for the treatments. Wastes are transformed to valuable magnetic photocatalysts in this research to solve the separation problem of wastewater and TiO<sub>2</sub> photocatalysts by magnetic field.

## 1. Introduction

Wastewaters from textile and dyeing industries are highly colored by various nonbiodegradable dyes which cause serious environmental problems [1]. Advanced oxidation processes such as UV/H<sub>2</sub>O<sub>2</sub> [2], ozonation [3–5], Fenton processes [5–8], ozone/Fenton [9], and TiO<sub>2</sub> and modified TiO<sub>2</sub> [10–17] are promising alternatives for the mineralization of textile dyes or other pollutants. Among them, semiconductor TiO<sub>2</sub>'s simultaneous photocatalytic oxidation and reduction show significant potential due to being photoreactive, nontoxic, chemically and biologically inert, photostable, and lower in cost. Among different advanced oxidation processes (AOPs), a brand new AOP, sonolysis or hybrid AOP, combined with sonolysis has drawn increasing attention as it generates ·OH free radical through transient cavitation by ultrasound irradiation [18–20]. Cavitation is essentially the nucleation, growth, and transient implosive collapse of gas bubbles driven by ultrasound wave.

The well-known nickel-zinc ferrite is of special technological significance, particularly at high frequencies, because

of its high resistivity and low eddy current losses. Several methods are conventionally used for the synthesis of these nanosized ferrites such as ceramic [21, 22], sol-gel [23, 24], coprecipitation [25], hydrothermal method [26, 27], citrate precursor method [28, 29], and autocombustion method [29, 30]. Sonochemical approach is considerably new to synthesize ferrite in which ferrite nanoparticles are prepared by ultrasound irradiation or sonication of the reaction mixture [31].

Despite existing technologies, separation difficulty of nanosized TiO<sub>2</sub> particles from treated wastewater still remains. Fixed-film-TiO<sub>2</sub> systems are undermined due to immobility while magnetic TiO<sub>2</sub> offers to overcome this limitation. For example, Chen and Zhao [32] reported a magnetically separable photocatalyst of TiO<sub>2</sub>/SiO<sub>2</sub>/γ-Fe<sub>2</sub>O<sub>3</sub> prepared by solid phase synthesis. The addition of a SiO<sub>2</sub> membrane between the γ-Fe<sub>2</sub>O<sub>3</sub> core and the TiO<sub>2</sub> shell weakened the adverse effects of γ-Fe<sub>2</sub>O<sub>3</sub> on the photocatalysis of TiO<sub>2</sub>. Photocatalysts in Chen and Zhao's article showed good photocatalytic activity and could be separated from the

solution with magnetic field. Gao et al. [33] synthesized a magnetically separated photocatalyst of  $\text{TiO}_2/\gamma\text{-Fe}_2\text{O}_3$  by sol-gel method. The sample sintered at  $500^\circ\text{C}$  displayed the highest degradation activity for acridine dye aqueous solution, with the optimal  $\text{TiO}_2$  supporting amount approximating 50%. Fu et al. [34] successfully prepared  $\text{TiO}_2/\text{NiCuZn}$  ferrite composite powder as a magnetic photocatalyst. The core  $\text{NiCuZn}$  ferrite powder was synthesized with the waste material from steel and electroplating industries.  $\text{TiO}_2$  nanocrystal shell was prepared by sol-gel hydrolysis of titanium isopropoxide with  $\text{NiCuZn}$  ferrite powder followed by heat treatment. In their study, the optimum dosage of the magnetic photocatalyst was 2.67 g/L to treat methylene blue solution.

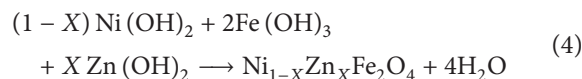
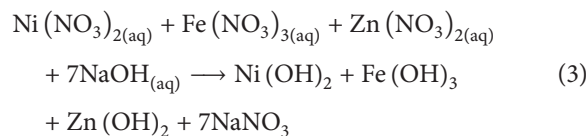
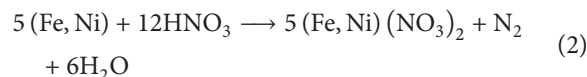
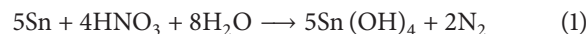
Recently we produced  $\text{MnZn}$  ferrite powders [35], which are used in power transformers and inductors, from spent alkali-manganese batteries in order to solve their heavy metal contamination problem. Comparing with  $\text{MnZn}$  ferrite,  $\text{Ni-Zn}$  ferrite is easier to be prepared. Lower temperature and no protecting atmosphere are needed during sintering. Therefore  $\text{Ni-Zn}$  ferrite was chosen to produce magnetic photocatalysts from IC lead frame scrap and waste pickling acid. Both ferrites solve the different heavy metals pollution problems and transform into useful magnetic photocatalysts.

In this research, a simple magnetic photocatalyst preparation was undertaken. First,  $\text{Ni-Zn}$  magnetic ferrite powder was prepared from IC lead frame scraps and ferrous sulfate containing spent acid solution from steel plants by coprecipitation. Then, the magnetic powder was added to a titanium sulfate solution and the hydroxides of titanium were precipitated at desired pH with urea solution. After filtration, drying, and grinding, the precipitates were sintered at  $500^\circ\text{C}$  under  $\text{N}_2$  atmosphere to form the magnetic photocatalyst,  $\text{Ni-Zn}$  ferrite/ $\text{TiO}_2$ . The degradations of simulated FBL (Everdirect Supra Turquoise Blue) dye wastewater were carried out by applying self-prepared magnetic photocatalysts under UVA irradiation. Also L-H kinetic model was studied.

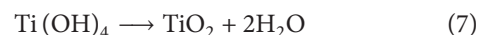
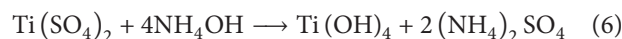
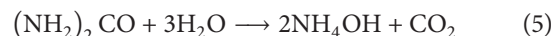
## 2. Materials and Methods

**2.1. Preparation of Magnetic Ni-Zn Ferrite Powder and Magnetic Photocatalyst.** Nitric acid was added sequentially to the small piece of lead frame scraps to dissolve nickel and iron. When hydrolysis was complete, tins were all precipitated as  $\text{Sn}(\text{OH})_4$  and the filtrate contained  $\text{Ni}^{+2}$  and  $\text{Fe}^{+2}$  ions. After detinning and according to the nickel concentration, waste acids from steel industry containing iron and reagent of zinc nitrate were added to the solution to adjust the solution composition as  $\text{Ni}_{1-X}\text{Zn}_X\text{Fe}_2\text{O}_4$ , where  $X$  is chosen as 0.5.  $\text{NaOH}$  solution is then added to adjust the solution pH value to alkali. Subsequently, all  $\text{Fe}$ ,  $\text{Ni}$ , and  $\text{Zn}$  ions in the solution were transformed into hydroxide forms and suspended in the solution. The solution was pumped with air to oxidize ferrous ion and heated for several hours. All hydroxides were reacted and precipitated from the solution as ferrite powders.  $\text{Ni-Zn}$  ferrite powders were filtered, washed, calcined, and dried. The designed composition was  $\text{Ni} : \text{Zn} : \text{Fe} = 0.5 : 0.5 : 2.0$  by moles and  $\text{Ni} : \text{Zn} : \text{Fe} = 16.9 : 18.8 : 64.3$  by weight percentages or

$\text{NiO} : \text{ZnO} : \text{Fe}_2\text{O}_3 = 9.4 : 10.2 : 80.4$  by weight. Corresponding reactions are shown in the following:



Experimental treatment with photocatalyst- $\text{TiO}_2$  alone for dye wastewater is proved to be very efficient. Besides, the secondary pollution by other advanced treatment methods can be eliminated. But there still exists the separation problem of solids ( $\text{TiO}_2$ ) and liquids (wastewater). Therefore, used in this study were titanium sulfate, urea, and  $\text{Ni-Zn}$  ferrite powder to produce modified titanium dioxide photocatalyst by coprecipitation. The ratio of  $\text{Ni-Zn}$  ferrite powder to  $\text{TiO}_2$  was 1:1 (wt%). Finally magnetic photocatalyst powder was obtained by filtration, drying, grinding, and calcination at  $500^\circ\text{C}$ . The same procedure was used for the preparation of  $\text{TiO}_2$  except the step of no addition of magnetic  $\text{Ni-Zn}$  ferrite powder. Related reactions were



The characterizations of the prepared  $\text{Ni-Zn}$  ferrite powders and modified magnetic photocatalysts,  $\text{Ni-Zn}$  ferrite/ $\text{TiO}_2$ , were investigated by ICP, XRF, XRD, SEM, SQUID, and BET measurements. TOC and ADMI values can be applied for the treatment of dye wastewater under UVA irradiation with the self-prepared  $\text{TiO}_2$  and  $\text{Ni-Zn}$  ferrite/ $\text{TiO}_2$  magnetic photocatalysts.

**2.2. Characterization.** The crystalline structures of both magnetic powder and magnetic photocatalyst were examined by XRD (X-ray diffractometer, XRD-6000, Shimadzu, Japan). Their M-H loops were measured by SQUID (superconducting quantum interference device, MPM57, Quantum Design, USA). Particle chemical compositions were analyzed by ICP (ICAP 9000, USA) and XRF (X-ray fluorescence, XEPOS/XEPO1, Spectro Co., Germany). Their microstructures were observed by SEM (scanning electron microscopy, S-3000N, Hitachi, Japan). The specific area was measured by BET surface area analyzer (Brunauer-Emmett-Teller, Model-ASAP 2012, Micromeritics, USA).

**2.3. Photocatalytic Degradation.** Photocatalytic reactions were carried out by mixing 1L of FBL dye solution and 5g of magnetic  $\text{Ni-Zn}$  ferrite/ $\text{TiO}_2$  photocatalysts inside a 2L

TABLE 1: Analysis of IC lead frame scraps by ICP.

Element	Fe	Ni	Sn
Concentration (ppm)	25325	18246	9571
Wt%	47.66%	34.33%	18.01%

TABLE 2: Analysis of filtrate after detinning by ICP.

Element	Fe	Ni
Concentration (ppm)	20364.75	14936.60
Weight %	57.69%	42.31%
Molarity (mole/L)	0.36	0.25

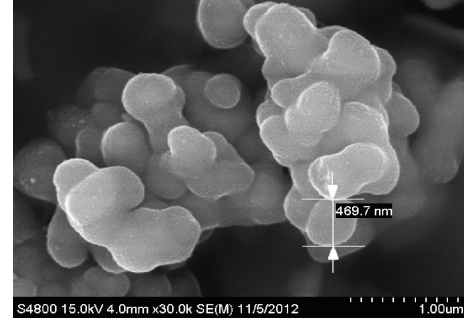
photoreactor with a Teflon agitator under UVA irradiation for 8 hrs. The structure of the FBL dye was shown in [8]. The initial dye concentrations were COD = 100, 200, 300, and 400 mg/L for each experiment. After photoreaction and filtration by 0.45  $\mu\text{m}$  MFS, TOC (total organic carbon, Model 1010, O.I. Analytical, USA) and ADMI color values (American Dye Manufacturers Institute, Model DR/4000V, HACH, USA) were measured for each sample. COD was determined by potassium dichromate titration as described in Standard Methods [36]. UVA intensities were measured by a radiometer (Lutron Co., Taiwan) and expressed as  $I_{\text{av}}$  ( $\text{mW}/\text{cm}^2$ ).

### 3. Results and Discussion

**3.1. Characterization of Magnetic Photocatalyst of Ni-Zn Ferrite/ $\text{TiO}_2$ .** The compositions of IC lead frame scraps and filtrate after detinning are shown in Tables 1 and 2, respectively.

XRF analyses of Ni-Zn ferrite powders and Ni-Zn ferrite/ $\text{TiO}_2$  are shown in Table 3. It is clear that the experimental values of magnetic powders from wastes are close to the quantity of the predetermined value. SEM micrographs suggest that particles of magnetic Ni-Zn ferrite powders agglomerate. The particle size is around 0.3  $\mu\text{m}$  by DLS (dynamic light scattering) analysis [37].  $\text{TiO}_2$  is precipitated on the surface of the secondary particle and its size is approximately 469.7 nm as shown in Figure 1. EDX diagrams of Ni-Zn ferrite powders and Ni-Zn ferrite/ $\text{TiO}_2$  photocatalyst indicate the presence of Ni, Zn, Fe, and titanium as shown in Figure 2. X-ray diffraction patterns of Ni-Zn ferrite powders and magnetic photocatalysts in Figure 3 reveal the spinel cubic ferrites and the anatase form of  $\text{TiO}_2$ . All peaks in the pattern match well with the Joint Committee of Powder Diffraction Standard (JCPDS). A small amount of hematite also exists in the specimens. The surface area of Ni-Zn ferrite powder by BET measurement is 17  $\text{m}^2/\text{g}$  and that of Ni-Zn ferrite/ $\text{TiO}_2$  rises to 61  $\text{m}^2/\text{g}$ , which shows more active sites for photoreaction.

The self-prepared  $\text{TiO}_2$  follows the same coprecipitation without the addition of Ni-Zn ferrite powder and the corresponding SEM and EDX diagrams are shown in Figures 4 and 5. The particle size is around 1  $\mu\text{m}$ –4.8  $\mu\text{m}$  and BET is 116 ( $\text{m}^2/\text{g}$ ) while BET of commercial  $\text{TiO}_2$  (7 nm) is 231 ( $\text{m}^2/\text{g}$ ).

FIGURE 1: SEM diagram of Ni-Zn ferrite/ $\text{TiO}_2$  ( $\times 30000$ ).

**3.2. Magnetic Property.** Magnetic properties of Ni-Zn ferrite powders and Ni-Zn ferrite/ $\text{TiO}_2$  are presented in Figure 6 as magnetic hysteresis loops by SQUID. The saturation magnetization ( $M_s$ ) of Ni-Zn ferrite powder and Ni-Zn ferrite/ $\text{TiO}_2$  is 64.43 and 17.05  $\text{emu}/\text{g}$  and the corresponding coercive forces ( $H_c$ ) are 6.13 and 7.66 Oe, respectively. Due to the minimal hysteresis and small  $H_c$ , the prepared magnetic materials are all soft magnetic and the magnetic photocatalysts made up from wastes can be recycled by applied magnetic field because of the magnetic property. The small coercivity of the ferrite mainly comes from the soft magnetic properties of the Ni-Zn ferrite, which has very low crystal and shape anisotropy constant, and is not due to size effect [38]. The saturation magnetization of the ferrite ( $\text{Ni}_{0.5}\text{Zn}_{0.5}\text{Fe}_2\text{O}_4$ ) prepared here is 64.43  $\text{emu}/\text{g}$ , and the literature values are about 70  $\text{emu}/\text{g}$  [39], depending on the preparation conditions. They are quite comparable.

**3.3. Photodegradation.** Photodegradations of simulated FBL dye wastewater at initial CODs of 100, 200, 300, and 400 mg/L under UVA irradiation with self-produced magnetic photocatalysts from wastes are shown in Figures 7 and 8. The degradation efficiencies increase as the pollutant concentrations decrease. For dilute pollution of FBL dye (COD = 100 ppm), TOC removal can reach 84.22% and color or ADMI removal reaches 81.68%. The photodegradations by self-prepared  $\text{TiO}_2$ , commercial  $\text{TiO}_2$ , and Ni-Zn ferrite/ $\text{TiO}_2$  are also summarized and compared in Table 4. Ni-Zn ferrite/ $\text{TiO}_2$  from wastes is very close to the commercial  $\text{TiO}_2$  (20 nm) in treatment efficiency by treating dilute simulated dye wastewater. The treatment efficiency of the self-prepared  $\text{TiO}_2$  is better than that of the commercial  $\text{TiO}_2$  (20 nm).

**3.4. Langmuir-Hinshelwood Kinetic Model (L-H Model).** L-H model can be expressed by the following equation:

$$r = -\frac{dC}{dt} = \frac{k_r KC}{1 + KC} = \frac{k_d C}{1 + KC}, \quad (8)$$

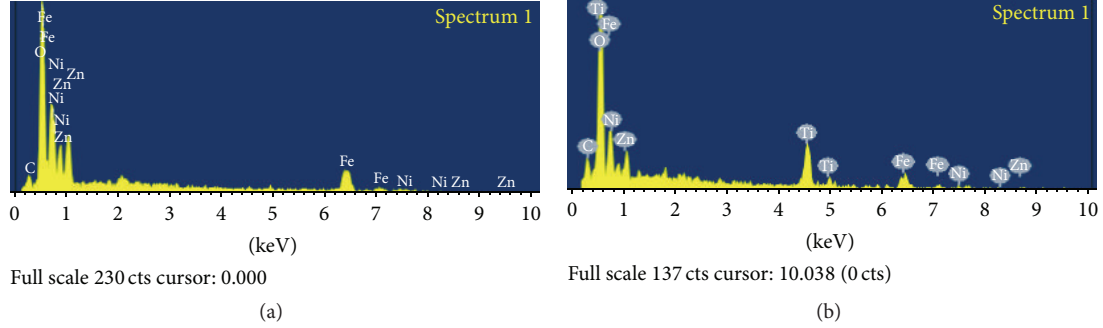
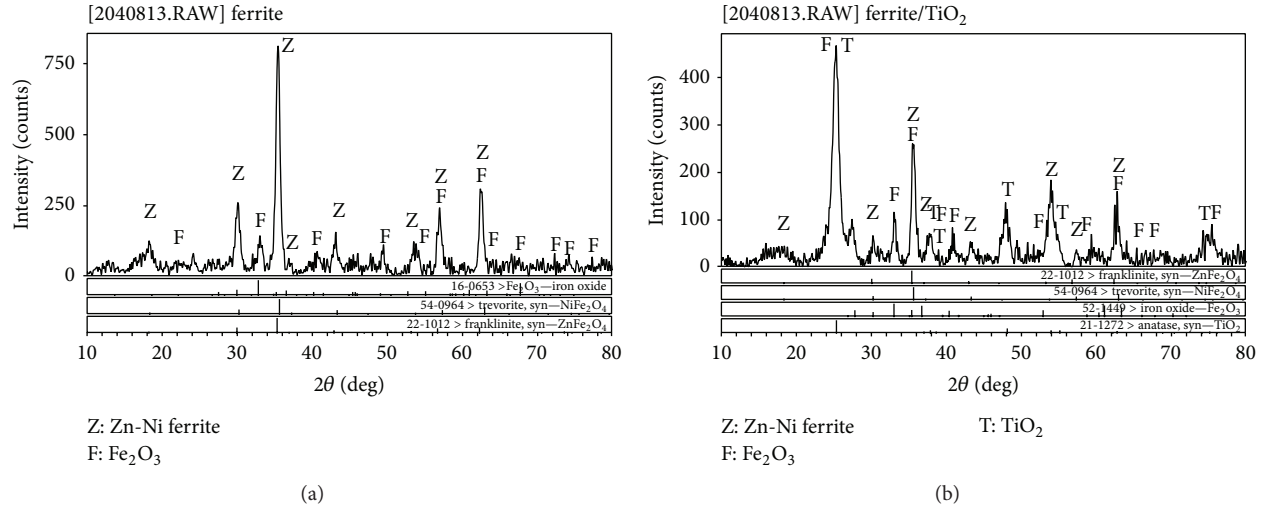
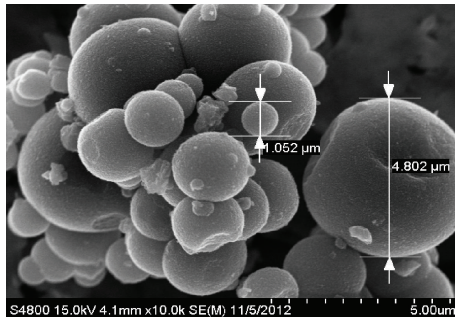
where  $k_r$  is the photocatalytic reaction constant [ $\text{mg}/(\text{L} \cdot \text{min})$ ],  $k_d$  is the apparent degradation rate constant ( $\text{min}^{-1}$ ), and  $C$  is the dye concentration, TOC ( $\text{mg}/\text{L}$ ). Combining zero-order and first-order reactions, L-H model becomes [40]

$$-\ln\left(\frac{C}{C_0}\right) + K(C_0 - C) = K_r K t. \quad (9)$$



TABLE 3: XRF analysis of magnetic materials ( $\text{Ni}_{0.5}\text{Zn}_{0.5}\text{Fe}_2\text{O}_4$  and Ni-Zn ferrite/ $\text{TiO}_2$ ).

Items	$\text{Fe}_2\text{O}_3$ (wt%)	NiO (wt%)	ZnO (wt%)	$\text{TiO}_2$ (wt%)
$\text{Ni}_{0.5}\text{Zn}_{0.5}\text{Fe}_2\text{O}_4$ (designed value)	80.4 wt%	9.4 wt%	10.20 wt%	—
$\text{Ni}_{0.5}\text{Zn}_{0.5}\text{Fe}_2\text{O}_4$ (experimental)	79.71 wt%	9.5 wt%	10.78 wt%	—
Ni-Zn ferrite/ $\text{TiO}_2$ (500°C) (experimental)	28.58 wt%	2.58 wt%	3.63 wt%	65.22 wt%

FIGURE 2: EDX of Ni-Zn ferrite powder (a) and Ni-Zn ferrite/ $\text{TiO}_2$  (b).FIGURE 3: XRD diagram of Ni-Zn ferrite powder (a) and Ni-Zn ferrite/ $\text{TiO}_2$  (500°C) (b).FIGURE 4: SEM images of self-prepared photocatalyst of  $\text{TiO}_2$  ( $\times 10000$ ).

Let  $C = 0.715C_0$ ,  $t = t_{0.715}$ ; the equation becomes

$$t_{0.715} = \frac{0.3354}{k_r K} + \frac{0.285C_0}{k_r}. \quad (10)$$

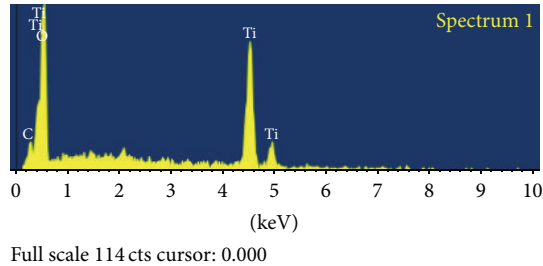
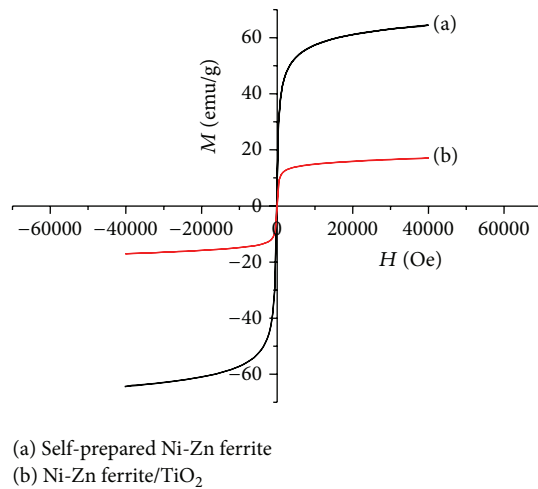
Plotting  $t_{0.715}$  against  $0.285C_0$  brings about a straight line as shown in Figure 9. From the slope and intercept, kinetic constants can be calculated.

Constants obtained from L-H model are  $k_r = 3.1614$  (mg/L min),  $k_d = 0.3212$  ( $\text{min}^{-1}$ ), and  $K = (k_d/k_r) = 0.1016$  (L/mg). The result shows that L-H kinetic model fits well for the photodegradation of FBL simulated dye wastewater with the self-prepared Ni-Zn ferrite/ $\text{TiO}_2$ .



TABLE 4: Ultimate TOC and ADMI removal % of various  $\text{TiO}_2$  (COD = 100 ppm, dosage = 5 g) under UVA irradiation ( $I_{av} = 1.324 \text{ W/cm}^2$ ).

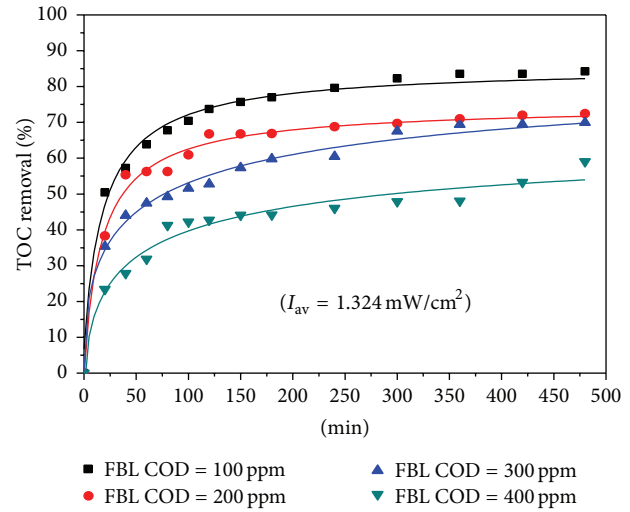
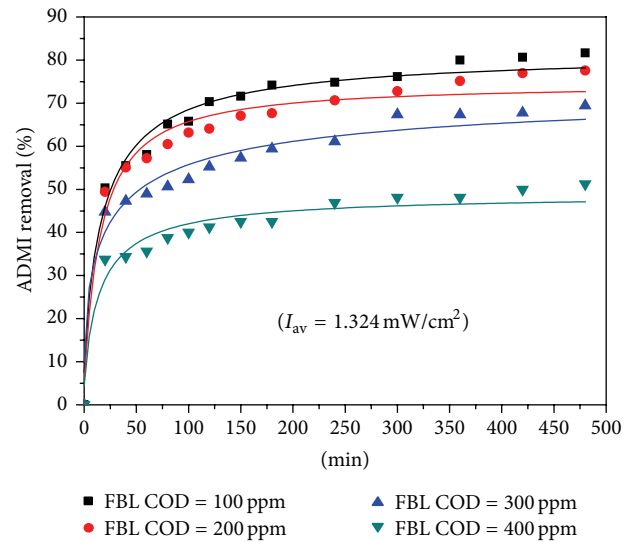
Photocatalyst	Ni-Zn ferrite/ $\text{TiO}_2$	Self-prepared $\text{TiO}_2$	Commercial $\text{TiO}_2$ (7 nm)	Commercial $\text{TiO}_2$ (20 nm)
TOC removal (%)	84.22%	91.71%	95.96%	84.40%
ADMI removal (%)	81.68%	93.04%	97.79%	87.66%

FIGURE 5: EDX of self-prepared photocatalyst of  $\text{TiO}_2$ .FIGURE 6: SQUID hysteresis loop of Ni-Zn ferrite powder and Ni-Zn ferrite/ $\text{TiO}_2$  calcined at  $500^\circ\text{C}$ .

#### 4. Conclusions

The following conclusions can be drawn:

- (1) Magnetic ferrite powder of  $\text{Ni}_{0.5}\text{Zn}_{0.5}\text{Fe}_2\text{O}_4$  was successfully prepared by coprecipitation from industrial wastes of IC lead frame and waste acids of steel industry.
- (2) Magnetic photocatalyst of Ni-Zn ferrite/ $\text{TiO}_2$  was also successfully fabricated from prepared magnetic ferrite powder,  $\text{Ti}(\text{SO}_4)_2$ , and urea by the same coprecipitation. By XRD analysis,  $\text{TiO}_2$  in magnetic photocatalyst shows the crystal structure of anatase form.
- (3) By SQUID analysis, the saturation magnetism ( $M_s$ ) of the prepared magnetic photocatalysts is 17.05 emu/g with the coercive force ( $H_c$ ) of 7.66 Oe, which proves that the magnetic photocatalyst is soft magnetic material and can be recycled by magnetic field.

FIGURE 7: TOC removal % versus time with Ni-Zn ferrite/ $\text{TiO}_2$  ( $\text{COD}|_{t=0} = 100\text{--}400 \text{ ppm}$ ) to treat FBL dye (dosage = 5 g/L;  $I_{av} = 0.1324 \text{ mW/cm}^2$ ).FIGURE 8: ADMI removal % versus time with Ni-Zn ferrite/ $\text{TiO}_2$  ( $\text{COD}|_{t=0} = 100\text{--}400 \text{ ppm}$ ) to treat FBL dye (dosage = 5 g/L;  $I_{av} = 0.1324 \text{ mW/cm}^2$ ).

- (4) The degradation of FBL dye shows that TOC and ADMI removal efficiencies are quite close for the prepared Ni-Zn ferrite/ $\text{TiO}_2$  and the commercial 20 (nm)  $\text{TiO}_2$ . The magnetic photocatalysts can solve the separation problem between wastewater and  $\text{TiO}_2$  photocatalysts by magnetic field.

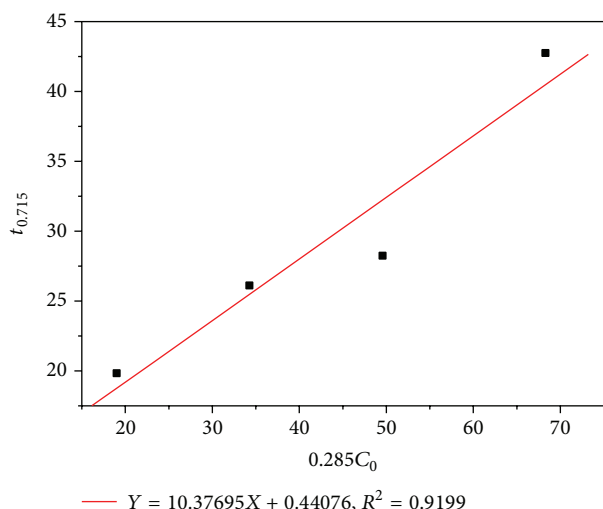


FIGURE 9: L-H kinetic model of magnetic photocatalysts of Ni-Zn ferrite/TiO<sub>2</sub>.

- (5) L-H kinetic model fits well for the self-prepared magnetic photocatalysts of Ni-Zn ferrite/TiO<sub>2</sub>, which can be used successfully in AOP.
- (6) Quite consequential is the transformation of hazardous wastes to valuable magnetic ferrite powders and magnetic photocatalysts and the processes studied not only recycle wastes to solve the global pollution problem but also tell the possibility of turning profits.

## Conflict of Interests

The authors declare that there is no conflict of interests regarding the publication of this paper.

## Acknowledgments

This project was supported by National Science Council, Taiwan, and Yeou Hung Material Technology Co., Ltd., Taiwan, under Contract no. NSC 100-2622-E-159-001-CC3. The authors express sincere gratitude for the financial support for this research.

## References

- [1] J. Pierce, "Colour in textile effluents, the origins of problems," *Journal of the Society of Dyers and Colourists*, vol. 110, pp. 131–133, 1994.
- [2] I. Arslan, I. A. Balcioglu, T. Tuhkanen, and D. Bahnemann, "H<sub>2</sub>O<sub>2</sub>/UV-C and Fe<sup>2+</sup>/H<sub>2</sub>O<sub>2</sub>/UV-C versus TiO<sub>2</sub>/UV-A treatment for reactive dye wastewater," *Journal of Environmental Engineering*, vol. 126, no. 10, pp. 903–911, 2000.
- [3] D. Tomova, V. Iliev, S. Rakovsky, M. Anachkov, A. Eliyas, and G. L. Puma, "Photocatalytic oxidation of 2,4,6-trinitrotoluene in the presence of ozone under irradiation with UV and visible light," *Journal of Photochemistry and Photobiology A: Chemistry*, vol. 231, no. 1, pp. 1–8, 2012.
- [4] Y. Nakamura, F. Kobayashi, M. Daidai, and A. Kurosumi, "Purification of seawater contaminated with undegradable aromatic ring compounds using ozonolysis followed by titanium dioxide treatment," *Marine Pollution Bulletin*, vol. 57, no. 1–5, pp. 53–58, 2008.
- [5] F. Fozzi, A. Machulek Jr., V. S. Ferreira et al., "Investigation of chlorimuron-ethyl degradation by Fenton, photo-Fenton and ozonation processes," *Chemical Engineering Journal*, vol. 210, pp. 444–450, 2012.
- [6] M. Karatas, Y. A. Argun, and M. E. Argun, "Decolorization of anthraquinonic dye, Reactive Blue 114 from synthetic wastewater by Fenton process: kinetics and thermodynamics," *Journal of Industrial and Engineering Chemistry*, vol. 18, no. 3, pp. 1058–1062, 2012.
- [7] S. Karthikeyan, A. Titus, A. Gnanamani, A. B. Mandal, and G. Sekaran, "Treatment of textile wastewater by homogeneous and heterogeneous Fenton oxidation processes," *Desalination*, vol. 281, no. 1, pp. 438–445, 2011.
- [8] R. Liu, H. M. Chiu, C.-S. Shiau, R. Y.-L. Yeh, and Y.-T. Hung, "Degradation and sludge production of textile dyes by Fenton and photo-Fenton processes," *Dyes and Pigments*, vol. 73, no. 1, pp. 1–6, 2007.
- [9] S. S. Abu Amr and H. A. Aziz, "New treatment of stabilized leachate by ozone/Fenton in the advanced oxidation process," *Waste Management*, vol. 32, no. 9, pp. 1693–1698, 2012.
- [10] M. N. Chong, B. Jin, C. W. K. Chow, and C. Saint, "Recent developments in photocatalytic water treatment technology: a review," *Water Research*, vol. 44, no. 10, pp. 2997–3027, 2010.
- [11] S. Bagwasi, B. Tian, J. Zhang, and M. Nasir, "Synthesis, characterization and application of bismuth and boron Co-doped TiO<sub>2</sub>: a visible light active photocatalyst," *Chemical Engineering Journal*, vol. 217, pp. 108–118, 2013.
- [12] M. Khraisheh, L. Wu, A. H. Al-Muhtaseb, A. B. Albadarin, and G. M. Walker, "Phenol degradation by powdered metal ion modified titanium dioxide photocatalysts," *Chemical Engineering Journal*, vol. 213, pp. 125–134, 2012.
- [13] R. Liu, H. S. Wu, R. Yeh, C. Y. Lee, and Y. Hung, "Synthesis and bactericidal ability of TiO<sub>2</sub> and Ag-TiO<sub>2</sub> prepared by coprecipitation method," *International Journal of Photoenergy*, vol. 2012, Article ID 640487, 7 pages, 2012.
- [14] A. Charanpahari, S. S. Umare, S. P. Gokhale, V. Sudarsan, B. Sreedhar, and R. Sasikala, "Enhanced photocatalytic activity of multi-doped TiO<sub>2</sub> for the degradation of methyl orange," *Applied Catalysis A: General*, vol. 443–444, pp. 96–102, 2012.
- [15] Z.-D. Meng, F.-J. Zhang, L. Zhu et al., "Synthesis and characterization of M-fullerene/TiO<sub>2</sub> photocatalysts designed for degradation azo dye," *Materials Science and Engineering C*, vol. 32, no. 8, pp. 2175–2182, 2012.
- [16] S. Yamazaki, Y. Fujiwara, S. Yabuno, K. Adachi, and K. Honda, "Synthesis of porous platinum-ion-doped titanium dioxide and the photocatalytic degradation of 4-chlorophenol under visible light irradiation," *Applied Catalysis B: Environmental*, vol. 121–122, pp. 148–153, 2012.
- [17] B. Neppolian, A. Bruno, C. L. Bianchi, and M. Ashokkumar, "Graphene oxide based Pt-TiO<sub>2</sub> photocatalyst: ultrasound assisted synthesis, characterization and catalytic efficiency," *Ultrasonics Sonochemistry*, vol. 19, no. 1, pp. 9–15, 2012.
- [18] S. R. Shirsath, D. V. Pinjari, P. R. Gogate, S. H. Sonawane, and A. B. Pandit, "Ultrasound assisted synthesis of doped TiO<sub>2</sub> nanoparticles: characterization and comparison of effectiveness for photocatalytic oxidation of dyestuff effluent," *Ultrasonics Sonochemistry*, vol. 20, no. 1, pp. 277–286, 2013.

- [19] S. Chakma and V. S. Moholkar, "Physical mechanism of sonofenton process," *AIChE Journal*, vol. 59, no. 11, pp. 4303–4313, 2013.
- [20] S. Chakma and V. S. Moholkar, "Investigations in synergism of hybrid advanced oxidation processes with combinations of sonolysis + fenton process + UV for degradation of bisphenol A," *Industrial and Engineering Chemistry Research*, vol. 53, no. 16, pp. 6855–6865, 2014.
- [21] J. Hu, M. Yan, and W. Luo, "Preparation of high-permeability NiZn ferrites at low sintering temperatures," *Physica B: Condensed Matter*, vol. 368, no. 1–4, pp. 251–260, 2005.
- [22] H. Su, H. Zhang, X. Tang, Y. Jing, and Y. Liu, "Effects of composition and sintering temperature on properties of NiZn and NiCuZn ferrites," *Journal of Magnetism and Magnetic Materials*, vol. 310, no. 1, pp. 17–21, 2007.
- [23] X. He, Q. Zhang, and Z. Ling, "Kinetics and magnetic properties of sol-gel derived NiZn ferrite-SiO<sub>2</sub> composites," *Materials Letters*, vol. 57, no. 20, pp. 3031–3036, 2003.
- [24] H. H. He, G. S. Song, and J. H. Zhu, "Non-stoichiometric NiZn ferrite by sol-gel processing," *Materials Letters*, vol. 59, pp. 1941–1944, 2005.
- [25] W.-C. Hsu, S. C. Chen, P. C. Kuo, C. T. Lie, and W. S. Tsai, "Preparation of NiCuZn ferrite nanoparticles from chemical co-precipitation method and the magnetic properties after sintering," *Materials Science and Engineering B*, vol. 111, no. 2–3, pp. 142–149, 2004.
- [26] K. H. Wu, Y. M. Shin, C. C. Yang, G. P. Wang, and D. N. Horng, "Preparation and characterization of bamboo charcoal/Ni<sub>0.5</sub>Zn<sub>0.5</sub>Fe<sub>2</sub>O<sub>4</sub> composite with core-shell structure," *Materials Letters*, vol. 60, no. 21–22, pp. 2707–2710, 2006.
- [27] S. Verma, P. A. Joy, Y. B. Kholam, H. S. Potdar, and S. B. Deshpande, "Synthesis of nanosized MgFe<sub>2</sub>O<sub>4</sub> powders by microwave hydrothermal method," *Materials Letters*, vol. 58, no. 6, pp. 1092–1095, 2004.
- [28] A. Verma, T. C. Goel, R. G. Mendiratta, and R. G. Gupta, "High-resistivity nickel-zinc ferrites by the citrate precursor method," *Journal of Magnetism and Magnetic Materials*, vol. 192, no. 2, pp. 271–276, 1999.
- [29] S. Deka and P. A. Joy, "Characterization of nanosized NiZn ferrite powders synthesized by an autocombustion method," *Materials Chemistry and Physics*, vol. 100, no. 1, pp. 98–101, 2006.
- [30] K. H. Wu, Y. C. Chang, and G. P. Wang, "Preparation of NiZn ferrite/SiO<sub>2</sub> nanocomposite powders by sol-gel autocombustion method," *Journal of Magnetism and Magnetic Materials*, vol. 269, no. 2, pp. 150–155, 2004.
- [31] P. P. Goswami, H. A. Choudhury, S. Chakma, and V. S. Moholkar, "Sonochemical synthesis and characterization of manganese ferrite nanoparticles," *Industrial & Engineering Chemistry Research*, vol. 52, no. 50, pp. 17848–17855, 2013.
- [32] F. Chen and J. Zhao, "Preparation and photocatalytic properties of a novel kind of loaded photocatalyst of TiO<sub>2</sub>/SiO<sub>2</sub>/γ-Fe<sub>2</sub>O<sub>3</sub>," *Catalysis Letters*, vol. 58, no. 4, pp. 246–247, 1999.
- [33] Y. Gao, B. Chen, H. Li, and Y. Ma, "Preparation and characterization of a magnetically separated photocatalyst and its catalytic properties," *Materials Chemistry and Physics*, vol. 80, no. 1, pp. 348–355, 2003.
- [34] Y.-P. Fu, W.-K. Chang, H.-C. Wang, C.-W. Liu, and C.-H. Lin, "Synthesis and characterization of anatase TiO<sub>2</sub> nanolayer coating on Ni-Cu-Zn ferrite powders for magnetic photocatalyst," *Journal of Materials Research*, vol. 25, no. 1, pp. 134–140, 2010.
- [35] R. Liu, C. F. Wu, and M. D. Ger, "Degradation of FBL dye wastewater by magnetic photocatalysts from scraps," *Journal of Nanomaterials*, vol. 2015, Article ID 651021, 9 pages, 2015.
- [36] APHA, *Standard Methods for the Examination of Water and Wastewater*, American Public Health Association, American Water Works Association, Water Environment Federation, Washington, DC, USA, 22nd edition, 2012.
- [37] C. F. Wu, *Preparation, characterization and application of Mn-Zn ferrite powders and magnetic titanium dioxide from used dry batteries and spent steel pickling liquids [M.S. thesis]*, Department of Chemical and Materials Engineering, Minghsin University of Science and Technology, Hsinchu, Taiwan, 2012.
- [38] B. D. Cullity and C. D. Graham, *Introduction to Magnetic Materials*, John Wiley & Sons, 2009.
- [39] A. Goldman, *Modern Ferrite Technology*, Van Nostrand Reinhold, 1990.
- [40] I. A. Alaton and I. A. Balcioglu, "Photochemical and heterogeneous photocatalytic degradation of waste vinylsulphone dyes: a case study with hydrolyzed Reactive Black 5," *Journal of Photochemistry and Photobiology A: Chemistry*, vol. 141, no. 2–3, pp. 247–254, 2001.

## Research Article

# TiO<sub>2</sub> Nanocatalysts Supported on a Hybrid Carbon-Covered Alumina Support: Comparison between Visible Light and UV Light Degradation of Rhodamine B

Mphilisi M. Mahlambi,<sup>1</sup> Ajay K. Mishra,<sup>2</sup> Shivani B. Mishra,<sup>1</sup> Rui W. Krause,<sup>1</sup> Bhekie B. Mamba,<sup>2</sup> and Ashok M. Raichur<sup>1,3</sup>

<sup>1</sup>Department of Applied Chemistry, University of Johannesburg, P.O. Box 17011, Doornfontein 2028, South Africa

<sup>2</sup>Nanotechnology and Water Sustainable Unit, College of Science and Technology, University of South Africa, Florida Campus, Johannesburg 1710, South Africa

<sup>3</sup>Department of Materials Engineering, Indian Institute of Science, Bangalore 560012, India

Correspondence should be addressed to Mphilisi M. Mahlambi; mmahlambi@yahoo.co.uk

Received 28 January 2015; Accepted 24 March 2015

Academic Editor: Lin-Hua Xu

Copyright © 2015 Mphilisi M. Mahlambi et al. This is an open access article distributed under the Creative Commons Attribution License, which permits unrestricted use, distribution, and reproduction in any medium, provided the original work is properly cited.

Titania nanoparticles were successfully supported on carbon-covered alumina (CCA) supports via the impregnation method to form carbon-covered alumina titania (CCA/TiO<sub>2</sub>). The CCA supports were synthesised through an equilibrium adsorption of toluene 2,4-diisocyanate where the N=C=O irreversibly adsorbs on the alumina and pyrolysis at 700°C affords CCA supports. These CCA/TiO<sub>2</sub> nanocatalysts were tested for their photocatalytic activity both under UV and visible light using Rhodamine B as a model pollutant. The reaction rate constant of the CCA/TiO<sub>2</sub> was found to be higher than that of unsupported titania and the reaction kinetics were found to follow an apparent first-order rate law. The CCA/TiO<sub>2</sub> nanocatalysts had a much larger surface area than the unsupported titania and they exhibited overall higher photodegradation efficiency under both UV and visible light than unsupported TiO<sub>2</sub>.

## 1. Introduction

The ability of photocatalysts to mineralise most organic pollutants to water and carbon dioxide as a low-cost advanced oxidation technology (AOT) has attracted interest for decades [1–4]. TiO<sub>2</sub> induced photocatalysis for the treatment of contaminated air and water is a well-established AOT technique [5–8] because of its high photoactivity, chemical and biological inertness, and commercial availability [1, 5, 9, 10]. The titania semiconductor absorbs a photon ( $h\nu$ ) with energy equal to or higher than its band gap of 3.2 eV resulting in the excitation of electrons from the valence band into the conduction band, leaving excited holes behind in the conduction band and creating positive holes in the valence band [6, 11–16]. Generally the hole oxidises water or OH groups in the titania lattice to produce  $\cdot$ OH radicals which initiate the oxidation of the organics.

However, titania has a large band gap (3.2 eV) that can only absorb about 2% to 3% visible light; thus a number of ways have been attempted to shift its band gap to the visible-light region. The modifications towards visible-light degradation by TiO<sub>2</sub> include metal ion doping [5, 17–21], anion doping [22–24], binary oxides [25, 26], and dye sensitizers [27, 28]. Another phenomenon that has been studied to enhance visible-light photoreactivity includes size [29, 30] and shape tailoring [31–34].

Carbon in its various forms has been used to synthesise visible-light active TiO<sub>2</sub>. These include carbon-covered titania [1], titania mounted on graphite [35], and nanotubes [36, 37] as well as activated carbon [8, 16, 38]. The advantage of carbon-titania composites is that the carbon does not only expand the absorption band to include visible light, it also suppresses phase transformations even at higher temperatures. Lin and coworkers [1] have reported on the successful



synthesis of carbon-covered titania through pyrolysis of sucrose over titania and its superior visible-light activity.

In this work we report on the photocatalytic activity of carbon-covered alumina supported titania in the degradation of Rhodamine B. Supports play an important role in determining the nature and extent of the catalytic activity of a catalyst. Carbon-covered alumina supported catalysts have been mostly used as supports for hydrotreating catalysts [39, 40] and ammonia synthesis [41, 42] but not for environmental remediation. The CCA/TiO<sub>2</sub> nanocatalysts show enhanced visible-light degradation (higher activity) than under UV light illumination of Rhodamine B. It is worth mentioning that the presence of carbon on the CCA support greatly increases the surface area of the CCA/TiO<sub>2</sub> catalysts and shifts the absorption edge of titania to the visible-light region resulting in visible-light degradation of Rhodamine B.

## 2. Experimental

**2.1. Materials and Reagents.** The materials used in this research study were purchased from suppliers and used without further purification. Only AR grade *n*-propanol which was obtained from SD's Fine Chemicals (Pty) Ltd was distilled before usage.

**2.1.1. Synthesis of TiO<sub>2</sub>.** Anatase-rich titania nanocatalysts were synthesised through the hydrolysis of TTIP through an esterification reaction between formic acid and propanol [10]. This method is reported in our previous works [43–45].

**2.1.2. Synthesis of Carbon Covered Alumina Supports.** CCA supports were synthesised by modification of an equilibrium adsorption method [46]. The detailed procedure for the modified procedure is reported elsewhere [45].

**2.1.3. Impregnation Experiments.** The TiO<sub>2</sub> catalysts were then supported on the CCA catalysts using a simple impregnation method. This impregnation technique is described in detail in our previous research work [45]. To study the catalytic efficiency of the supported CCA catalysts, photocatalytic degradation studies were done under visible light.

**2.1.4. Photocatalytic Degradation Experiments.** To study the degradation and the kinetics of Rhodamine B by the titania photocatalysts, a Newport 9600 Full Spectrum Solar Simulator equipped with 150 W ozone-free xenon lamp was used, which produces a collimated beam of 33 mm diameter, an equivalent of 1.3 suns. For the purposes of this study, the distance between the solar simulator and the experimental setup was set such that the beam power was equivalent to 1 sun. UV light filter GG450 was used to ensure that the photocatalytic degradation experienced is only due to visible light irradiation. The photocatalytic activity of these nanophotocatalysts was studied using 100 mL (10 mg·L<sup>-1</sup>) Rhodamine B. The visible light (solar) irradiation lamp was placed at about a 10 cm distance away from the reactant solution. The CCA-supported titania nanoparticles (100 mg nanoparticles per 100 mL of 10 mg·L<sup>-1</sup> dye) were used in suspension to determine the photoactivity of the nanoparticles. The solution was

stirred with a magnetic stirrer for 1 h prior to irradiation with the solar light to establish an adsorption-desorption equilibrium between the dye and the catalyst surface. Aliquots of 2 mL were extracted from the reaction chamber at 30 min intervals to study the extent of the degradation. The entire photo-reactor setup was set inside a 1 m × 70 cm wooden box and the experiment was carried in a dark room. The setup was the same for the free (unsupported) titania nanocatalysts and a UV light source was used for UV light degradation experiments.

Prior to the photodegradation experiments, Rhodamine B solution (without catalyst) was irradiated with the solar light (photolysis) for a maximum period of 5 h to establish whether there was any degradation due to the solar light alone. A U Shimadzu UV-2450 UV-Vis spectrophotometer was used to determine the extent of photodegradation of Rhodamine B. After the irradiation process had been established, the kinetics of the photodegradation was studied. The apparent rate constant allows for the determination of photocatalytic activity independent of the previous adsorption period and the concentration of the Rhodamine B remaining in the solution [47]. The apparent first-order kinetic equation  $-\ln(C_t/C_0) = K_{app}t$ , where  $K_{app}$  is the apparent rate constant,  $C_t$  is the solution phase concentration, and  $C_0$  is the concentration at  $t = 0$ , was used to fit the experimental data [48].

## 2.2. Characterization

**2.2.1. UV-Vis Diffuse Reflectance Spectra.** A Shimadzu UV-2450 UV-Vis spectrophotometer was used to record the UV-Vis diffuse reflectance spectra of the CCA-supported and free TiO<sub>2</sub> nanocatalysts using BaSO<sub>4</sub> as a reference sample. These were recorded in the range of  $\lambda = 300$  nm to 800 nm, at room temperature and in air. This was done to ascertain the effect of the support on the band gap ( $E_g$ ) of the titania nanoparticles. The equation  $E_g = hc/\lambda$  was used where  $E_g$  is the band gap,  $h$  is Planck's constant,  $c$  is the speed of light (m·s<sup>-1</sup>), and  $\lambda$  is the wavelength (nm). A tangent of the plot of  $h\nu$  versus  $(\alpha h\nu)^2$  gives an estimate of the band gap where  $\alpha$  is the absorbance and  $\nu$  is the wave number.

**2.2.2. BET Surface Area Studies.** The surface area ( $S_{BET}$ ), pore volume, and pore-size distributions of the synthesised CCA-supported catalysts were studied using a Micromeritics ASAP 2020 Surface Area and Porosity Analyzer. The samples were degassed in nitrogen under vacuum for 24 h at 200°C prior to determination of the surface area. Surface area is an important parameter when studying the catalytic efficiency of the nanocatalysts embedded on CCA supports (CCA/TiO<sub>2</sub>) since a high surface area means more active sites for extensive catalysis.

**2.2.3. SEM and TEM Studies.** A JEOL J2100 F transmission electron microscope (TEM) was used to study the microstructure of the nanocatalysts. The sample powders were dispersed in ethanol and sonicated for 10 min before analysis. A drop of the suspension was then placed on a carbon coated copper grid and dried in air prior to visualisation. To analyse and visualise the surface morphology of the nanocatalysts,



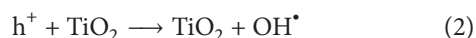
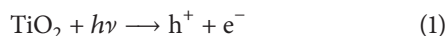
TABLE 1: Comparison of photodegradation efficiencies of Rhodamine B by free and CCA/TiO<sub>2</sub> under UV and visible-light illumination.

Light source	Catalyst	Degradation efficiency (%)	Time taken (min)
Visible light	Photolysis (no catalyst)	4	270
Visible light	Unsupported TiO <sub>2</sub>	20	270
Visible light	CCA-supported TiO <sub>2</sub>	100	180
UV-visible light	Unsupported TiO <sub>2</sub>	100	270
UV-visible light	CCA-supported TiO <sub>2</sub>	100	240

a quanta FEI-SIRION scanning electron microscope (SEM) was used. For SEM analysis, the powder samples were placed on a carbon tape and analysed without gold coating.

### 3. Results and Discussions

**3.1. Degradation Process.** The photodegradation process of Rhodamine B can be summarised in (1) to (3) when disregarding the role of the electrons ( $e^-$ ) which is in the oxidation of metal ions. The titania nanocatalysts absorb a photon ( $h\nu$ ) resulting in the excitation of an electron ( $e^-$ ) from the valence band (VB) to the conduction band (CB) leaving an electron vacancy or a hole ( $h^+$ ) in the valence band (1). The holes then migrate to the surface of the titania where they react with surface hydroxyl groups in the TiO<sub>2</sub> lattice or water to produce hydroxyl radicals (2):



The hydroxyl radicals then react with the Rhodamine B producing intermediates, carbon dioxide, water, and inorganic ions (3).

**3.2. Degradation Studies.** Figure 1 shows the UV spectra of Rhodamine B with its peak maximum at 554 nm. It also shows the disappearance of the peak after illumination with either UV or visible light in the presence of different titania catalysts. For the photodegradation studies, the dye was illuminated with visible light in the absence of the catalyst to determine the extent of degradation under visible light since Rhodamine B has been reported to absorb light which is in the range of 400 nm to 600 nm [26, 28]. The results obtained showed that photolysis, on average, degraded about 4% of the Rhodamine B. The mixture was stirred in the dark for an hour to reach equilibrium between the catalyst and the dye before illumination with either the UV or visible light and the concentration was monitored. It was found that there was only about 2% adsorption of the dye on the catalysts when equilibrium was reached.

**3.2.1. UV Light Degradation of Rhodamine B.** Photodegradation of Rhodamine B was tested using the different catalysts under UV light irradiation. As shown in Table 1, both the CCA/TiO<sub>2</sub> and the free titania nanocatalysts achieved complete degradation after 270 min. The linear transform curve of the photodegradation of Rhodamine B (Figure 2) shows that

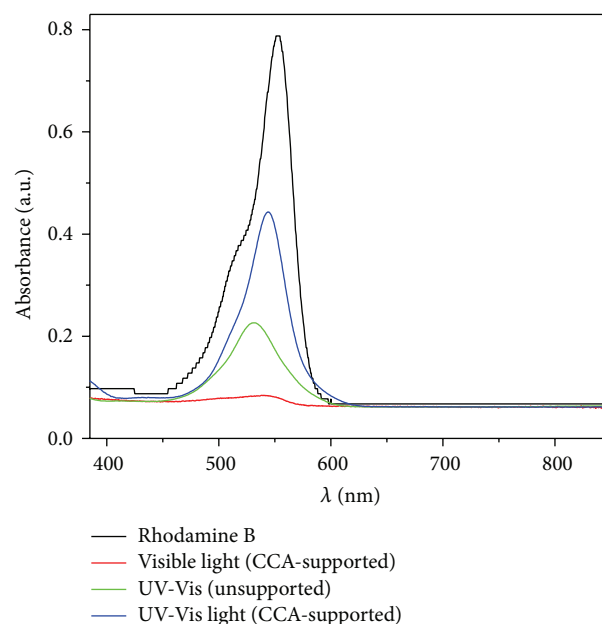


FIGURE 1: Graph showing absorbance of Rhodamine B before and after illumination with visible light.

the CCA/TiO<sub>2</sub> nanocatalysts had an apparent rate constant ( $K_{app}$ ) of  $0.0215 \text{ min}^{-1}$  and the free TiO<sub>2</sub> nanocatalysts had a  $K_{app}$  value of  $0.0167 \text{ min}^{-1}$ . From these results the CCA/TiO<sub>2</sub> nanocatalysts show a higher reaction rate than the free anatase titania.

**3.2.2. Visible Light Degradation of Rhodamine B.** The degradation of Rhodamine B was also tested under visible light illumination. The results obtained (Table 1) show that CCA/TiO<sub>2</sub> nanocatalysts were photocatalytically active under visible light. While the unsupported titania could only degrade about 20% of Rhodamine B in 270 min with an apparent rate constant of  $0.000832 \text{ min}^{-1}$ , the CCA/TiO<sub>2</sub> nanocatalysts completely degraded the dye within 180 min and a high apparent rate of  $0.0294 \text{ min}^{-1}$ .

From the results obtained, the CCA/TiO<sub>2</sub> nanocatalysts exhibited superior photocatalytic activity compared to the unsupported titania both under UV and visible-light illumination. This could be a result of the modification of the surface area of the titania catalysts by the carbon-covered alumina supports. Also, this showed that CCAs are good supports for titania nanocatalysts as they result in an enhanced photocatalytic activity. The presence of carbon could be

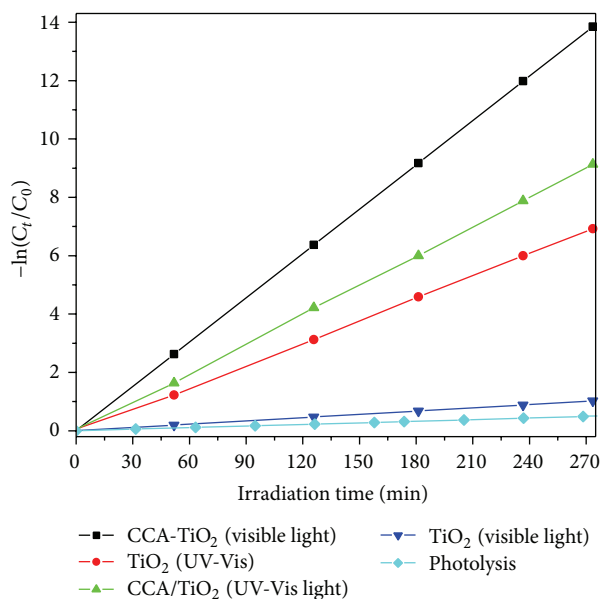


FIGURE 2: Linear transform graph of degradation of Rhodamine B by free titania CCA/TiO<sub>2</sub> under UV and visible-light illumination.

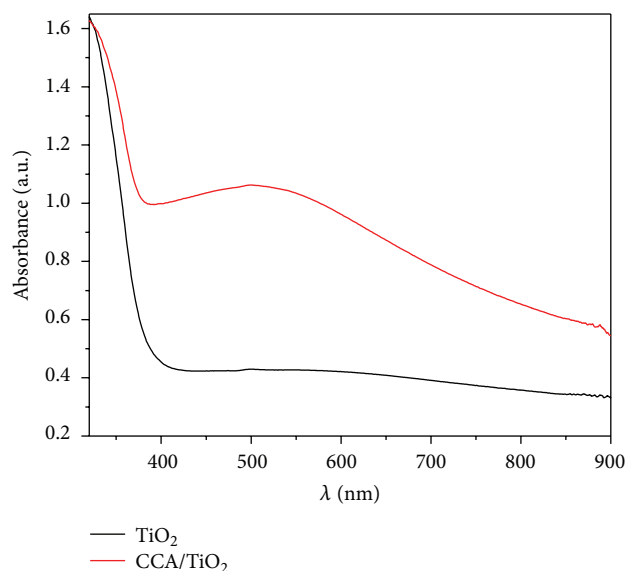


FIGURE 3: UV-Vis diffuse spectra of TiO<sub>2</sub> and CCA/TiO<sub>2</sub> nanocatalysts.

responsible for perturbing the transmission of both UV and visible light to the surface of titania resulting in an increased photocatalytic activity of titania. Furthermore, the presence of aluminium on the support system could prove efficient in that it could act as an electron trapper and hence prohibit or reduce the possibility of electron-hole recombination thus resulting in an enhanced photocatalytic activity.

**3.3. UV-Diffuse Spectra and Band-Gap Studies.** To further study the origin of this enhanced photocatalytic activity, the UV-diffuse reflectance spectra (Figure 3) of the CCA/TiO<sub>2</sub>

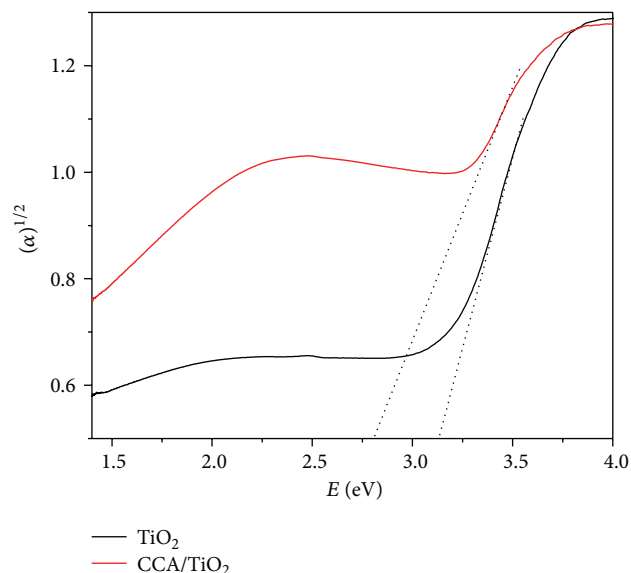


FIGURE 4: Band-gap studies of TiO<sub>2</sub> and CCA/TiO<sub>2</sub> nanocatalysts.

and free titania were studied. The CCA/TiO<sub>2</sub> spectrum showed a significant red shift of the band edge from 380 nm to 416 nm, that is, in the visible range. This shift in the absorption edge is responsible for the visible-light photocatalytic activity of the CCA-supported titania.

The data obtained from the UV-Vis diffuse spectra of the CCA/TiO<sub>2</sub> and free titania were used to indirectly measure the band gap (Figure 4). The band gap of the free titania was found to be 3.19 eV which is close to the known literature value of free anatase titania nanocatalysts. The CCA-supported catalysts showed a significant decrease in the band gap from 3.19 eV to 2.82 eV. The decrease by 0.37 eV is much higher than the decrease of 0.14 eV reported for carbon-doped titania [1]. The presence of alumina might have contributed to the decrease in the band gap and subsequently enhanced the photocatalytic activity.

**3.4. BET Surface Area and Pore-Size Distribution Measurements.** The nitrogen adsorption-desorption isotherms were measured in order to understand the influence of supporting titania nanocatalysts on the CCA (Figures 5 and 6). Figure 5 shows the adsorption-desorption isotherm of pure titania and the insert graph shows the pore-size distribution graph of the titania. Figure 6 shows the adsorption-desorption isotherm of the CCA/TiO<sub>2</sub> with the insert showing the pore-size distribution graph. Evidence of the occurrence of open pores in the CCA/TiO<sub>2</sub> is shown by the presence of the hysteresis loop. The narrow hysteresis loop observed on the titania graph is an indication of a uniform pore-size distribution of the nanoparticles. The CCA/TiO<sub>2</sub> graph on the other hand shows a wider hysteresis loop, an indication of a wider range of pore distribution, that is, the presence of titania, carbon, and alumina pores which play an important role in the observed enhancement of the photodegradation of Rhodamine B.

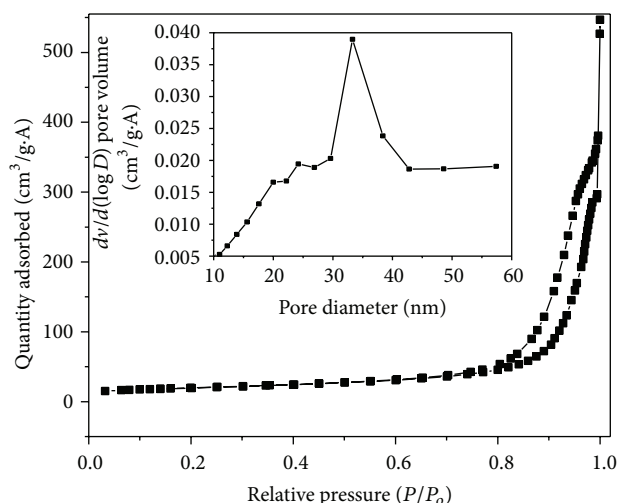


FIGURE 5: Nitrogen adsorption-desorption isotherm of titania nanocatalysts.

The surface properties of CCA/TiO<sub>2</sub> and free titania, that is, specific surface area, pore volume, pore size, and pore-size distribution, were analysed according to the BJH method (insert graphs in Figures 5 and 6). The free titania nanoparticles had a surface area of 69.34 m<sup>2</sup>·g<sup>-1</sup> while the CCA/TiO<sub>2</sub> nanocatalysts had a surface area of 149 m<sup>2</sup>·g<sup>-1</sup>. This is an increase of about twice the initial surface area and this is a result of the creation of new pore structures after the modification of the CCA support surface. A decrease in the mean diameter of the pores was also observed, from 35 nm to 5.41 nm for the titania and the CCA/TiO<sub>2</sub>, respectively. This is an indication that the titania occupied the inner pores of the carbon-covered alumina supports, hence the decrease. The increase in the surface area and decrease in particle size therefore played an important role in the enhanced photocatalytic degradation of Rhodamine B shown by the CCA-supported catalysts.

**3.5. SEM and TEM Studies.** The high surface area of the CCA/TiO<sub>2</sub> nanoparticles observed in the BET surface area analysis was further confirmed by the SEM images (Figure 7). From the SEM micrographs the titania nanoparticles appear evenly distributed on the surface of the carbon-covered alumina supports. The even distribution of the titania nanocatalysts on the surface of the CCA support is a result of the titania nanocatalysts occupying the inner pores of the CCA supports. This distribution of the TiO<sub>2</sub> nanoparticles therefore results in the increased surface area exhibited by the CCA/TiO<sub>2</sub> nanocatalysts over the unsupported TiO<sub>2</sub> nanocatalysts.

The TEM images (Figure 8) of the CCA/TiO<sub>2</sub> nanocatalysts showed that the nanocatalysts were not only successfully embedded on the pores of the CCA supports but were also evenly distributed on the CCA surface. From these TEM images it can be seen that the TiO<sub>2</sub> nanocatalysts (Figure 8(a)) did not lose their crystallinity upon embedding on the CCA supports (Figure 8(b)). This was further confirmed by the electron diffraction (ED) patterns. The ED patterns of

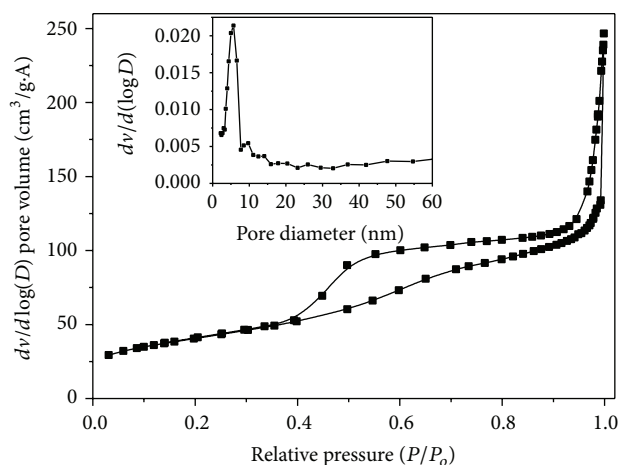


FIGURE 6: Nitrogen adsorption-desorption isotherm of the CCA/TiO<sub>2</sub> nanocatalysts.

the CCA/TiO<sub>2</sub> nanocatalysts show that embedding the TiO<sub>2</sub> nanocatalysts on the CCA supports did not destroy their crystal lattice (Figure 8(a)). These ED patterns are characteristic of the 101 plane of the TiO<sub>2</sub> nanoparticles (Figure 8).

Both the SEM and the TEM studies revealed that the physical morphology of the CCA-supported titania nanocatalysts played a major role in the photocatalytic degradation properties of these nanocatalysts. The SEM studies revealed that the CCA/TiO<sub>2</sub> nanoparticles had a high surface area while the TEM studies showed that the nanoparticles were evenly distributed on the surface of the CCA supports and that they still exhibited high crystallinity (ED patterns). Therefore the increased surface area and the preserved crystallinity are responsible for the high photocatalytic activity exhibited by the CCA/TiO<sub>2</sub> nanocatalysts.

The elemental composition of the synthesized catalyst and supports was identified using the EDS spectroscopy and this is shown in Figure 9. The EDS spectrum of the CCA-TiO<sub>2</sub> nanocatalysts showed the presence of Al, O, C, and Ti elements. From the EDS we were able to confirm not only the successful incorporation of carbon on the surface of alumina but also the successful impregnation of the CCA with the TiO<sub>2</sub> nanocatalysts.

## 4. Conclusions

The CCA-supported titania nanocatalysts demonstrated superior photocatalytic activity compared to the free titania catalysts both under UV and visible-light illumination. The presence of the CCA supports resulted in an increased surface area and decreased the rate of electron-hole recombination (electron scavengers) hence resulting in an increased photocatalytic activity. Also, embedding the titania catalysts on the CCA supports resulted in a sharp decrease in the band gap of titania thus shifting the absorption edge of titania towards the visible-light region resulting in an enhanced visible-light photoactivity of the CCA-supported catalysts.



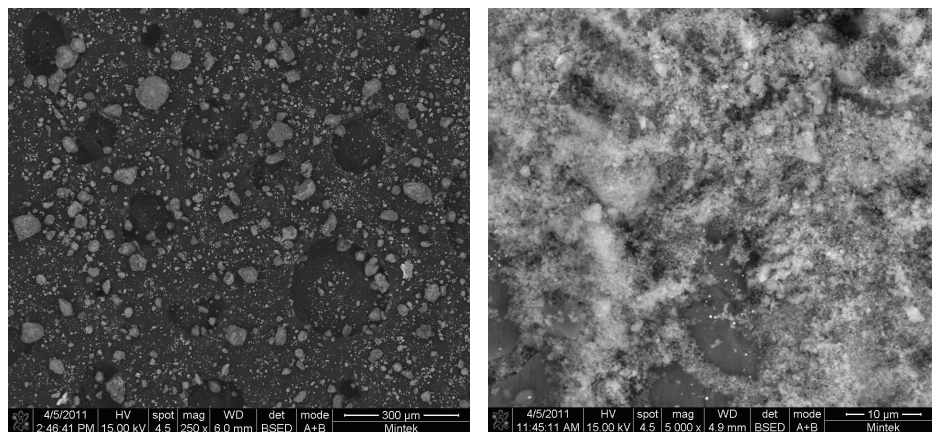


FIGURE 7: SEM images of the CCA/TiO<sub>2</sub> nanocatalysts.

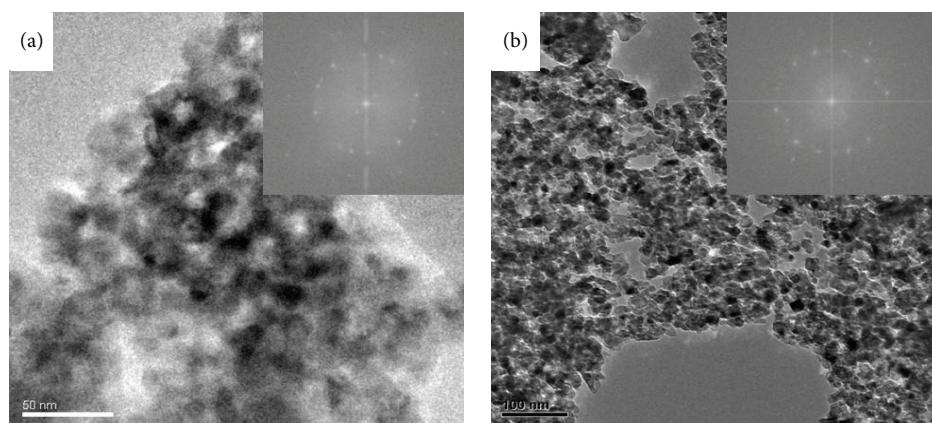


FIGURE 8: TEM images of the (a) TiO<sub>2</sub> and (b) CCA/TiO<sub>2</sub> nanocatalysts.

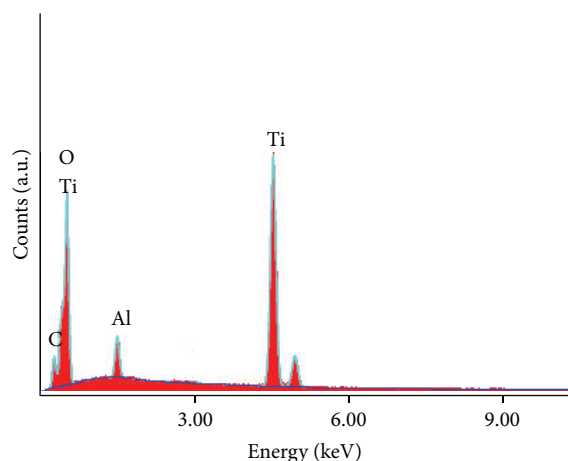


FIGURE 9: EDS spectrum of the CCA/TiO<sub>2</sub> nanocatalysts.

Furthermore, the CCA-TiO<sub>2</sub> nanocatalysts had a high surface area, were evenly distributed on CCA support surface, and were highly crystalline thus making the CCA supports a superior support for titania nanocatalysts for environmental pollution remediation.

## Conflict of Interests

The authors declare that there is no conflict of interests regarding the publication of this paper.

## Acknowledgments

The authors are grateful to the University of Johannesburg for financial support and the Indian Institute of Science, Bangalore, India, for providing the infrastructure to carry out some of this research work.

## References

- [1] L. Lin, W. Lin, Y. X. Zhu et al., "Uniform carbon-covered titania and its photocatalytic property," *Journal of Molecular Catalysis A: Chemical*, vol. 236, no. 1-2, pp. 46–53, 2005.
- [2] K. Yu, S. Yang, H. He, C. Sun, C. Gu, and Y. Ju, "Visible light-driven photocatalytic degradation of rhodamine B over NaBiO<sub>3</sub>: pathways and mechanism," *The Journal of Physical Chemistry A*, vol. 113, no. 37, pp. 10024–10032, 2009.
- [3] A. Bhattacharyya, S. Kawi, and M. B. Ray, "Photocatalytic degradation of orange II by TiO<sub>2</sub> catalysts supported on adsorbents," *Catalysis Today*, vol. 98, no. 3, pp. 431–439, 2004.

- [4] J. Ovenstone, "Preparation of novel titania photocatalysts with high activity," *Journal of Materials Science*, vol. 36, no. 6, pp. 1325–1329, 2001.
- [5] M. Behpour, S. M. Ghoreishi, and F. S. Razavi, "Photocatalytic activity of  $\text{TiO}_2/\text{Ag}$  nanoparticle on degradation of water pollutions," *Digest Journal of Nanomaterials and Biostructures*, vol. 5, no. 2, pp. 467–475, 2010.
- [6] M. R. Hoffmann, S. T. Martin, W. Choi, and D. W. Bahnemann, "Environmental applications of semiconductor photocatalysis," *Chemical Reviews*, vol. 95, no. 1, pp. 69–96, 1995.
- [7] X. Chen and S. S. Mao, "Titanium dioxide nanomaterials: synthesis, properties, modifications and applications," *Chemical Reviews*, vol. 107, no. 7, pp. 2891–2959, 2007.
- [8] B. Tryba, A. W. Morawski, and M. Inagaki, "A new route for preparation of  $\text{TiO}_2$ -mounted activated carbon," *Applied Catalysis B: Environmental*, vol. 46, no. 1, pp. 203–208, 2003.
- [9] B. Neppolian, H. Yamashita, Y. Okada, H. Nishijima, and M. Anpo, "Preparation of unique  $\text{TiO}_2$  nano-particle photocatalysts by a multi-gelation method for control of the physico-chemical parameters and reactivity," *Catalysis Letters*, vol. 105, no. 1–2, pp. 111–117, 2005.
- [10] J. Zhu, J. Zhang, F. Chen, K. Iino, and M. Anpo, "High activity  $\text{TiO}_2$  photocatalysts prepared by a modified sol-gel method: characterization and their photocatalytic activity for the degradation of XRG and X-GL," *Topics in Catalysis*, vol. 35, no. 3–4, pp. 261–268, 2005.
- [11] K. Ramanathan, D. Avnir, A. Modestov, and O. Lev, "Sol-gel derived ormosil-exfoliated graphite- $\text{TiO}_2$  composite floating catalyst: photodeposition of copper," *Chemistry of Materials*, vol. 9, no. 11, pp. 2533–2540, 1997.
- [12] D.-S. Seo, J.-K. Lee, E.-G. Lee, and H. Kim, "Effect of aging agents on the formation of  $\text{TiO}_2$  nanocrystalline powder," *Materials Letters*, vol. 51, no. 2, pp. 115–119, 2001.
- [13] A. Fujishima, T. N. Rao, and D. A. Tryk, "Titanium dioxide photocatalysis," *Journal of Photochemistry and Photobiology C: Photochemistry Reviews*, vol. 1, no. 1, pp. 1–21, 2000.
- [14] K. Kabra, R. Chaudhary, and R. L. Sawhney, "Treatment of hazardous organic and inorganic compounds through aqueous-phase photocatalysis: a review," *Industrial and Engineering Chemistry Research*, vol. 43, no. 24, pp. 7683–7696, 2004.
- [15] C. Minero, G. Mariella, V. Maurino, and E. Pelizzetti, "Photocatalytic transformation of organic compounds in the presence of inorganic anions. 1. Hydroxyl-mediated and direct electron-transfer reactions of phenol on a titanium dioxide-fluoride system," *Langmuir*, vol. 16, no. 6, pp. 2632–2641, 2000.
- [16] J. Araña, J. M. Doña-Rodríguez, E. T. Rendón et al., " $\text{TiO}_2$  activation by using activated carbon as a support: part I. Surface characterisation and decantability study," *Applied Catalysis B: Environmental*, vol. 44, no. 2, pp. 161–172, 2003.
- [17] A. Ahmad, J. Thiel, and S. Ismat Shah, "Structural effects of niobium and silver doping on titanium dioxide nanoparticles," *Journal of Physics: Conference Series*, vol. 61, pp. 11–15, 2007.
- [18] A. R. Malagutti, H. A. J. L. Mourão, J. R. Garbin, and C. Ribeiro, "Deposition of  $\text{TiO}_2$  and  $\text{Ag/TiO}_2$  thin films by the polymeric precursor method and their application in the photodegradation of textile dyes," *Applied Catalysis B: Environmental*, vol. 90, no. 1–2, pp. 205–212, 2009.
- [19] Y. Lai, H. Zhuang, K. Xie et al., "Fabrication of uniform  $\text{Ag/TiO}_2$  nanotube array structures with enhanced photoelectrochemical performance," *New Journal of Chemistry*, vol. 34, no. 7, pp. 1335–1340, 2010.
- [20] Y. J. Lee, M. P. de Jong, and W. G. van der Wiel, "Electronic structure of  $\text{Co}^{2+}$  ions in anatase  $\text{Co/TiO}_2$  in relation to heterogeneity and structural defects," *Physical Review B: Condensed Matter and Materials Physics*, vol. 83, no. 13, Article ID 134404, 2011.
- [21] M. Hamadanian, A. Reisi-Vanani, and A. Majedi, "Sol-gel preparation and characterization of  $\text{Co/TiO}_2$  nanoparticles: application to the degradation of methyl orange," *Journal of the Iranian Chemical Society*, vol. 7, no. 1, pp. S52–S58, 2010.
- [22] X. Li, R. Xiong, and G. Wei, "S-N Co-doped  $\text{TiO}_2$  photocatalysts with visible-light activity prepared by sol-gel method," *Catalysis Letters*, vol. 125, no. 1–2, pp. 104–109, 2008.
- [23] C. Burda, Y. Lou, X. Chen, A. C. S. Samia, J. Stout, and J. L. Gole, "Enhanced nitrogen doping in  $\text{TiO}_2$  nanoparticles," *Nano Letters*, vol. 3, no. 8, pp. 24–26, 2003.
- [24] W. Ho, J. C. Yu, and S. Lee, "Synthesis of hierarchical nanoporous F-doped  $\text{TiO}_2$  spheres with visible light photocatalytic activity," *Chemical Communications*, no. 10, pp. 1115–1117, 2006.
- [25] V. Panić, A. Dekanski, S. Milonjić, R. Atanasoski, and B. Nikolić, "Influence of the aging time of  $\text{RuO}_2$  and  $\text{TiO}_2$  sols on the electrochemical properties and behavior for the chlorine evolution reaction of activated titanium anodes obtained by the sol-gel procedure," *Electrochimica Acta*, vol. 46, no. 2–3, pp. 415–421, 2000.
- [26] Z. He, C. Sun, S. Yang, Y. Ding, H. He, and Z. Wang, "Photocatalytic degradation of rhodamine B by  $\text{Bi}_2\text{WO}_6$  with electron accepting agent under microwave irradiation: mechanism and pathway," *Journal of Hazardous Materials*, vol. 162, no. 2–3, pp. 1477–1486, 2009.
- [27] E. Stathatos, T. Petrova, and P. Lianos, "Study of the efficiency of visible-light photocatalytic degradation of basic blue adsorbed on pure and doped mesoporous titania films," *Langmuir*, vol. 17, no. 16, pp. 5025–5030, 2001.
- [28] T. S. Natarajan, M. Thomas, K. Natarajan, H. C. Bajaj, and R. J. Tayade, "Study on UV-LED/ $\text{TiO}_2$  process for degradation of Rhodamine B dye," *Chemical Engineering Journal*, vol. 169, no. 1–3, pp. 126–134, 2011.
- [29] A. Pottier, S. Cassaignon, C. Chanéac, F. Villain, E. Tronc, and J.-P. Jolivet, "Size tailoring of  $\text{TiO}_2$  anatase nanoparticles in aqueous medium and synthesis of nanocomposites. Characterization by Raman spectroscopy," *Journal of Materials Chemistry*, vol. 13, no. 4, pp. 877–882, 2003.
- [30] M. Guglielmi, A. Martucci, E. Menegazzo et al., "Control of semiconductor particle size in Sol-gel thin films," *Journal of Sol-Gel Science and Technology*, vol. 8, no. 1–3, pp. 1017–1021, 1997.
- [31] W. Chen and W. Gao, "Sol-enhanced electroplating of nanostructured Ni- $\text{TiO}_2$  composite coatings—the effects of sol concentration on the mechanical and corrosion properties," *Electrochimica Acta*, vol. 55, no. 22, pp. 6865–6871, 2010.
- [32] T. Sugimoto, K. Okada, and H. Itoh, "Synthesis of uniform spindle-type titania particles by the gel-sol method," *Journal of Colloid and Interface Science*, vol. 193, no. 1, pp. 140–143, 1997.
- [33] T. Kasuga, M. Hiramatsu, A. Hoson, T. Sekino, and K. Niihara, "Titania nanotubes prepared by chemical processing," *Advanced Materials*, vol. 11, no. 15, pp. 1307–1311, 1999.
- [34] L. H. Huang, C. Sun, and Y. L. Liu, "Pt/N-codoped  $\text{TiO}_2$  nanotubes and its photocatalytic activity under visible light," *Applied Surface Science*, vol. 253, no. 17, pp. 7029–7035, 2007.
- [35] T. Tsumura, N. Kojitani, H. Umemura, M. Toyoda, and M. Inagaki, "Composites between photoactive anatase-type  $\text{TiO}_2$



- and adsorptive carbon," *Applied Surface Science*, vol. 196, no. 1–4, pp. 429–436, 2002.
- [36] L. Chena, X. Pang, G. Yu, and J. Zhang, "In-situ coating of MWNTs with solgel  $\text{TiO}_2$  nanoparticles," *Advanced Materials Letters*, vol. 1, no. 1, pp. 75–78, 2010.
- [37] K. Woan, G. Pyrgiotakis, and W. Sigmund, "Photocatalytic carbon-nanotube- $\text{TiO}_2$  composites," *Advanced Materials*, vol. 21, no. 21, pp. 2233–2239, 2009.
- [38] J. Matos, J. Laine, and J.-M. Herrmann, "Synergy effect in the photocatalytic degradation of phenol on a suspended mixture of titania and activated carbon," *Applied Catalysis B: Environmental*, vol. 18, no. 3–4, pp. 281–291, 1998.
- [39] J. P. R. Vissers, F. P. M. Mercx, S. M. A. M. Bouwens, V. H. J. de Beer, and R. Prins, "Carbon-covered alumina as a support for sulfide catalysts," *Journal of Catalysis*, vol. 114, no. 2, pp. 291–302, 1988.
- [40] S. K. Maity, L. Flores, J. Ancheyta, and H. Fukuyama, "Carbon-modified alumina and alumina-carbon-supported hydrotreating catalysts," *Industrial and Engineering Chemistry Research*, vol. 48, no. 3, pp. 1190–1195, 2009.
- [41] S. K. Masthan, P. S. S. Prasad, K. S. R. Rao, and P. K. Rao, "Hysteresis during ammonia synthesis over promoted ruthenium catalysts supported on carbon-covered alumina," *Journal of Molecular Catalysis*, vol. 67, no. 2, pp. 1–5, 1991.
- [42] K. S. R. Rao, P. K. Rao, S. K. Masthan, L. Kaluschnaya, and V. B. Shur, "New type of carbon coated alumina supports for the preparation of highly active ruthenium catalysts for ammonia synthesis," *Applied Catalysis*, vol. 62, no. 1, pp. L19–L22, 1990.
- [43] M. M. Mahlambi, A. K. Mishra, S. B. Mishra, R. W. Krause, B. B. Mamba, and A. M. Raichur, "Comparison of rhodamine B degradation under UV irradiation by two phases of titania nano-photocatalyst," *Journal of Thermal Analysis and Calorimetry*, vol. 110, no. 2, pp. 847–855, 2012.
- [44] M. M. Mahlambi, A. K. Mishra, S. B. Mishra, A. M. Raichur, B. B. Mamba, and R. W. Krause, "Layer-by-layer self-assembled metal-ion- (Ag-, Co-, Ni-, and Pd-) doped  $\text{TiO}_2$  nanoparticles: synthesis, characterisation, and visible light degradation of rhodamine B," *Journal of Nanomaterials*, vol. 2012, Article ID 302046, 12 pages, 2012.
- [45] M. M. Mahlambi, A. K. Mishra, S. B. Mishra, R. W. Krause, B. B. Mamba, and A. M. Raichur, "Effect of metal ions (Ag, Co, Ni, and Pd) on the visible light degradation of rhodamine B by carbon-covered alumina-supported  $\text{TiO}_2$  in aqueous solutions," *Industrial and Engineering Chemistry Research*, vol. 52, no. 5, pp. 1783–1794, 2013.
- [46] L. F. Sharanda, Y. V. Plyuto, I. V. Babich et al., "Synthesis and characterisation of hybrid carbon-alumina support," *Applied Surface Science*, vol. 252, no. 24, pp. 8549–8556, 2006.
- [47] Y. Ao, J. Xu, D. Fu, and C. Yuan, "Preparation of Ag-doped mesoporous titania and its enhanced photocatalytic activity under UV light irradiation," *Journal of Physics and Chemistry of Solids*, vol. 69, no. 11, pp. 2660–2664, 2008.
- [48] M. Stir, R. Nicula, and E. Burkel, "Pressure-temperature phase diagrams of pure and Ag-doped nanocrystalline  $\text{TiO}_2$  photocatalysts," *Journal of the European Ceramic Society*, vol. 26, no. 9, pp. 1547–1553, 2006.